

ENGINEERING EXCHANGE INTERACTION IN COUPLED
SPIN-QUBIT QUANTUM DOTS

BY

LINGXIAO ZHANG

B.S., Peking University, 2001

M.S., University of Illinois at Urbana-Champaign, 2003

DISSERTATION

Submitted in partial fulfillment of the requirements
for the degree of Doctor of Philosophy in Electrical and Computer Engineering
in the Graduate College of the
University of Illinois at Urbana-Champaign, 2008

Urbana, Illinois

Doctoral Committee:

Professor Jean-Pierre Leburton, Chair
Professor Jianming Jin
Professor Kent Choquette
Assistant Professor Nadya Mason

UMI Number: 3337987

INFORMATION TO USERS

The quality of this reproduction is dependent upon the quality of the copy submitted. Broken or indistinct print, colored or poor quality illustrations and photographs, print bleed-through, substandard margins, and improper alignment can adversely affect reproduction.

In the unlikely event that the author did not send a complete manuscript and there are missing pages, these will be noted. Also, if unauthorized copyright material had to be removed, a note will indicate the deletion.

UMI[®]

UMI Microform 3337987

Copyright 2009 by ProQuest LLC.

All rights reserved. This microform edition is protected against unauthorized copying under Title 17, United States Code.

ProQuest LLC
789 E. Eisenhower Parkway
PO Box 1346
Ann Arbor, MI 48106-1346

© 2008 Lingxiao Zhang

ABSTRACT

In this dissertation, we present theoretical studies of coupled semiconductor quantum dots containing up to two electrons. Our focus is the exchange interaction between the two electron spins because this quantity governs the fundamental quantum logic gate operation. To gain critical insight into engineering the exchange interaction, we have performed detailed calculations in two types of quantum dot systems:

For two-dimensional GaAs coupled dots, numerical exact diagonalization method is utilized to solve the one- and two-particle Schrödinger equations. We have calculated the stability diagram of the coupled dots for different dot geometries and under various magnetic fields, which reveals the relation between the stability diagram topology and the interdot coupling strength under different conditions. We have also performed detailed analysis on the interdot detuning and dot deformation effects which exemplify the general von Neumann-Wigner theorem on molecular state energies.

For coupled quantum dots formed in a single InAs quantum wire, we use the variational Heitler-London method to obtain the single- and two-particle ground state energies. We show the variational Heitler-London methods yield lower ground state energies than the conventional approach. We find that the exchange energy decreases as the wire diameter becomes smaller due to enhanced coulomb interaction in a quasi-one-dimensional system.

In memory of my father

ACKNOWLEDGMENTS

I sincerely thank my adviser, Prof. Jean-Pierre Leburton, for being a wonderful mentor of mine for seven years. I truly thank my Ph.D. committee members—Profs. Richard M. Martin, Jianming Jin, James Gary Eden, Kent D. Choquette, Nadya Mason—for their time and kindness.

I am greatly indebted to Drs. Philippe Matagne and Dmitriy V. Melnikov for their help and patience during my graduate studies. I am grateful to my teachers at the University of Illinois at Urbana-Champaign among whom Profs. Karl Hess, Paul M. Goldbart, and Michael T. Heath have not only taught me science and engineering but also inspired me to become a scholar. I appreciate the opportunities to work with Profs. Jianhua Zhang and Elyse Rosenbaum as a teaching assistant and to learn from them as well.

I thank our collaborators Ronald Hanson, Leo P. Kouwenhoven, Dyutiman Das, Richard M. Martin, Milton Feng, Gabriel Walter, Dennis Deppe, Wenhua Yang, and Sapan Agarwal. I also thank all my concurrent colleagues and fellows at the University of Illinois for helping me in my study and research. I acknowledge DARPA, NSF, CSE Fellowship program, Beckman Institute, and University of Illinois Research Council for supporting my research projects.

Finally, my thanks go to three special women in my life: mom, yaya, and yuyu.

TABLE OF CONTENTS

LIST OF TABLES	vii
LIST OF FIGURES	viii
CHAPTER 1 INTRODUCTION	1
CHAPTER 2 MODEL AND METHODS	5
2.1 Model Potential for Coupled Two-Dimensional Dots	5
2.2 Hamiltonian of the Two-Electron System	6
2.3 Theoretical Methods for Exchange Energy	8
2.3.1 The Hubbard model	8
2.3.2 The Heitler-London method	9
2.3.3 Numerical exact diagonalization method	10
2.3.4 Survey of additional methods	12
CHAPTER 3 COUPLED CIRCULAR QUANTUM DOTS	15
3.1 Single-Particle Wavefunction and Electron Density	15
3.2 Bias Voltage Dependence of Energies	16
3.3 Charge Stability Diagrams	21
3.3.1 Experimental stability diagram and general theory	21
3.3.2 Stability diagrams in magnetic fields	23
CHAPTER 4 COUPLED ELONGATED QUANTUM DOTS	30
4.1 Coupled Dots with Small Aspect Ratio	30
4.1.1 Exchange energy	30
4.1.2 Stability diagrams	32
4.1.3 Interdot detuning effects and electron localization	33
4.2 Coupled Dots with Large Aspect Ratio	36
4.2.1 System energy and exchange energy	36
4.2.2 Density and spectral function	38
4.2.3 Von Neumann-Wigner theorem	41
4.2.4 Spin phase diagram	42
4.2.5 Stability diagrams	44
4.2.6 Detuning effects	49

CHAPTER 5	COUPLED QUANTUM WIRE QUANTUM DOTS	56
5.1	Three-Dimensional Confinement Potential	56
5.2	The Variational Heitler-London Method	58
5.3	Exchange Energy	60
5.4	Size Effects	63
5.5	Discussions	68
5.5.1	Limitation of the variational Heitler-London method	68
5.5.2	Comparison with experiments	69
CHAPTER 6	CONCLUSIONS AND OUTLOOKS	71
APPENDIX A	MATHEMATICAL RESULTS FOR THE EXACT DIAGO-	
	NALIZATION METHOD	73
APPENDIX B	HEITLER-LONDON MATRIX ELEMENTS	79
REFERENCES	83
AUTHOR'S BIOGRAPHY	89

LIST OF TABLES

- 3.1 Comparison of the magnitude of the second order derivative $\kappa(1)$ and $\kappa(2)$ of the chemical potential curves $\mu(1)$ and $\mu(2)$ near their turning points for various interdot separations and magnetic fields. Units of the data are in meV^{-1} . $\kappa^S(2)$ and $\kappa^T(2)$ denote the values for the singlet and the lowest triplet state, respectively. The Zeeman effect is included here. 25

- 5.1 Values of $d = l_z$ at which the variational Heitler-London calculation breaks down due to large overlap of the localized s states for energies of different states (shown on the leftmost column) at $D = 20$ nm. The second (third) column gives the values for InAs (GaAs). The unit of $d = l_z$ is effective Bohr radius r_0 . For InAs (GaAs), $r_0 = 33.59$ (10.35) nm. 69

LIST OF FIGURES

2.1	(a) Potential contour plots for coupled circular dots with parameters $d = 60$ nm, $R_x = R_y = 30$ nm, $V_L = V_R = 25$ meV. (b) Same as (a) but for $R_x = 30$ nm, $R_y = 45$ nm. (c) Potential profile in the x direction for $V_L = V_R = 25$ meV (solid) and $V_L = 29$, $V_R = 25$ meV (dashed), $d = 60$ nm, $R_x = 30$ nm.	7
3.1	Two-dimensional plots. Columns I and II: real part of the single-particle ground and first excited states; columns III and IV: electron density of the singlet and triplet states. Rows I and II are at $B = 0$ and 6 T, respectively. Parameters for the Gaussian potential are $d = 50$ nm, $R_x = R_y = 30$ nm, $V_L = V_R = 21$ meV, and scales for the x and y direction are shown for the lower left panel and are the same for other panels.	16
3.2	Row I, single-particle energy separation between the ground and first excited states and row II, the exchange energy as a function of V_L and V_R at $B = 0$ T (column I), 3 T (column II), and 6 T (column III). Other parameters are $d = 50$ nm, $R_x = R_y = 30$ nm. Scale units are in meV. The Zeeman effect is not included here.	17
3.3	Dependence of the exchange energy on $V_L = V_R$ at (a) $B = 0$ T, (b) 3 T, and (c) 6 T. $d = 50$ nm, $R_x = R_y = 30$ nm. The Zeeman effect is not included here.	18
3.4	(a) The confinement potential for $d = 50$ nm (solid) and $d = 60$ nm (dashed) at $V_L = V_R = 25$ meV, $R_x = R_y = 30$ nm. Chemical potentials $\mu(1)$ (solid) and $\mu^S(2)$ (dashed) vs. $V_L = V_R$ for (b) $d = 50$ nm and (c) $d = 60$ nm. In both of them the horizontal line indicates the values of the chemical potential at which the contours in Fig. 3.8 are drawn.	19
3.5	Surface (contour) plots of the total energies for $N = 1$ (left column) and $N = 2$, singlet (right column) at $d = 50$ nm (top row) and $d = 60$ nm (bottom row). Scale units are in meV.	20
3.6	Experimental charge stability diagram in the few-electron regime [13].	22
3.7	Schematic illustrating the structure of the stability diagram within the circle on Fig. 3.6. Note the order of the diagram is inverted compared to Fig. 3.6.	23

- 3.8. Contour plots of the chemical potentials $\mu(1)$ and $\mu^S(2)$ as functions of V_L and V_R for $d = 50$ nm (solid) and $d = 60$ nm (dashed). The turning points on the contour lines are indicated by solid dots and the dotted line is a guide for the eyes along the main diagonal ($V_L = V_R$). The numbers on the left (right) within parentheses give the electron numbers in the left (right) dot [the (0,0) region is located at the lower left corner below the $\mu(1)$ branch for $d = 50$ nm]. 24
- 3.9 (a) $d = 50$ nm. Contour plots of the chemical potentials. Single-electron state: lower branches, solid curves. Two-electron singlet state: upper branches, solid curves. Two-electron triplet state: upper branches, dashed curves. Different magnetic fields are labeled in the figure. (b) Same as (a) but at $d = 60$ nm. The contour lines for singlet and triplet states at $B = 0$ are indistinguishable on the scale of the figure. The Zeeman effect is included here. 26
- 3.10 Double-triplet point separation projected along V_L (or V_R , $V_L = V_R$) axis as a function of the magnetic field B for (a) $d = 50$ nm and (b) $d = 60$ nm. The data for singlet and the lowest triplet states are labeled by “ Δ ” and “+”, respectively. The Zeeman effect is taken into account here. The upper (lower) inset in each figure shows the exchange energy J as a function of the magnetic field with (without) the Zeeman effect. The data in the insets are obtained at $V_L = V_R = 25$ meV. 26
- 3.11 Same as the main panels of Fig. 3.10, but without the Zeeman effect. 28
- 4.1 (a) Main panel: exchange energy dependence on the magnetic field for dots with different aspect ratios $r = R_y/R_x$, $R_x = 30$ nm. The insets (I), (II), and (III) show the contour plots of the confining potential for $r = 1$, $r = 1.5$, and $r = 0.67$, respectively. (b) Exchange energy maximum [$J(B = 0)$] and magnetic field at singlet-triplet transition [$B_0 = B(J = 0)$] and (c) merit factor $J/\hbar\omega_c$ ($\omega_c = eB_0/m_*c$) as a function of the aspect ratio $r = R_y/R_x$. For (a), (b), and (c), $V_L = V_R = 25$ meV, $d = 60$ nm, and the Zeeman effect is ignored. 31
- 4.2 Contour plots of chemical potentials $\mu(1)$ (lower branches) and $\mu^S(2)$ (upper branches) at $r = R_y/R_x = 0.67$ (dotted), 1 (dashed), and 1.5 (solid). $d = 60$ nm, $R_x = 30$ nm, $B = 0$ T, reference chemical potential value: -17 meV. 32
- 4.3 Exchange energy J as a function of V_L in the model potential at different magnetic fields. V_R is fixed at 21 meV. Other parameters are $d = 60$ nm, $R_x = R_y = 30$ nm. For clarity, curves for different B fields are shifted vertically by numerical value $-0.2B$ in the unit of meV. 33
- 4.4 Two-dimensional electron density plots for (a) $r = R_y/R_x = 1$ and (b) $r = R_y/R_x = 1.5$. In each case rows (I) and (II) are for the singlet and triplet states, respectively. Different columns are for different parameters: (I) $V_L = V_R = 21$ meV, $B = 0$, (II) $V_L = 29$, $V_R = 21$ meV, $B = 0$, and (III) $V_L = 29$, $V_R = 21$ meV, $B = 6$ T. For all cases, $d = 60$ nm and $R_x = 30$ nm. 34

4.5	Exchange energy J as a function of V_L in the model potential at different magnetic fields. V_R is fixed at 21 meV. Other parameters are $d = 60$ nm, $R_x = 30$ nm, $R_y = 45$ nm. For clarity, curves for different B fields are shifted vertically by numerical value $-0.3B$ in the unit of meV.	35
4.6	Top panels: potential contour plots of coupled QD with $r = 1$ (left), $r = 4$ (middle), and $r = 8$ (right) at $d = 50$ nm. Darker regions correspond to higher potential. Lower panel: three lowest singlet (red, solid lines) and triplet (blue, dashed lines) energy levels as a function of QD aspect ratio r at $d = 50$ nm. The inset shows r dependence of the exchange energy J (blue, solid) and tunnel coupling $2t$ (red, dotted). Other parameters are the same for all panels, which are $V_L = V_R = 25$ meV, $R_x = 30$ nm, $B = 0$	37
4.7	Contour plots of the electron density for singlet (upper row) and triplet (lower row). Columns I, II, and III are for $r = 3.9$, $r = 4$, and $r = 8$, respectively. Darker regions correspond to higher electron density.	39
4.8	Spectral decomposition of the two-electron wavefunction onto different single-particle pairs. The red (dark) columns are for $r = 3.9$, while the yellow (bright) columns are for $r = 4$. The inset shows the contour plots of the lowest three single-particle states in ascending order of energy for both $r = 3.9$ and $r = 4$	40
4.9	Mesh (contour) plot of the exchange energy J as a function of QD aspect ratio r and the magnetic field B . The thick white curves (solid and dashed) on the contour plot correspond to $J = 0$	43
4.10	Top panels: stability diagrams for $r = 1$ (left), $r = 3$ (middle), and $r = 5$ (right). In each diagram, the red, green, and blue curves (solid) are computed contour lines at which the chemical potentials $\mu(1)$, $\mu^S(2)$, and $\mu^T(2)$, respectively, equal to the reference value $\mu_{ref} = -21$ meV. Curves for different chemical potentials are also indicated by arrows. The dashed lines are a guide for eyes separating different stable charge states. Note that the exact locations of the $\mu(3)$ curve and $(1, 2)$, $(2, 1)$ regions are not computed. In the leftmost upper panel, we also indicate the double-triple points A and B. Point C is where the $\mu^S(2)$ curve has the largest curvature for $V_L \neq V_R$. The bottom panels show the computed $2t$ and J (solid curves) as a function of interdot detuning $\epsilon = V_L - V_R$ from the center of the $(1, 1)$ region for corresponding dot aspect ratios. The dashed curves on the bottom panels show the separation (Δ^{ST}) between the contour lines of $\mu^S(2)$ and $\mu^T(2)$ projected along the main diagonal of the stability diagram above as a function of interdot detuning $\epsilon = V_L - V_R$. All data are obtained at $R_x = 30$ nm, $d = 50$ nm, and $B = 0$ T.	45
4.11	Same as the stability diagrams in Fig. 4.10, but for row (I) $d = 60$ nm, $B = 0$ T. (II) $d = 50$ nm, $B = 2$ T.	48

- 4.12 Top panels: potential contour plots of coupled QD with $r = 1$ (left two) and $r = 3$ (right two). For each r , the panel on the left (right) is for $V_L = V_R = 21$ ($V_L = 31$, $V_R = 21$) meV. (a) $r = 1$. Main panel: two lowest singlet (red, solid lines) and triplet (blue, dashed lines) energy levels as a function of detuning. U (V) indicates the anticrossing point for the two lowest singlet (triplet) levels. Lower inset: zoom-in region near the anticrossing point of the singlet energy levels. (b) $r = 3$. Main panel and lowest inset same as in (a) but for $r = 3$. U' (V') indicates the anticrossing (crossing) point of the two lowest singlet (triplet) energy levels. Upper inset: three lowest single-particle energy levels in asymmetric confinement. In (a) and (b), the singlet energy levels are lowered by 3 meV for clarity. . . . 50
- 4.13 (a) Two-dimensional density plots for $r = 1$ at zero magnetic field. Columns (I), (II), and (III) correspond to $V_L = 21$, 29, and 42 meV, respectively. First (second) row, labeled S (T), is for the lowest singlet (triplet) state. (b) Same as (a) but for $r = 3$. Columns (I), (II), and (III) correspond to $V_L = 25$, 25.45, and 25.47 meV, respectively. Coordinates are shown in lower left panel and are the same for all panels. For $r = 3$, the peak separation along the x (y) direction in the density of the triplet state is ~ 60 (~ 40) nm for column (II) [(III)]. . . . 51
- 4.14 Exchange coupling J as a function of V_L (V_R fixed at 21 meV) for QD aspect ratios $r = 1$ (black, solid), $r = 1.5$ (blue, dashed), $r = 3$ (green, dashed-dotted), and $r = 5$ (red, dotted) at zero magnetic field. The scaling factor for each curve is shown in parenthesis. . . . 53
- 4.15 Main panel: J as a function of V_L for $r = 3$ at different magnetic fields. The magnetic field value is given on top of each curve. The curve for $B = 0.1$ T is indicated by an arrow. For clarity, curves at different B fields are shifted vertically in multiples of 0.03 meV. The dashed (dotted) gray line is a guide for the eyes tracing the localization point of the singlet (triplet) state at different magnetic fields. Inset: two lowest triplet energy levels at $B = 0$ T (red, dashed) and $B = 0.1$ T (blue, solid). . . . 54
- 5.1 (a) Schematic of coupled QDs $D1$ and $D2$ formed in a quantum wire. Gates $G1$ and $G5$ define the outer barriers of the two QDs; $G3$ controls the inter-dot coupling; $G2$ and $G4$ are plungers tuning the confinement in each QD. Charging current flows along the wire from source to drain. (b) Schematic of the confinement potential of the coupled QDs along the z (wire axial) direction. $\varphi_L(\mathbf{r})$ and $\varphi_R(\mathbf{r})$ denote the localized s states in the left and right QDs, respectively. . . . 57
- 5.2 (a) Single-particle ground state energy, (b) single-particle first excited state energy, (c) two-electron singlet state energy, (d) two-electron triplet state energy, (e) coulomb energy in the singlet state, (f) coulomb energy in the triplet state, (g) tunneling coupling $2t$, and (h) exchange interaction as a function of the half interdot separation d for $l_z = 30$ nm and $D = 20$ nm. The inset in (g) shows $2t$ in the zoom-in region $20 < d < 30$ nm. On each panel, the solid (dashed) line shows the VHL (HL) result. . . . 61

5.3	Main panel: Exchange coupling J (solid curve) and tunnel coupling $2t$ (dashed curve) as a function of the effective barrier height V_b^{eff} . Values of half interdot separation d corresponding to different V_b^{eff} values are shown on the upper horizontal scale. Inset: z -direction potential profile at V_b^{eff} values 0 meV (red, solid), 5 meV (green, dashed), and 10 meV (blue, dotted). Corresponding V_b values are -14.71 meV, -1.16 meV, and 6.65 meV, respectively. Values of other parameter are: $D = 20$ nm, $d = l_z = 30$ nm, and $l_b = 30$ nm.	62
5.4	(a) Exchange coupling J as a function of wire diameter D and half separation between the QDs d , which is set equal to QD radius l_z ($d = l_z$). (b) J as a function of D for different $d = l_z$ values (shown in the figure). The J value on each curve is normalized to its value at $D = 1$ nm. For $(d = l_z) = 20, 30, 40, 50, 60$ nm, $J(D = 1\text{nm}) = 2.33 \times 10^{-1}, 2.47 \times 10^{-2}, 3.53 \times 10^{-3}, 1.37 \times 10^{-3}, 4.81 \times 10^{-4}$ meV, respectively.	63
5.5	Electron density plot in the z -direction for (a) singlet and (b) triplet states at $d = l_z = 30$ nm. In each figure, the density is plotted at $D = 1$ nm (red, solid), $D = 10$ nm (green, dashed-dotted), $D = 40$ nm (blue, dashed), and $D = 80$ nm (black, dotted). For each D , the density is normalized to its peak value.	64
5.6	Variational parameters ω_z (shown as $\hbar\omega_z$), half separation a , the overlap S , and the coulomb energies as a function of D at $d = l_z = 30$ nm. Upper (lower) row is for the singlet (triplet) state.	65
5.7	Main panel: Exchange coupling as a function of the magnetic field applied along the wire without the Zeeman effect for $D = 20$ nm, $d = l_z = 30$ nm. Inset: same as main panel but with Zeeman effect.	66
5.8	Addition energy of the second electron $E^a(2)$ as a function of wire diameter D and half interdot separation $d = l_z$	68

CHAPTER 1

INTRODUCTION

Semiconductor quantum dots (QDs) are nanoscale devices in which charge carriers are confined in all three dimensions similar to the physical situation in atoms [1, 2, 3, 4, 5, 6]. The confinement is usually achieved by electrical gating and/or etching techniques applied, e.g., to a two-dimensional electron gas (2DEG) [1, 3, 7]. As they show typical atomic properties such as discrete energy levels and shell structures [8, 9], QDs are often referred to as artificial atoms. However, in contrast to real atoms, in QDs the number of electrons is tunable and the characteristic lengths of the system corresponding to external confinement potential, electron-electron interaction, and an applied magnetic field are of comparable size. Design of these QDs, which previously contained tens of electrons, has been improved to operate them in a few-electron regime where the charging of the very first electrons can be observed experimentally [8, 9].

Recently, the discovery of new principles of computation based on quantum mechanics has led to the idea of using coupled quantum dots for quantum computation [10]. In this scenario, a quantum bit or qubit (the basic unit of information in a quantum computer) is represented by a single electron spin in a single quantum dot. This representation has two main advantages: first, single electron spin exists in a well-defined two-dimensional Hilbert space. Second, spin decoherence time in GaAs can be on the order of microseconds [11], which is favorable for preserving phase coherence during quantum logic gate operation. In addition to a well-defined qubit, it has been shown that the spins in coupled quantum

dots can be entangled so as to produce the fundamental quantum controlled-NOT (CNOT) gate [10, 11]. Such an operation is achieved by electrically varying the coupling barrier or distance between the dots [12, 13, 14], and detuning the energy spectra of the individual QDs by appropriate gate biasing [11, 15]. The CNOT gate operation, when cast into a physical picture, is given by temporary exchange interaction $J(t)$ between two spins S_1 and S_2 described by a Heisenberg Hamiltonian

$$H_S(t) = J(t) \mathbf{S}_1 \cdot \mathbf{S}_2. \quad (1.1)$$

Due to its fundamental role in coupled quantum dot systems for quantum computing applications, the exchange interaction is the focus of both experimental and theoretical works. Experimentally, the extraction of the exchange interaction relies on the charge stability diagram in which the boundaries between distinctive stable charge states, i.e., between the states with fixed number of electrons N_1 and N_2 in each of the coupled dots, are represented as functions of the two controlling gate biases, one for each dot [14]. Recent experimental studies have used different methods for exchange interaction extraction: one is based on the Hubbard model, which involves the analysis of double-triplet point (DTP) separation on the stability diagram [16]; the other utilizes Zeeman splitting and interdot detuning in a coherent control cycle of double QDs to measure the exchange interaction indirectly [15]. In theoretical approaches, a variational method such as Heitler-London or exact diagonalization is commonly used to obtain the dependence of the exchange interaction on the system parameters such as the interdot separation, the tunneling barrier between the QDs, and externally applied magnetic field [17, 18, 19, 20, 21].

Very recently, the exploration of new hardware schemes at the frontier of solid state quantum computing has unveiled a new approach to fabricate coupled quantum dots (QDs) with controlling gate grid adjacent to an InAs quantum wire (QW) [22, 23]. In these device structures, electrons are laterally confined (i.e., perpendicular to the axial direction of the

wire) by the wire external surfaces (wire diameters are tens or even a few nanometers) [24], and longitudinally confined in the wire axial direction by the electrostatic potential barriers created by the local controlling gates. The local gate width and separation range from ~ 10 to ~ 100 nm, which results in small effective dot sizes and interdot separations, so that size quantization effects and exchange coupling between the QDs are expected to be significantly larger than that in the two-dimensional electron gas (2DEG) based semiconductor QDs [25]. In quantum wire quantum dot (QWQD) systems, the distance between the controlling gates and the QD region (~ 25 nm) [22, 23] is smaller than that in 2DEG-based QDs (~ 100 nm) [15], leading to better electrostatic control of the charge (spin) states in the QDs. Furthermore, QWQD structures offer linear scalability (i.e., with the linear grid of the controlling gates) instead of the 2D scalability resulting from top or side gate patterning in 2DEG-based QDs [22, 23].

The theoretical work presented in this dissertation is inspired by concurrent experiments: the motivation behind the first part of this dissertation is to formulate the procedure to numerically simulate the charge stability diagram and therefore set a bridge between the experimentally well studied stability diagrams and the theoretically well investigated exchange coupling [26]. Studies in the second part of this dissertation originate from the experimental results on the exchange energy dependence on the interdot detuning [15]. Because of the emerging importance of the quantum wire quantum dot systems, the last part of this dissertation is dedicated to the discussion of theoretical calculations of the exchange energy in such systems.

This dissertation is organized as follows:

In Chapter 2, we discuss various theoretical models and methods to study coupled quantum dot systems. Special emphases are given to coupled Gaussian potentials and numerical exact diagonalization method, which serve as the theoretical foundation for Chapters 3 and 4.

In Chapter 3, we focus on coupled circular dot systems and study the topology of the stability diagram and the exchange energy with respect to the interdot coupling strength as a result of interdot distance and perpendicular magnetic fields.

In Chapter 4, we investigate combined geometric and interdot detuning effects on coupled elliptical quantum dots.

In Chapter 5, we explore coupled quantum wire quantum dots. Special emphasis is given to the size effects on the exchange energy.

Finally, in Chapter 6, we summarize important findings in previous chapters and present outlooks for new hardware schemes for computation.

CHAPTER 2

MODEL AND METHODS

In this chapter, we discuss the confinement potential model and system Hamiltonian for the two-dimensional coupled quantum dot (CQD) system. We then give a survey of various theoretical methods for solving the Schrödinger equation of two electrons in such systems, with a special emphasis on the exact diagonalization (ED) method. Based on the our model and the ED method, we obtain the results in Chapters 3 and 4.

2.1 Model Potential for Coupled Two-Dimensional Dots

We use the following two-dimensional model potential for the coupled quantum dot system:

$$V(x, y) = -V_L e^{-(x+d/2)^2/R_x^2 + y^2/R_y^2} - V_R e^{-(x-d/2)^2/R_x^2 + y^2/R_y^2}. \quad (2.1)$$

The above potential involves five adjustable parameters, d is the interdot separation in the x direction, which is the main factor affecting the coupling between the two electrons in coupled QDs. R_x and R_y are the extension of the each QD in the x and y directions, respectively. By fixing one of them and changing the other, we are able to deform the dot from a circular shape to an elliptical one. V_L and V_R control the depth of the left and

Some of the material presented in this chapter was originally published. L.-X. Zhang, D. V. Melnikov, and J.-P. Leburton, Physical Review B, vol. 74, p. 205306, 2006. "Copyright 2006 by the American Physical Society." © 2007 IEEE. Reprinted, with permission, from L.-X. Zhang, D. V. Melnikov and J.-P. Leburton, "Engineering exchange coupling in double elliptic quantum dots," *IEEE Transactions on Nanotechnology*, vol. 6, pp. 250-255, 2007.

right dots. The variation of them is used to simulate the physical process of changing the top controlling gate biases in experimental devices. Figure 2.1(a) shows the potential contour plots for coupled circular dots with parameters $d = 60$ nm, $R_x = R_y = 30$ nm, $V_L = V_R = 25$ meV. Figure 2.1(b) shows the potential contour plots for coupled elliptical dots with parameters $d = 60$ nm, $R_x = 30$ nm, $R_y = 45$ nm, $V_L = V_R = 25$ meV. In Fig. 2.1(c), the potential shape in the x direction of $V_L = V_R = 25$ meV (solid) and $V_L = 29$, $V_R = 25$ meV (dashed) are compared with parameters $d = 60$ nm, $R_x = 30$ nm.

In addition to the coupled Gaussian-shaped potential given by Eq. (2.1) [18, 20], several other confinement potential shapes for CQDs have been investigated, such as coupled parabolic potential [19] and coupled quartic potential [17] with the following expressions:

$$V(x, y) = \frac{1}{2}m^*\omega_0^2 \min \left\{ \left(x - \frac{d}{2}\right)^2 + y^2, \left(x + \frac{d}{2}\right)^2 + y^2 \right\}, \quad (2.2)$$

$$V(x, y) = \frac{1}{2}m^*\omega_0^2 \left[\frac{1}{4a^2}(x^2 - a^2)^2 + y^2 \right]. \quad (2.3)$$

We note that in the QD coupling direction the investigated potential shapes have either a polynomial dependence or Gaussian dependence. For such potential shapes it is relatively easy to obtain the matrix element in the exact diagonalization method given the basis states being Harmonic oscillator states or Landau level states (product of polynomial and Gaussian). Although different potential shapes are equally applicable to studying CQDs, the Gaussian shaped potential has the advantage of fitting closely to the confinement profile in realistic QDs [27, 28].

2.2 Hamiltonian of the Two-Electron System

The Hamiltonian for the coupled system is given by

$$\hat{H} = \hat{H}_{orb} + \hat{H}_Z, \quad (2.4)$$

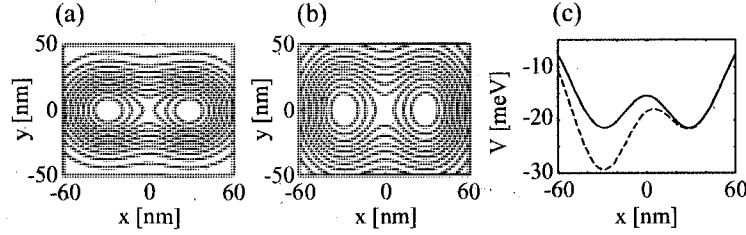


Figure 2.1 (a) Potential contour plots for coupled circular dots with parameters $d = 60$ nm, $R_x = R_y = 30$ nm, $V_L = V_R = 25$ meV. (b) Same as (a) but for $R_x = 30$ nm, $R_y = 45$ nm. (c) Potential profile in the x direction for $V_L = V_R = 25$ meV (solid) and $V_L = 29$, $V_R = 25$ meV (dashed), $d = 60$ nm, $R_x = 30$ nm.

$$\hat{H}_{orb} = \hat{h}(\mathbf{r}_1) + \hat{h}(\mathbf{r}_2) + C(\mathbf{r}_1, \mathbf{r}_2), \quad (2.5)$$

$$\hat{h}(\mathbf{r}) = \frac{1}{2m^*}(\mathbf{p} + \frac{e}{c}\mathbf{A})^2 + V(\mathbf{r}), \quad (2.6)$$

$$C(\mathbf{r}_1, \mathbf{r}_2) = e^2/\epsilon|\mathbf{r}_1 - \mathbf{r}_2|, \quad (2.7)$$

$$\hat{H}_Z = g\mu_B \sum_i \mathbf{B} \cdot \mathbf{S}_i. \quad (2.8)$$

In above, the total Hamiltonian \hat{H} consists of the orbital part \hat{H}_{orb} and the Zeeman part \hat{H}_Z , which are separated by neglecting the spin-orbit interaction. The orbital part of the Hamiltonian contains the single-particle Hamiltonians and the coulomb interaction between the two electrons. The Zeeman term simply induces a constant shift for nonzero spins. $\mathbf{A} = \frac{1}{2}[-By, Bx, 0]$ is the vector potential in the symmetric gauge for a constant magnetic field B oriented perpendicular to the QD plane (xy -plane). The effective mass m^* , dielectric constant ϵ , and the g -factor g are material dependent and for GaAs $m^* = 0.067m_e$, $\epsilon = 12.9$ and $g = -0.44$; μ_B is the Bohr magneton.

Here, we note the different energy scales in GaAs QDs: the single-particle energy level spacing is 1 – 10 meV, and intradot coulomb energy is on the same order. The Zeeman energy lowers the triplet energy by 25 $\mu\text{eV} / \text{T}$. The spin-orbit interaction and hyperfine interaction are 10^{-7} and 10^{-5} times of the single-particle energy spacing, respectively [17, 29]. Therefore, if thermal effects are not taken into account in GaAs QDs, the dominant

energy contributions to a two-electron system are from the single-particle energies and coulomb interaction.

2.3 Theoretical Methods for Exchange Energy

2.3.1 The Hubbard model

The Hubbard model is arguably the simplest model for obtaining the exchange energy in CQDs. It was first developed by J. Hubbard in the 1960s to treat electron correlations in narrow energy bands [30, 31, 32]. Within the Hubbard model, the exchange energy in CQDs is given by $J = 4t^2/U_H$. $2t$ is called the tunnel coupling term given by the energy difference of the single-particle ground and first excited states. U_H is the on-site repulsion term, which is the coulomb interaction between two electrons if they are placed in a single dot. The Hubbard model has been used to estimate the exchange energy from data obtained in transport experiments on laterally coupled vertical quantum dots [16], in which it was modified to take into account the interdot coulomb interaction $J = 4t^2/(U_{intra} - U_{inter})$. It has also been discussed in theoretical works which leads to the extended Hubbard limit, where $J = 4t^2/U_H + V$. By incorporating in the V term the difference in the coulomb energy of different spin states, this extended expression gives qualitative explanation of the singlet-triplet transition [17, 33]. Although quantitative exactness cannot be achieved based on the Hubbard model, it usually gives a reasonable estimate of the order of magnitude of the exchange energy in the absence of magnetic field, given predetermined $2t$ and U_H values. The validity of the Hubbard model is discussed by comparing its numerical results with those obtained from methods with higher accuracy (see Sections 3.3.2, 5.3, and [17, 33]).

2.3.2 The Heitler-London method

The method named after Heitler-London assumes that many-electron lowest-energy wave functions in molecules may be written in terms of the one-electron ground-state orbitals of the isolated constituent atoms [34, 35]. In the context of two coupled quantum dots, each containing a single electron, this picture reduces to its simplest form; namely the two-electron wavefunctions in the singlet and triplet states are given by the symmetric and antisymmetric linear combination of the localized $1s$ orbitals:

$$\Psi^{S/T}(\mathbf{r}_1, \mathbf{r}_2) = \frac{\varphi_L(\mathbf{r}_1)\varphi_R(\mathbf{r}_2) \pm \varphi_L(\mathbf{r}_2)\varphi_R(\mathbf{r}_1)}{\sqrt{2(1 \pm S^2)}}, \quad (2.9)$$

where $\Psi^{S/T}$ denotes the singlet (triplet) wavefunction; φ_L, φ_R denote the $1s$ states wavefunction localized in the two dots (“L” and “R” mean “left” and “right,” respectively); $S = \langle \varphi_L | \varphi_R \rangle$ is the overlap between the two $1s$ wavefunctions. Using the trial wavefunctions, the exchange energy (without Zeeman effect) is calculated by

$$J = \langle \Psi^T | \hat{H}_{orb} | \Psi^T \rangle - \langle \Psi^S | \hat{H}_{orb} | \Psi^S \rangle. \quad (2.10)$$

From a different viewpoint, the Heitler-London formulation is in effect the simplest case for a configuration interaction (molecular orbital interaction, exact diagonalization) calculation. Because of its simple form, it is computationally very efficient, and with polynomial or Gaussian-shaped confining potential, an analytical form of J can be obtained.

Compared to the Hubbard model, the Heitler-London approximation makes an improvement on exchange energy calculation in that it implicitly takes into account the different spins of singlet and triplet by using symmetric and antisymmetric linear combinations in the spatial wavefunction and explicitly computes the coulomb matrix elements. Although it has been shown that the results of J from Heitler-London calculations could offset the exact value by several meVs, it gives correct qualitative behaviors, e.g., J as a function of magnetic fields [33, 36]. Its numerical accuracy can be improved by incorporating varia-

tional parameters in the trial wavefunctions to minimize the system energies (see Section 5.2)

It has been pointed out that the Heitler-London method becomes invalid as the interdot (or interatom) distance is either too small (depending on the coulomb energy compared to the single-dot confinement) or too large, both due to an overestimate of the overlap term S . More quantitative discussions on this point can be found in [37] and the references therein.

2.3.3 Numerical exact diagonalization method

The main method we use to solve the Schrödinger equation to obtain the results in Chapters 3 and 4 is the numerical exact diagonalization (ED) method. Using this method, a matrix is constructed by using a large number of basis states, then the matrix is diagonalized to obtain the system energies. Since a large number of basis states need to be considered, this method is computationally expensive. The size of the matrix and the time for evaluating the coulomb matrix element are both $O(N^4)$, N being the number of basis states. For a fixed number of basis states, variational parameters are sometimes introduced in the basis states to minimize the energy (for harmonic oscillator states, the oscillator frequency is usually used as variational parameter), which makes the method even more computationally expensive. The advantage of this method is that a high accuracy in the energy can be achieved, and the energies of the excited states can be extracted in the diagonalization procedure. For this reason, we use this method in our calculation, and its advantage is reflected by the accurate energy results obtained for QDs with large separations or under large magnetic fields.

Our numerical exact diagonalization method consists of two steps [38]. We solve the single- and two-particle problem in a sequence

$$\hat{h}\psi_i(\mathbf{r}) = e_i\psi_i(\mathbf{r}), \quad (2.11)$$

$$\hat{H}_{orb}\Psi_i^{S/T}(\mathbf{r}_1, \mathbf{r}_2) = E_i\Psi_i^{S/T}(\mathbf{r}_1, \mathbf{r}_2). \quad (2.12)$$

The full expressions for \hat{h} and \hat{H}_{orb} are given by Eqs. (2.6) and (2.5), respectively. In the following, we outline the main numerical procedure and give the expressions of the relevant quantities. The mathematical details are given in Appendix A. If we use a finite number of basis states, Eqs. (2.11) and (2.12) can both be transformed into generalized eigenvalue problem [39]

$$\mathbf{HC} = \mathbf{ESC}. \quad (2.13)$$

The matrix element for the single-particle problem is $\langle \chi_i(\mathbf{r}) | \hat{h} | \chi_j(\mathbf{r}) \rangle$ where $\chi_i(\mathbf{r}) = \phi_m(x)\phi_n(y)$, and ϕ_n denotes the n -th harmonic oscillator states (in this work, we use up to nine harmonic states in each direction). The frequencies of the harmonic oscillator states are adjustable parameters. For the two-particle problem, the matrix element is $\langle \Lambda_p^{S/T}(\mathbf{r}_1, \mathbf{r}_2) | \hat{H}_{orb} | \Lambda_q^{S/T}(\mathbf{r}_1, \mathbf{r}_2) \rangle$, and $\Lambda_s^{S/T}(\mathbf{r}_1, \mathbf{r}_2) = \chi_i(\mathbf{r}_1)\chi_j(\mathbf{r}_2) \pm \chi_j(\mathbf{r}_1)\chi_i(\mathbf{r}_2)$. Note that for the singlet state $i = j$ is allowed, albeit not for the triplet state. In our construction of the trial wavefunctions, we start with harmonic oscillator states centered at the origin ($x = 0, y = 0$). One can offset these coordinates and localize the basis states at different points. One common choice is to shift the basis states to center at the potential minima [18], or several centers around the potential minima [20].

Upon completion of the diagonalization procedure, we extract the quantities of interest, which include the system energies e_i and $E_i^{S/T}$. Here, we *emphasize* that in this dissertation if not specifically mentioned, “singlet” and “triplet” refer to the singlet and triplet ground states. The chemical potential of the N -th electron is given by the following equation [14]:

$$\mu(N) = E_0(N) - E_0(N - 1), \quad (2.14)$$

where $E_0(N)$ [note $E_0(0) = 0$] is the ground state energy. The exchange energy is given

by

$$J = E_0^T(2) - E_0^S(2). \quad (2.15)$$

The single-particle wavefunctions is $\psi_i(\mathbf{r})$ (we usually extract the real part). The two-electron density is given by

$$\rho^{S/T}(\mathbf{r}_1) = \int |\Psi_0^{S/T}(\mathbf{r}_1, \mathbf{r}_2)|^2 d\mathbf{r}_2. \quad (2.16)$$

The spectral function is defined as the projection coefficients of the singlet and triplet ground states onto the single-particle product states

$$\alpha_{k,l}^{S/T} = \left\langle \psi_k(\mathbf{r}_1) \psi_l(\mathbf{r}_2) | \Psi_0^{S/T}(\mathbf{r}_1, \mathbf{r}_2) \right\rangle. \quad (2.17)$$

Finally, the expectation value of the parity operator is given by

$$\langle \hat{P} \rangle = \left\langle \Psi_0^{S/T}(x_1, y_1, x_2, y_2) | \Psi_0^{S/T}(-x_1, -y_1, -x_2, -y_2) \right\rangle, \quad (2.18)$$

and for the parity operator along the y -axis

$$\langle \hat{P}_y \rangle = \left\langle \Psi_0^{S/T}(x_1, y_1, x_2, y_2) | \Psi_0^{S/T}(x_1, -y_1, x_2, -y_2) \right\rangle. \quad (2.19)$$

2.3.4 Survey of additional methods

In this section, we give a quick survey of more theoretical methods that found application to the study of the electronic structure of CQDs. The purpose is far from delving into the mathematical and computational details, but to discuss the general principles behind each method and provide further references.

The Heitler-London method can be extended to include not only the lowest symmetric and antisymmetric states from the localized $1s$ orbitals, but also the doubly occupied $1s$ orbitals for the singlet states. The system energy is therefore computed using four two-

electron basis states. Such a method is called the Hund-Mulliken approach. Its application to two-electron CQD problem leads to the extended Hubbard limit, in which the conventional terms in the Hubbard model are expressed explicitly as the matrix elements of the four trial wavefunctions, and different spin states (singlet and triplet) are properly taken into account [17].

In addition to the Hund-Mulliken approach, other methods that conventionally found important applications in atomic and molecular systems have also been applied to study CQD systems, the most prominent being the Hartree-Fock (HF) method and density functional theory (DFT). In both methods, the many-body Schrödinger equation is transformed into a single-particle problem by treating the electron-electron interaction as an additional term in the single-particle energy: in the HF method, this is done by introducing the Fock operator which includes the nonlocal coulomb and exchange interactions; in DFT, the electron-electron interaction is treated as a functional of the electron densities. In DFT, the interaction term can be taken to depend only on local densities, and such an approximation is called local density approximation (LDA). If spin information is considered in LDA, the resulting approach is called local spin density approximation (LSDA). Since in both methods, no precise many-body wavefunction is constructed, and electron-electron interaction is only taken into account by approximations, the resulting energies could become unsatisfactory especially for few electrons in a weak confinement potential, in which situation the exact diagonalization method is more advantageous. However, the advantage of both methods lies in that they remain computationally tractable for large number of electrons (usually tens of electrons). Reviews of the HF method and DFT are given by [40] and [41], respectively. A review of their applications in QDs can be found in [5]. Specific applications of the HF method to CQDs can be found in [18, 42] and references therein. Specific applications of DFT to CQDs can be found in [43, 44, 45, 46, 47] and references therein.

The variational Monte Carlo (VMC) method has also been applied to the study of CQD systems. Similar to other variational methods, it introduces variational parameters in a finite number of basis states and minimizes the system energy with respect to these parameters [48]. The particular feature of this method is that Monte Carlo integral is used for computing the target function for minimization. A good agreement is found between results of VMC and ED methods for the exchange energy of two electrons in CQD systems [49].

Meshing is a technique often used in combination with above methods. At one level, a nonanalytical confining potential is first projected onto a spatial mesh. The ED method can then proceed based on the matrix elements from the projected potential [38, 50]. At another level, a single-particle problem is solved based on the constructed mesh using the finite difference (element) method. For DFT calculations, this procedure is a major step of the calculation (see [51] and references therein). For ED calculations, this procedure serves as an intermediate step, after which the many-body wavefunction is constructed using obtained single-particle wavefunctions on a mesh [33, 52, 53].

CHAPTER 3

COUPLED CIRCULAR QUANTUM DOTS

In this chapter, we focus on coupled QDs with circular shape. Our main purpose is to compare the exchange energy and stability diagram of QDs with different interdot coupling strength.

3.1 Single-Particle Wavefunction and Electron Density

In Fig. 3.1, we display the real part of the single-particle wavefunction of the s and p states in column I [$re(\psi_0)$] and II [$re(\psi_1)$] and the electron density for the singlet and triplet states in column III ($\rho_{S=0}$) and IV ($\rho_{S=1}$). Data in Row I and II are computed at $B = 0$ and 6 T, respectively. Parameters for the Gaussian potential are $d = 50$ nm, $R_x = R_y = 30$ nm, $V_L = V_R = 21$ meV, and scales for the x and y direction are shown for the lower left panel and are the same for other panels. At $B = 0$ T (Row I), despite the presence of the interdot barrier (barrier height 1.67 meV), the s and p states resemble the corresponding ones in a single dot elongated in the x direction, which implies strong interdot coupling at $d = 50$ nm. The electron density profiles show more clearly the localization of the two electrons in each dot and the singlet state has much stronger interdot coupling than the triplet. The

The material presented in this chapter was originally published. L.-X. Zhang, D. V. Melnikov, and J.-P. Leburton, Physical Review B, vol. 74, p. 205306, 2006. "Copyright 2006 by the American Physical Society."

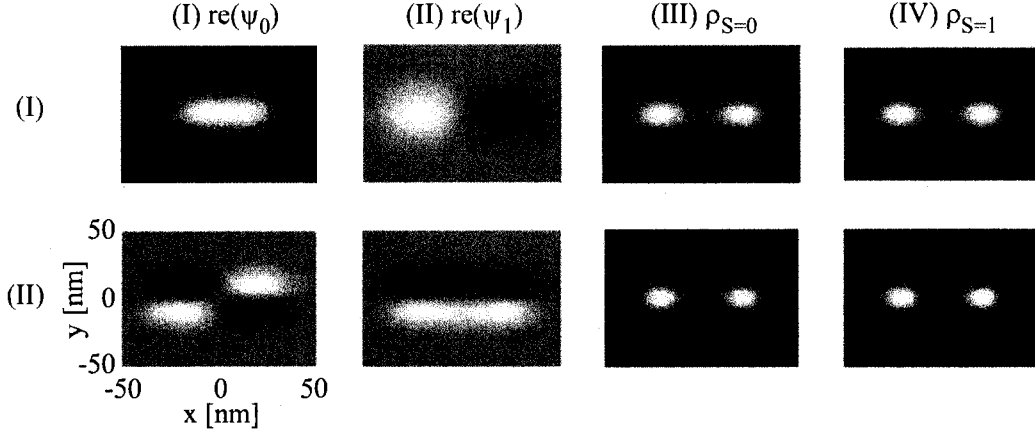


Figure 3.1 Two-dimensional plots. Columns I and II: real part of the single-particle ground and first excited states; columns III and IV: electron density of the singlet and triplet states. Rows I and II are at $B = 0$ and 6 T, respectively. Parameters for the Gaussian potential are $d = 50$ nm, $R_x = R_y = 30$ nm, $V_L = V_R = 21$ meV, and scales for the x and y direction are shown for the lower left panel and are the same for other panels.

exchange energy for this setup is 0.245 meV. At $B = 6$ T, more complicated structures in the s and p states (real parts) are observed due to the interplay between confinement, interdot coupling, and magnetic field effects. But the electron densities are similar to the corresponding ones at $B = 0$ T. The singlet and triplet states show comparable interdot coupling strength due to the localizing magnetic field, and the exchange energy in this case is -0.018 meV.

3.2 Bias Voltage Dependence of Energies

In Fig. 3.2, we plot the variation of the single-particle energy separation between the ground and first excited states (row I) and the exchange energy (row II) as a function of V_L and V_R at magnetic field $B = 0$ T (column I), 3 T (column II), and 6 T (column III); other parameters are $d = 50$ nm, $R_x = R_y = 30$ nm. In contrast to its small variation along the main diagonal ($V_L = V_R$), the single-particle energy separation increases drastically with the interdot detuning ($|\epsilon|$, $\epsilon = V_L - V_R$) for the investigated magnetic fields. The contours parallel to the main diagonal indicate that the single-particle energy separation

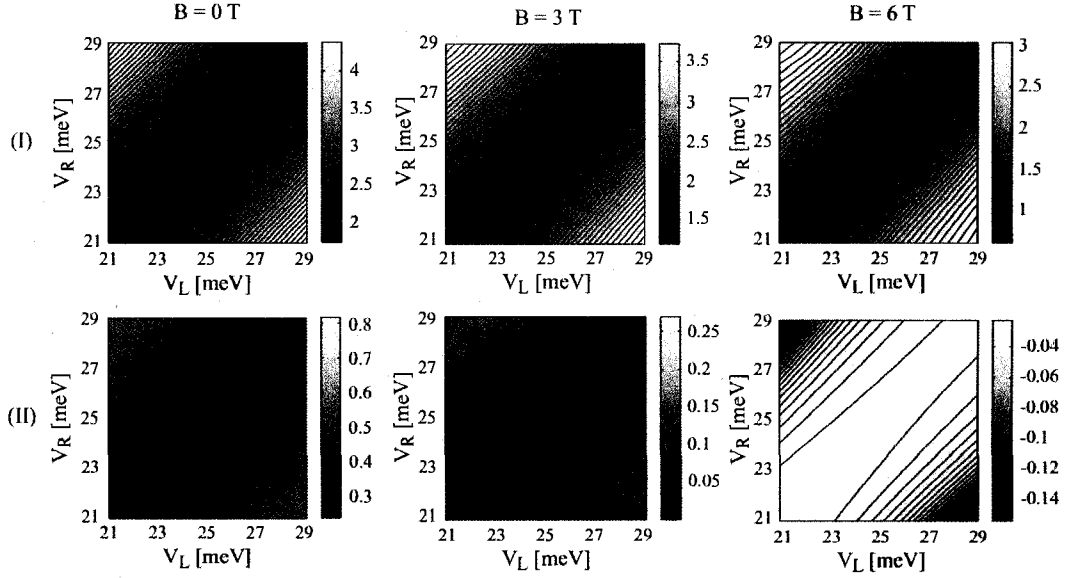


Figure 3.2 Row I, single-particle energy separation between the ground and first excited states and row II, the exchange energy as a function of V_L and V_R at $B = 0$ T (column I), 3 T (column II), and 6 T (column III). Other parameters are $d = 50$ nm, $R_x = R_y = 30$ nm. Scale units are in meV. The Zeeman effect is not included here.

is dependent mainly on interdot detuning, which is the relative difference between V_L and V_R , but not their absolute values. We observe that for a fixed bias $V_L = V_R$ along the main diagonal, the single-particle energy separation decreases as the magnetic field increases, as seen by comparing the different scales of row I on Fig. 3.7 (see [19]). This is because the magnetic field localizes the electron wavefunction and decouples the electrons in each dot, resulting in less quantum mechanical interaction between the two electrons.

The contour plots of the exchange energy J as a function of V_L and V_R are similar to those of the single-particle separation; however, deviation from linearity near the main diagonal $V_L = V_R$ is observed. Note in particular that at $B = 6$ T the exchange energy decreases to a more negative value as the interdot detuning ($|\epsilon|$, $\epsilon = V_L - V_R$) increases. The strong dependence on the interdot detuning of the single-particle energy separation and the exchange energy results from the fact that larger interdot detuning tends to localize the electrons into the dot with a lower potential, which effectively leads to a single dot.

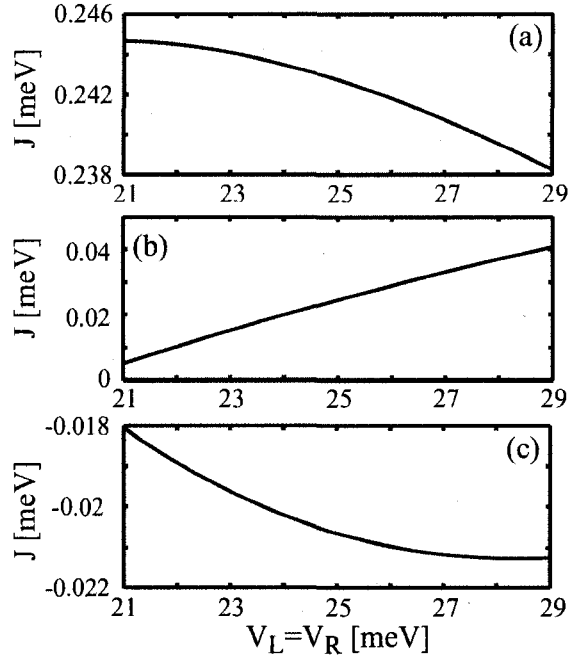


Figure 3.3 Dependence of the exchange energy on $V_L = V_R$ at (a) $B = 0$ T, (b) 3 T, and (c) 6 T. $d = 50$ nm, $R_x = R_y = 30$ nm. The Zeeman effect is not included here.

In Fig. 3.3, we plot the variations of the exchange energy J on $V_L = V_R$ (along the main diagonal in Fig. 3.2, row II) for (a) $B = 0$ T, (b) 3 T, and (c) 6 T. The variation of the exchange energy from $V_L = V_R = 21$ to 29 meV is relatively small for $B = 0$ and 6 T, while at $B = 3$ T near which the singlet-triplet transition ($J = 0$) occurs, there is an order of magnitude increase in J over this bias range. The difference at different magnetic fields can be qualitatively understood by analyzing potential variations as $V_L = V_R$ changes from 21 to 29 meV. On one hand, the confinement in the x direction becomes larger. On the other hand, the barrier between the two dots becomes higher. In general, a stronger confinement in the coupling direction induces larger single-particle level separation and results in an increase of the exchange energy, while a higher barrier tends to decouple more the two dots and results in a decrease of the exchange energy. However, these competing effects are affected by the presence of the magnetic field, specifically magnetic localization which results in the different behaviors displayed in Fig. 3.3(a), (b), and (c).

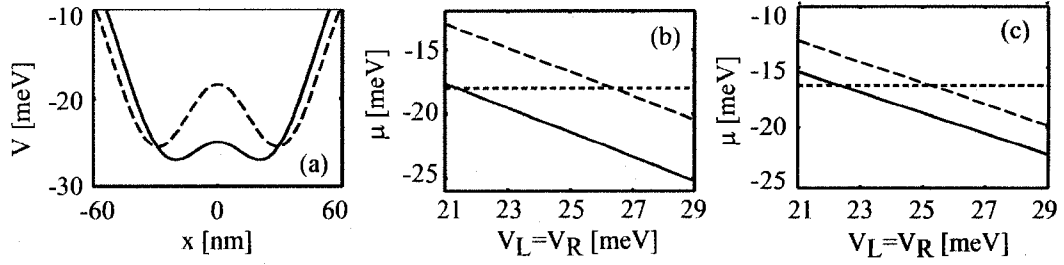


Figure 3.4 (a) The confinement potential for $d = 50$ nm (solid) and $d = 60$ nm (dashed) at $V_L = V_R = 25$ meV, $R_x = R_y = 30$ nm. Chemical potentials $\mu(1)$ (solid) and $\mu^S(2)$ (dashed) vs. $V_L = V_R$ for (b) $d = 50$ nm and (c) $d = 60$ nm. In both of them the horizontal line indicates the values of the chemical potential at which the contours in Fig. 3.8 are drawn.

We now consider two coupled QD systems with different interdot separations $d = 50$ nm (strong coupling) and $d = 60$ nm (weak coupling). The confinement potentials for the two cases are plotted in Fig. 3.4(a) for $d = 50$ nm (solid) and $d = 60$ nm (dashed) with other parameters $R_x = R_y = 30$ nm, $V_L = V_R = 25$ meV. It is seen that, aside from the increased lateral separation, the barrier is also higher in the latter case (1.98 vs. 7.10 meV). Figure 3.4(b) and (c) show the chemical potentials for one electron $\mu(1)$ and two electron singlet $\mu^S(2)$ which decrease almost linearly as V_L and V_R simultaneously increase in the absence of the magnetic field. Note that this linear dependence is different from that of the exchange energy. Here, we consider $\mu^S(2)$ since singlet is the ground state in the absence of the magnetic field. We also find linear dependence on $V_L = V_R$ of $\mu^T(2)$ (for the lowest triplet state) with similar slope in the absence of the magnetic field and slightly larger slopes for the linear decrease of $\mu^S(2)$ and $\mu^T(2)$ at nonzero magnetic fields.

Figure 3.5 shows the dependences of the total energies $E_0(1)$ and $E_0^S(2)$ for one and two electrons on V_L and V_R . In all cases, energy is lowered as V_L or V_R is increased since the potential energy is lowered. We see that in the one-electron case (left column), the curvature of $E_0(1)$ in the region where V_L and V_R are near each other ($V_L \sim V_R$) is much larger for $d = 60$ nm than for $d = 50$ nm because of the weaker coupling between the QDs in the former case. We also note that for both values of the interdot distance, the curvatures

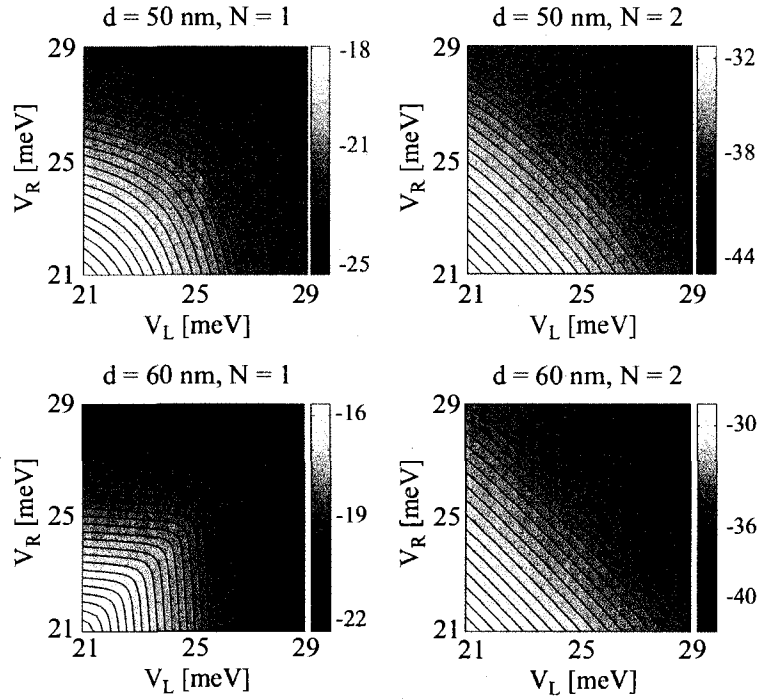


Figure 3.5 Surface (contour) plots of the total energies for $N = 1$ (left column) and $N = 2$, singlet (right column) at $d = 50 \text{ nm}$ (top row) and $d = 60 \text{ nm}$ (bottom row). Scale units are in meV.

of the energy contour plots increase slightly along the main diagonal since the coupling between the dots decreases as $V_L = V_R$ gets larger.

However, when two electrons populate the QD system, the situation becomes radically different: in the weak coupling case ($d = 60 \text{ nm}$, bottom right), the total energy of the two-electron system in the $V_L \sim V_R$ region is almost linearly dependent on V_L (V_R), i.e., the curvature is vanishingly small, while for $d = 50 \text{ nm}$ (top right) the energy curves clearly exhibit a nonlinear behavior with nonzero curvatures. The large overlap between the electron wavefunctions in the strong interdot coupling case ($d = 50 \text{ nm}$) is responsible for the smooth nonlinear dependence of the energy on V_L (V_R). However, in the weak-coupling case ($d = 60 \text{ nm}$), the two electrons are well localized in the individual QDs by coulomb repulsion and the large barrier between the dots, so that the potential change in one QD caused by the variation of V_L (V_R) does not affect the electron charge distribution but only acts as a constant addition to the total energy. This leads to the linear contours

shown on the lower right panel in Fig. 3.5. These contour lines are characterized by $V_L + V_R = \text{constant}$, where the *constant* is determined by the total potential energy. When the difference between V_L and V_R becomes sufficiently large to overcome the coulomb repulsion, the two electrons move into one QD. This is accompanied by a change in the slope of the energy curves which become either horizontal or vertical as V_L (or V_R) no longer affects the total energy and correspond to transitions to (0,2)/(2,0) regions on the stability diagram [14]. We emphasize that the observed quasi-linear behavior of the total energy $E_0(2)$ when $V_L \sim V_R$ in the weak coupling regime ($d = 60$ nm) is physically different from the situation in two coalesced dots where both $E_0(1)$ and $E_0(2)$ are also straight lines perpendicular to the main diagonal in the $V_L - V_R$ plane [14]. In the latter case the system is effectively a single QD and changing either V_L or V_R by the same amount has the same effect on the total energy of the system.

3.3 Charge Stability Diagrams

3.3.1 Experimental stability diagram and general theory

Figure 3.6 shows the charge stability diagram of an experimental structure in the few electron regime [13]. The dark lines signify the conductance minimum of very sensitive charge detectors as a function of two controlling gate biases V_L and V_{PR} for the left and right dot, respectively. The almost horizontal (vertical) lines correspond to single electron charging events in the left (right) dot and they separate the whole region into distinct stable charge states; e.g., “12” means one electron in the left dot and two electrons in the right dot are the stable charge state in the specified bias range.

For quantum computing, it is most interesting to investigate the coupled quantum dot systems with up to two electrons (see Chapter 1). Therefore, in our work we focus on the corresponding regions on the stability diagram. Along the circle on Fig. 3.6, the system could undergo a transition from “00” to “01” to “10” to “11.” It is seen that there is a small

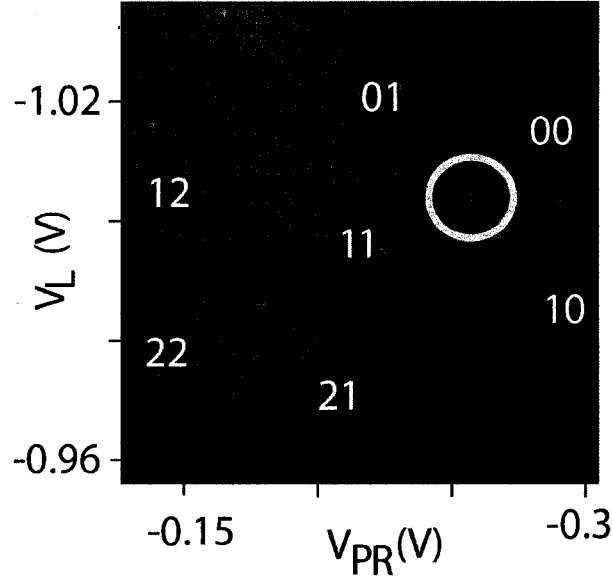


Figure 3.6 Experimental charge stability diagram in the few-electron regime [13].

segment separating the dark lines between the “00” and “11” regions. Figure 3.7 shows a schematic illustrating more clearly the structure of the stability diagram inside the circle on Fig. 3.6 (note that the stability diagrams in Figs. 3.6 and 3.7 are plotted differently due to the increasing directions of the gate biases). The two solid hyperbolic lines in Fig. 3.7 correspond to the two dark lines inside the circle in Fig. 3.6. At the lower (upper) branch, the chemical potential of the first (second) electron $\mu(1)$ [$\mu(2)$] is aligned with the source and drain chemical potentials μ_S and μ_D , and the first (second) electron is charged into the system. Here, we consider the linear transport regime in which $\mu_S \approx \mu_D$. At the crescents of the different branches, three different charge states coincide in terms of the total energy of the system; e.g., at the solid crescent on the lower hyperbolic branch, states “00”, “01”, and “10” coincide. For this reason, each crescent is called a triple point. The distance between the triple points on the lower (upper) branches is called the double-triple point (DTP) separation which consists of two parts: first, the part due to classical coulomb interaction within the electrons in the coupled dots denoted as V_{inter} (interdot coulomb matrix element), which can be extracted from the distance between the crossing point of the asymptotic lines to the lower and upper hyperbolic branches; second, tunnel coupling

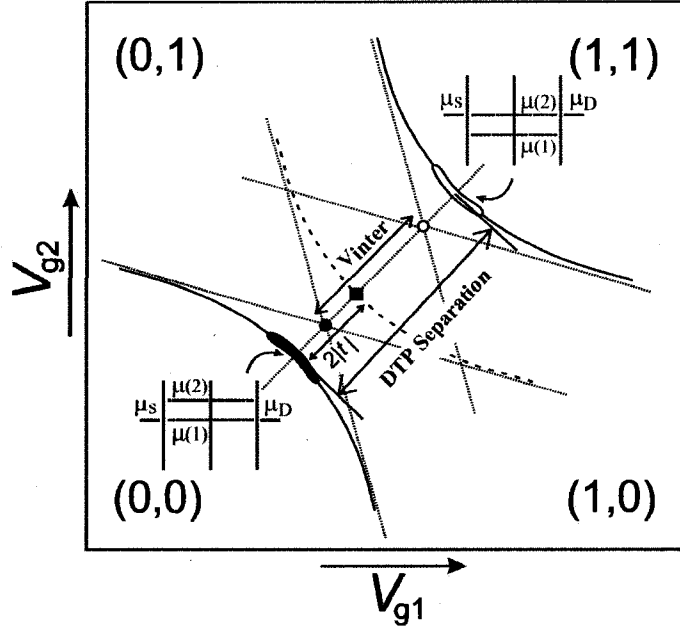


Figure 3.7 Schematic illustrating the structure of the stability diagram within the circle on Fig. 3.6. Note the order of the diagram is inverted compared to Fig. 3.6.

between the two dots denoted as t , which has a quantum mechanical origin. As the coupling strength between the two dots gets weaker, both V_{inter} and the tunnel coupling decrease, leading to a smaller DTP separation and a larger curvature of the chemical potential contour lines [14].

3.3.2 Stability diagrams in magnetic fields

Figure 3.8 displays the contour plots of $\mu(1)$ (lower branches) and $\mu^S(2)$ (upper branches) as functions of V_L and V_R at zero magnetic field. We choose constant values of $\mu(1) = \mu^S(2) = -18$ meV for $d = 50$ nm and $\mu(1) = \mu^S(2) = -16.5$ meV for $d = 60$ nm as the reference values of the chemical potential in the source/drain of the QD device. In Fig. 3.8 we can recognize four regions corresponding to four stable charge states with different numbers of electrons in each dot [the numbers in the parentheses in each region give the number of electrons in the (left, right) QD] separated by the chemical potential contours and the main diagonal $V_L = V_R$. Double-triplet points are indicated by solid dots. From

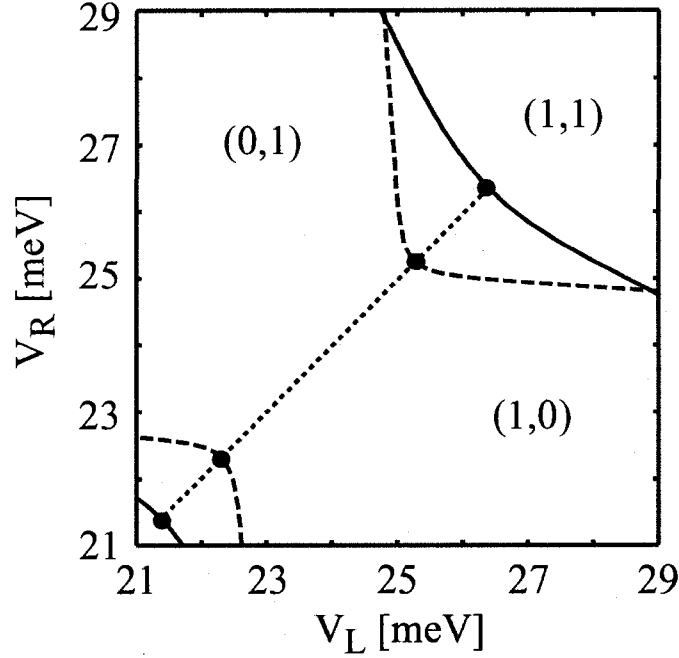


Figure 3.8 Contour plots of the chemical potentials $\mu(1)$ and $\mu^S(2)$ as functions of V_L and V_R for $d = 50$ nm (solid) and $d = 60$ nm (dashed). The turning points on the contour lines are indicated by solid dots and the dotted line is a guide for the eyes along the main diagonal ($V_L = V_R$). The numbers on the left (right) within parentheses give the electron numbers in the left (right) dot [the (0,0) region is located at the lower left corner below the $\mu(1)$ branch for $d = 50$ nm].

Fig. 3.8 we also observe that the DTP separation $\Delta V_L = \Delta V_R = 5.00$ meV in the $d = 50$ nm case is significantly larger than the corresponding value $\Delta V_L = \Delta V_R = 2.93$ meV in the $d = 60$ nm case. Furthermore, the curvature of the branches around the DTP is smaller for $d = 50$ nm than for $d = 60$ nm (see Table 3.1).¹ According to the general theory [14], a smaller DTP separation (or equivalently a larger curvature of the chemical potential contour lines) indicates a weaker interdot coupling which is consistent with our findings.

¹We fit the data along the chemical potential contour lines by a hyperbolic shape, $V_y = \pm a\sqrt{1 + (V_x/b)^2} + c$, where $V_x = (V_L - V_R)/\sqrt{2}$, $V_y = (V_L + V_R)/\sqrt{2}$, and a , b , and c are positive fitting parameters. We limit our fitting procedure to a region in which $|V_x| < 0.3$ meV and require $\epsilon = \max|V_y^{fit} - V_y^0| < 10^{-3}$ meV wherein V_y^{fit} and V_y^0 denote the fitting and original data, respectively. Hence, the magnitude of the second order derivative at $V_x = 0$ is given by $\kappa = (\partial^2 V_y / \partial V_x^2)|_{V_x=0} = |a/b^2|$, in units of meV^{-1} . We use this fitting scheme to obtain the data in Table 3.1. Even with magnetic fields, the hyperbolic fitting of the whole chemical potential contours gives $\epsilon < 0.05$ meV.

Table 3.1 Comparison of the magnitude of the second order derivative $\kappa(1)$ and $\kappa(2)$ of the chemical potential curves $\mu(1)$ and $\mu(2)$ near their turning points for various interdot separations and magnetic fields. Units of the data are in meV^{-1} . $\kappa^S(2)$ and $\kappa^T(2)$ denote the values for the singlet and the lowest triplet state, respectively. The Zeeman effect is included here.

B (T)	$d = 50 \text{ nm}$		$d = 60 \text{ nm}$	
	$\kappa(1)$	$\kappa^S(2) [\kappa^T(2)]$	$\kappa(1)$	$\kappa^S(2) [\kappa^T(2)]$
0	0.307	0.238 [0.269]	1.800	2.550 [2.52]
3	0.400	0.336 [0.349]	4.673	6.145 [7.463]
6	0.714	0.631 [0.659]	15.706	27.230 [37.141]

From the data in Table 3.1, we note that for $d = 50 \text{ nm}$, the curvature (magnitude) $\kappa(2)$ of the $\mu(2)$ curve is smaller than the curvature (magnitude) $\kappa(1)$ for $\mu(1)$, while in the $d = 60 \text{ nm}$ case $\kappa(1) < \kappa(2)$. This peculiar behavior can be clarified by noting that both $\kappa(1)$ and $\kappa(2)$ are determined by the differences between the corresponding curvatures of the total energy whose behavior in the voltage plane is discussed above. This indicates that in general, all else being equal, in the weak-coupling regime the curvature of the chemical potential for two electrons is larger than that one for one electron, $\kappa(2) > \kappa(1)$, while in the strong coupling regime, the opposite relationship $\kappa(2) < \kappa(1)$ holds.

In the presence of the magnetic field, the curvatures of the chemical potential contours also increase as can be seen in Fig. 3.9(a) and (b) where we again plot the chemical potential contours for $\mu(1)$, $\mu^S(2)$ and $\mu^T(2)$ at constant reference values of $\mu(1) = \mu^S(2) = \mu^T(2) = -18$ (-16.5) meV for $d = 50$ (60) nm at $B = 0, 3$ and 6 T . Note the order of the contours for $\mu^S(2)$ and $\mu^T(2)$ at different magnetic fields. As the magnetic field increases, the contours shift from the lower left corner to the upper right corner because the single-particle eigenenergies increase [19]. In addition to the curvature increase, the DTP separation becomes smaller at larger magnetic field for both singlet and the lowest triplet states [for the detailed explanation of this effect, see the discussion on Fig. 3.10(a)]. From the changes in the curvature and DTP separation, one concludes that the magnetic field indeed induces a quantum mechanical decoupling between the two dots and results in magnetic localization of electrons in each dot. By comparing the chemical potential curves

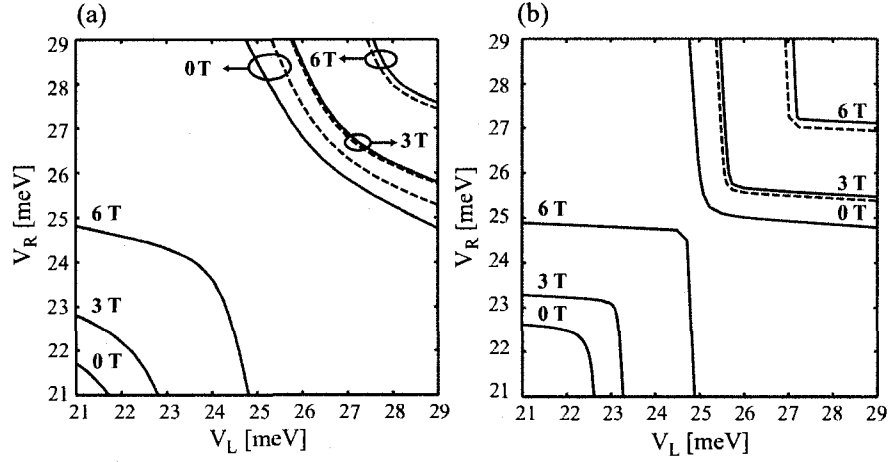


Figure 3.9 (a) $d = 50$ nm. Contour plots of the chemical potentials. Single-electron state: lower branches, solid curves. Two-electron singlet state: upper branches, solid curves. Two-electron triplet state: upper branches, dashed curves. Different magnetic fields are labeled in the figure. (b) Same as (a) but at $d = 60$ nm. The contour lines for singlet and triplet states at $B = 0$ are indistinguishable on the scale of the figure. The Zeeman effect is included here.

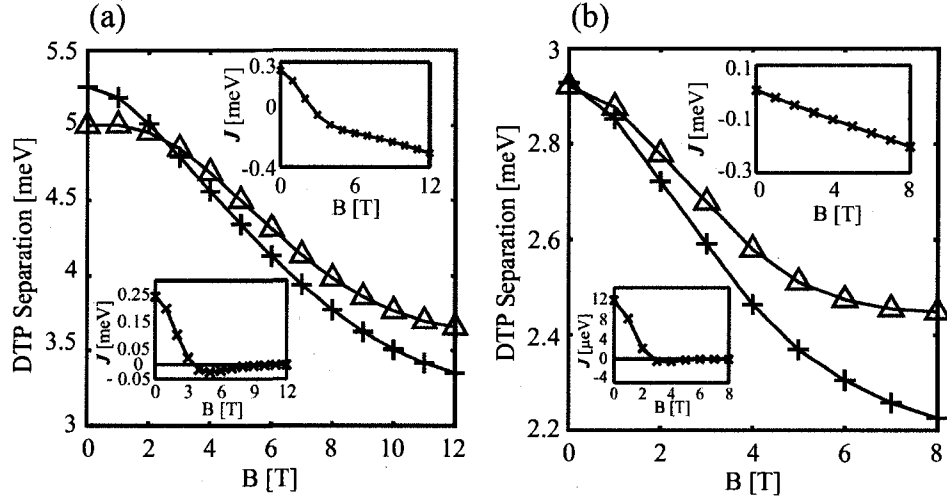


Figure 3.10 Double-triplet point separation projected along V_L (or V_R , $V_L = V_R$) axis as a function of the magnetic field B for (a) $d = 50$ nm and (b) $d = 60$ nm. The data for singlet and the lowest triplet states are labeled by “ Δ ” and “+”, respectively. The Zeeman effect is taken into account here. The upper (lower) inset in each figure shows the exchange energy J as a function of the magnetic field with (without) the Zeeman effect. The data in the insets are obtained at $V_L = V_R = 25$ meV.

in Fig. 3.9(a) with the corresponding ones in Fig. 3.9(b), we see that in the latter case the chemical potential contours have much larger curvatures than in the former case (see Table 3.1 for details) due to the increased interdot decoupling, and for each value of the magnetic field the DTP separation for $d = 60$ nm is more than 60% smaller than for $d = 50$ nm.

From Table 3.1, it is also shown that the curvatures $\kappa(1)$ and $\kappa(2)$ progressively increase as the magnetic field becomes larger. This is due to enhanced localization of electrons caused by the magnetic field. The magnetic localization in the weak coupling case became prevalent at lower fields than in the strong coupling situation [see lower insets of Fig. 3.10], which is manifested by a more rapid increase in the curvature of chemical potential contours.

The main panels of Figs. 3.10(a) and (b) show the extracted DTP separation along V_L (or V_R , $V_L = V_R$) axis as a function of magnetic fields for $d = 50$ nm and 60 nm interdot separations, respectively. In this calculation, the Zeeman effect is taken into account. In each plot the data are shown for the singlet and lowest triplet states. Note that at $B = 0$ the DTP separation for the singlet state is smaller than that for the lowest triplet state because the singlet is the ground state, while at larger B fields, the lowest triplet state becomes the ground state and the order of the DTP separations is reversed.

As a comparison with the data on the main panels of Figs. 3.10(a) and (b), in Figs. 3.11 (a) and (b) we show the same quantities without the Zeeman effect. In this case, at large magnetic field the DTP separations for singlet and the triplet states are identical because J vanishes due to the decoupling effects of the magnetic field. If Zeeman energy is taken into account, it will leave the singlet energy $E_0^S(2)$ ($S = 0$) unchanged, while lowering the single-particle energy $E_0(1)$ ($s_z = \frac{1}{2}$) and triplet energy $E_0^T(2)$ ($S_z = 1$) by $\frac{1}{2}g\mu_B B$ and $g\mu_B B$, respectively. Since the DTP separation is proportional to $\mu(2) - \mu(1) = E_0(2) - 2E_0(1)$, the Zeeman effect induces an increase in the singlet DTP separation, while its effect is cancelled out for the lowest triplet, which explains the difference between the data shown in the main panel of Fig. 3.9 and Fig. 3.11.

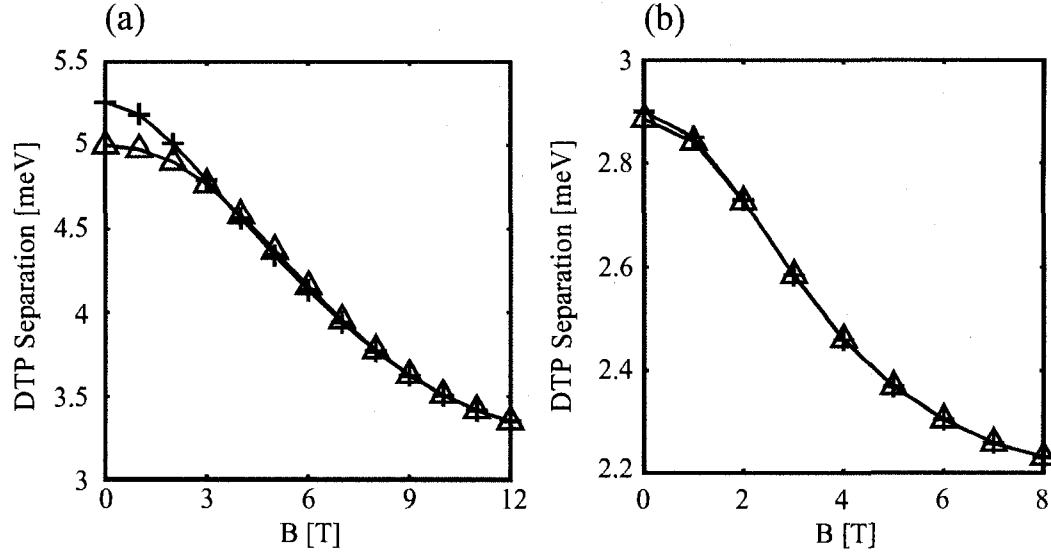


Figure 3.11 Same as the main panels of Fig. 3.10, but without the Zeeman effect.

The upper (lower) inset in Figs. 3.10(a) and (b) shows the corresponding exchange energy J as a function of the magnetic field calculated by Eq. (2.15) with (without) the Zeeman effect. In both cases, the Zeeman effect induces a linear dependence of J on B . However, in (a) given the strong coupling between the dots, the orbital contribution to J dominates at low B fields before being overcome by the Zeeman induced decrease at higher field; in (b), J is totally dominated by the Zeeman contribution, which decreases linearly with the B field. Comparison of the B field dependences of the DTP separation and exchange energy in the absence of the Zeeman effect in Fig. 3.10 shows that the latter saturates at much lower values of the magnetic field than the former. This is because the DTP separation is determined by the coulomb interaction between electrons which decreases as the electrons become localized by the magnetic field in individual dots. (Within the Heitler-London approximation, this decrease is proportional to B^{-2} , while the exchange energy in absence of the Zeeman effect approaches zero much faster than the coulomb interaction since it is proportional to the overlap between the individual electron wave functions that decays exponentially fast in strong magnetic fields [17].)

It is also interesting to compare the exact values of the exchange energy (see the insets in Fig. 3.10) with those extracted from the stability diagrams in magnetic fields using the

Hubbard model [16, 17]. According to this model, $J_{est} = 4t^2/(V_{intra} - V_{inter})$ where $2t$ is the tunnel (symmetric-asymmetric) splitting, V_{intra} and V_{inter} are the intradot and interdot coulomb interactions. From the data shown in Fig. 3.10, we estimate the value of the interdot coulomb interaction $V_{inter}^{50(60)} \approx 3.4$ (2.0) meV for $d = 50$ (60) nm, which is given by the DTP separation (for the lowest triplet state) in the limit of large magnetic fields. These numbers are in good agreement with the corresponding expectation values $\langle C(\mathbf{r}_1, \mathbf{r}_2) \rangle$ of the coulomb interaction matrix (3.5 and 2.2 meV, respectively) obtained from direct calculations, thereby confirming electron localization and QDs decoupling. Since at zero magnetic field, the DTP separation is equal to $2t + V_{inter}$, we obtain $2t^{50(60)} \approx 1.6$ (0.7) meV which is consistent with the energy differences between the two lowest single-particle levels of 1.9 (0.4) meV. As $V_{intra} \approx 8$ meV is given by the electron addition energy in one QD which is the distance between the “corners” of the linear region where single electron relocation occurs from one dot to the other in the $N = 2$ energy diagram (see Fig. 3.5), the estimated values of the exchange energy become $J_{est}^{50(60)} \approx 0.6$ (0.08) meV. These numbers are of the same order as the numerically exact values of 0.24 (0.012) meV, but they both significantly *overestimate* the computed data and therefore can only be used as a general guideline to gauge the magnitude of the exchange coupling in double QDs. The overestimation is due to the difference between coulomb energies in the singlet and triplet states that lowers the exchange energy [17], but which is not taken into account in the simple Hubbard model.

CHAPTER 4

COUPLED ELONGATED QUANTUM DOTS

In this chapter, we investigate coupled quantum dots with various aspect ratios $r = R_y/R_x$ in our model potential Eq. (2.1), which is a more realistic situation since in experiments the confinement potential deviate from a perfect circular shape (see, e.g., [45]). We first study coupled QDs with small aspect ratios, and then investigate QDs with relatively large aspect ratios. We not only analyze the exchange energy and stability diagram for QDs with different aspect ratios, but also study the interdot detuning effects, which are relevant to coupled QD experiments.

4.1 Coupled Dots with Small Aspect Ratio

4.1.1 Exchange energy

In Fig. 4.1(a), main panel, we plot the exchange energy as a function of the magnetic field for coupled QDs with different aspect ratios $r = R_y/R_x$, $R_x = 30$ nm. Here, we focus on the geometry effects and ignore the Zeeman effect which only introduces a linear shift to each curve. In insets (I), (II), and (III), the contour plots of the two-dimensional potential are displayed for $r = 1$, $r = 1.5$, and $r = 0.67$, respectively. Other parameters

Some of the material presented in this chapter was originally published. © 2007 IEEE. Reprinted, with permission, from L.-X. Zhang, D. V. Melnikov and J.-P. Leburton, "Engineering exchange coupling in double elliptic quantum dots," *IEEE Transactions on Nanotechnology*, vol. 6, pp. 250-255, 2007.

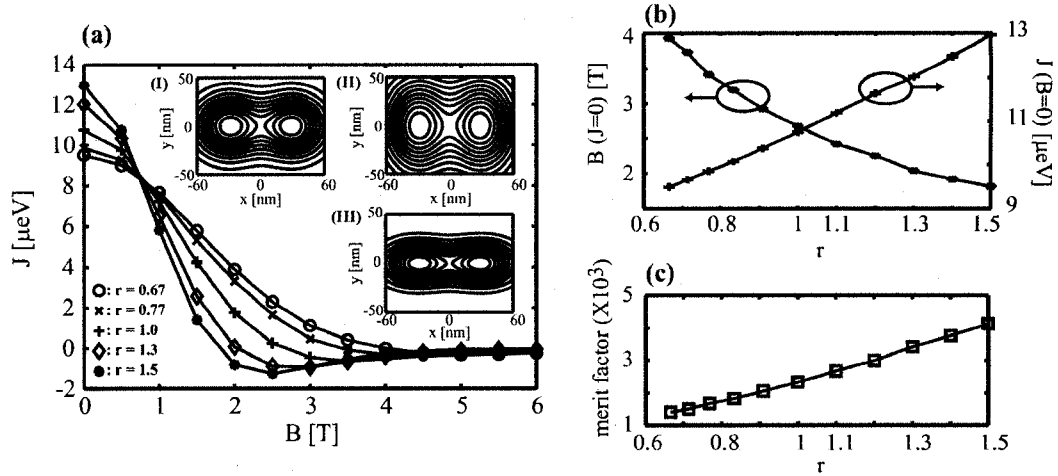


Figure 4.1 (a) Main panel: exchange energy dependence on the magnetic field for dots with different aspect ratios $r = R_y/R_x$, $R_x = 30$ nm. The insets (I), (II), and (III) show the contour plots of the confining potential for $r = 1$, $r = 1.5$, and $r = 0.67$, respectively. (b) Exchange energy maximum $[J(B = 0)]$ and magnetic field at singlet-triplet transition $[B_0 = B(J = 0)]$ and (c) merit factor $J/\hbar\omega_c$ ($\omega_c = eB_0/m_*c$) as a function of the aspect ratio $r = R_y/R_x$. For (a), (b), and (c), $V_L = V_R = 25$ meV, $d = 60$ nm, and the Zeeman effect is ignored.

for the model potential are $V_L = V_R = 25$ meV, $d = 60$ nm. It is observed that the magnitudes of the maximum and minimum values of the exchange energy are larger for a larger aspect ratio r because of enhanced interdot coupling in the y direction (perpendicular to the coupling direction x). As the aspect ratio r increases, the magnetic fields at the singlet-triplet transition point ($J = 0$), at exchange energy minimum, and at the saturation point of exchange energy all become smaller, leading to a more rapid variation of exchange energy as a function of B . In Fig. 4.1(b), as the aspect ratio increases from 0.67 to 1.5, the exchange energy maximum $[J(B = 0)]$ ramps up slowly from 9.5 to 13 μeV , while the magnetic field at the singlet-triplet transition point $[B_0 = B(J = 0)]$ decreases more rapidly from 4 to 1.75 T. For spin-based quantum computing, a larger $J(B = 0)$ and a smaller $B(J = 0)$ are both desirable because they offer more controllability of the quantum logic gate [10, 15]. Therefore, we define a merit factor, $J(B = 0)/\hbar\omega_c$, where $\omega_c = eB_0/m_*c$ is the cyclotron frequency at $J = 0$. In Fig. 4.1(c), we observe that the merit factor increases almost linearly with the aspect ratio, with an enhancement factor of more

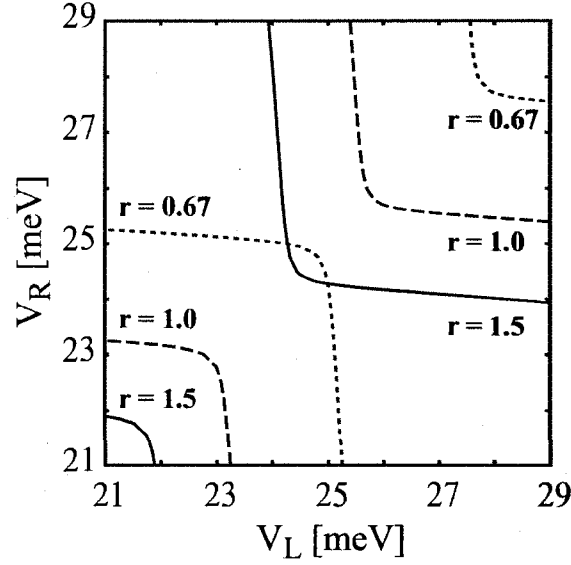


Figure 4.2 Contour plots of chemical potentials $\mu(1)$ (lower branches) and $\mu^S(2)$ (upper branches) at $r = R_y/R_x = 0.67$ (dotted), 1 (dashed), and 1.5 (solid). $d = 60$ nm, $R_x = 30$ nm, $B = 0$ T, reference chemical potential value: -17 meV.

than two as the aspect ratio increases from 0.67 to 1.5. It is also interesting to note that in Fig. 4.1(a) at $B \approx 0.8$ T, the values of the exchange energy for dots of different aspect ratios are very close to each other ($J \approx 8.5$ μeV), which implies that at this magnetic field the geometric factor plays a minor role in determining the exchange energy.

4.1.2 Stability diagrams

In Fig. 4.2, we plot the chemical potential contours for $\mu(1)$ (lower branches), $\mu^S(2)$ (upper branches) at constant reference value of $\mu(1) = \mu^S(2) = -17$ meV for $d = 60$ nm and $r = R_y/R_x = 0.67$ (dotted), 1 (dashed), and 1.5 (solid) with R_x fixed at 30 nm at zero magnetic field. As the aspect ratio decreases, the single-particle eigenenergies increase as a result of stronger confinement in each dot; hence, the chemical potential contours shift from the lower left corner to the upper right corner. The DTP separation is $\Delta V_L = \Delta V_R = 2.83$, 2.94, and 3.04 meV for $r = 0.67$, 1, and 1.5, respectively. Therefore, the coupling strength

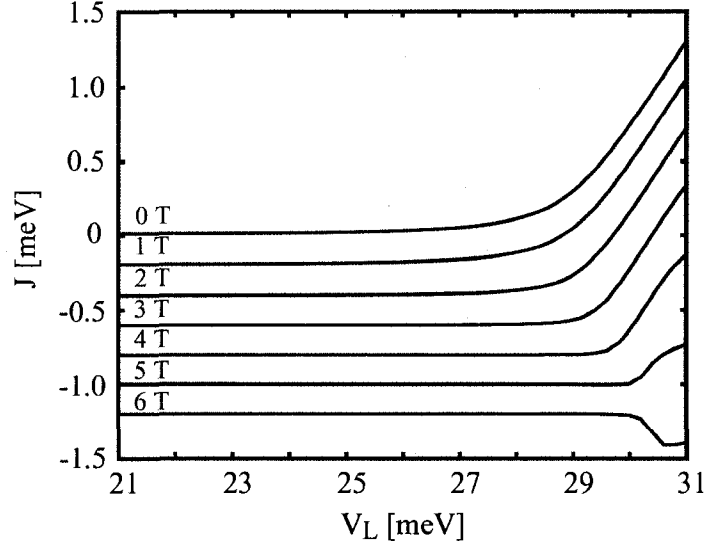


Figure 4.3 Exchange energy J as a function of V_L in the model potential at different magnetic fields. V_R is fixed at 21 meV. Other parameters are $d = 60$ nm, $R_x = R_y = 30$ nm. For clarity, curves for different B fields are shifted vertically by numerical value $-0.2B$ in the unit of meV.

is larger for a larger aspect ratio, which complies with earlier results of a larger exchange energy value at zero magnetic field for a larger aspect ratio.

4.1.3 Interdot detuning effects and electron localization

In Fig. 4.3, the exchange energy is shown as a function of V_L at $V_R = 21$ meV, or effectively as a function of interdot detuning $\epsilon = V_L - V_R$ for coupled circular dots ($R_x = R_y = 30$ nm, $d = 60$ nm) at different magnetic fields. The exchange energy at different magnetic fields is almost invariant for V_L from 21 to 29 meV. But for $V_L > 29$ meV, it increases superlinearly at $B = 0$ to 5 T and decrease superlinearly at $B = 6$ T. For $B = 5$ and 6 T, a trend of saturation is seen as well. The onset of the superlinearity is in accordance with the difference in the electron density between the singlet and triplet states. As shown in Fig. 4.4, as V_L becomes larger, the electron density of the singlet state is first well localized in the left dot while the electron density of the triplet state is still spread out in the two

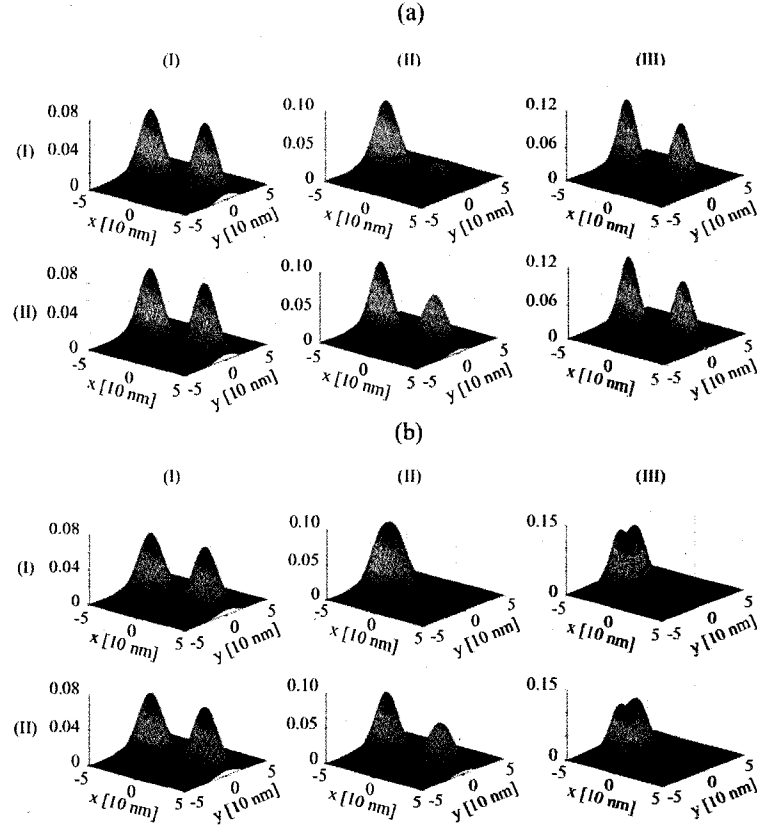


Figure 4.4 Two-dimensional electron density plots for (a) $r = R_y/R_x = 1$ and (b) $r = R_y/R_x = 1.5$. In each case rows (I) and (II) are for the singlet and triplet states, respectively. Different columns are for different parameters: (I) $V_L = V_R = 21$ meV, $B = 0$, (II) $V_L = 29$, $V_R = 21$ meV, $B = 0$, and (III) $V_L = 29$, $V_R = 21$ meV, $B = 6$ T. For all cases, $d = 60$ nm and $R_x = 30$ nm.

dots, and this difference in electron density becomes larger; therefore, the magnitude of the exchange energy increases.

In Fig. 4.5, we show the dependence of the exchange energy on V_L at $V_R = 21$ meV, for coupled elliptical dots ($R_x = 30$ nm, $R_y = 45$ nm, $d = 60$ nm) at different magnetic fields. The qualitative behavior of the exchange energy for $r = 1.5$ is similar to that for $r = 1$ in Fig. 3.4, except that the trend of saturation is seen to occur for a large interdot detuning value ($\epsilon = V_L - V_R > 9$ meV) at all the investigated magnetic fields. This is because for a larger aspect ratio, the effective size of each dot is larger and it is easier to localize the electron density for both the singlet and triplet states into a single dot, leading

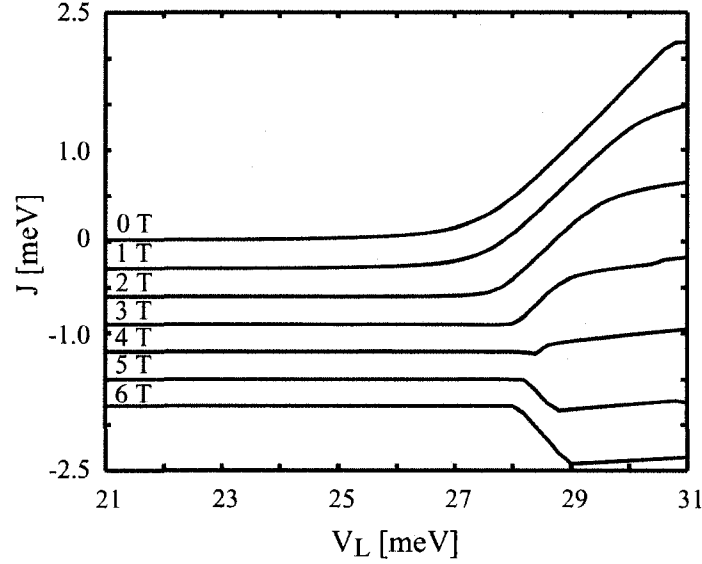


Figure 4.5 Exchange energy J as a function of V_L in the model potential at different magnetic fields. V_R is fixed at 21 meV. Other parameters are $d = 60$ nm, $R_x = 30$ nm, $R_y = 45$ nm. For clarity, curves for different B fields are shifted vertically by numerical value $-0.3B$ in the unit of meV.

to the saturation of the exchange energy in the meV range, which is typical in a single dot of the same size [19, 38]. Here, we note that the general trend of the superlinear increase of the exchange energy as a function of the interdot detuning agrees with recent experimental findings [15].

In Fig. 4.4, we show the two-dimensional electron density plots for (a) $r = R_y/R_x = 1$ and (b) $r = R_y/R_x = 1.5$. In each case rows (I) and (II) are for the singlet and triplet states, respectively. Different columns are for different parameters: (I) $V_L = V_R = 21$ meV, $B = 0$, (II) $V_L = 29$, $V_R = 21$ meV, $B = 0$ and (III) $V_L = 29$, $V_R = 21$ meV, $B = 6$ T. In all cases, $d = 60$ nm and $R_x = 30$ nm. In the following we compare (a) and (b) by columns with different external parameters: at zero interdot detuning ($V_L = V_R$) and $B = 0$ [column (I)], for both (a) and (b), the electron density of both the singlet and triplet states shows two peaks localized at the center of each dot which are symmetric with respect to $x = 0$. The exchange energy for (a) and (b) is $J = 15$ and $J = 19$ μeV , respectively, which are of comparable order of magnitude. At nonzero interdot detuning ($V_L - V_R = 8$

meV) and $B = 0$ [column (II)], the singlet electron density in (a) for $r = 1$ shows a secondary peak in the right dot, while this peak is absent for a larger aspect ratio $r = 1.5$ in (b). This is because for a larger aspect ratio, the onset value of the interdot detuning for two-electron localization into one dot is smaller (see discussion on Figs. 4.3 and 4.5 above) due to the relaxation of the confinement potential in the y direction. In this column, the triplet electron density profiles for both cases show a secondary peak in the right dot and are similar to one another. The calculated exchange energy for (a) and (b) is $J = 297$ and $J = 1050 \mu\text{eV}$, respectively, in accordance with the observed differences in the electron densities between the singlet and triplet states for these two cases. At nonzero interdot detuning ($V_L - V_R = 8 \text{ meV}$) and $B = 6 \text{ T}$ [column (III)], there is a drastic difference of the electron density profiles between (a) and (b): in (a) for both singlet and triplet the electron density shows a higher (lower) peak localized at the center of the left (right) dot, while in (b), for both singlet and triplet the electron density is completely localized into the left dot with two equal peaks at $y = \pm 8 \text{ nm}$, $x = -30 \text{ nm}$. Due to the large overlap of the electron wavefunctions in the latter case, the exchange interaction $J = -577 \mu\text{eV}$ is three orders of magnitude larger than $J = -1.22 \mu\text{eV}$ in the former case. We note that different density profiles result from the combined effects of the confinement potential and magnetic field that are well captured in our exact diagonalization method by incorporating single-particle excited states in both x and y directions into constructing the two-electron wavefunctions. We also note that a simple Heiter-London calculation, which only takes into account the ground state wavefunctions, will not suffice.

4.2 Coupled Dots with Large Aspect Ratio

4.2.1 System energy and exchange energy

Figure 4.6 top panels show the potential contour plots for aspect ratios $r = 1$ (left), $r = 4$ (middle), and $r = 8$ (right). As r increases, the potential becomes more elongated in the y -

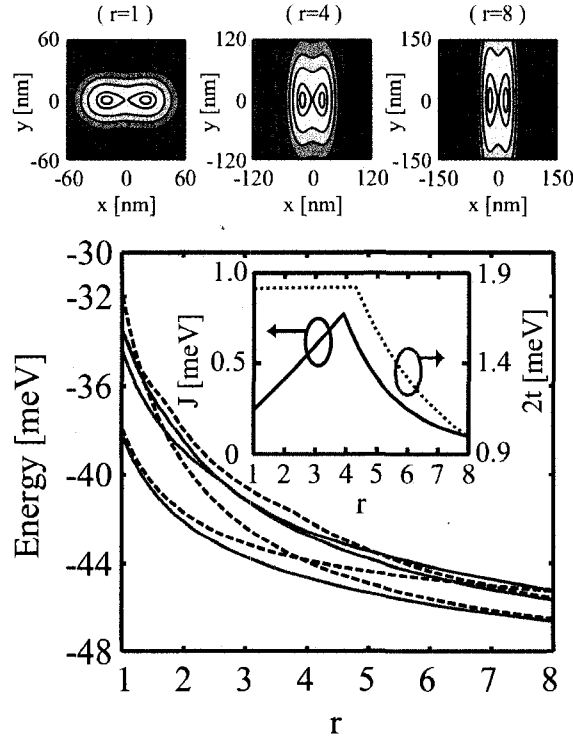


Figure 4.6 Top panels: potential contour plots of coupled QD with $r = 1$ (left), $r = 4$ (middle), and $r = 8$ (right) at $d = 50$ nm. Darker regions correspond to higher potential. Lower panel: three lowest singlet (red, solid lines) and triplet (blue, dashed lines) energy levels as a function of QD aspect ratio r at $d = 50$ nm. The inset shows r dependence of the exchange energy J (blue, solid) and tunnel coupling $2t$ (red, dotted). Other parameters are the same for all panels, which are $V_L = V_R = 25$ meV, $R_x = 30$ nm, $B = 0$.

direction, while the effective interdot distance (i.e., the x -distance between the two minima of the potential) and the interdot barrier height remain constant values of 40 nm and 1.98 meV, respectively.

In lower panel of Fig. 4.6, we plot the three lowest singlet (red, solid) and triplet (blue, dashed) energy levels as a function of r . With increasing r , the single-particle energies decrease (not shown), resulting in the decrease of the two-particle energy levels. We note that the lowest energy of the singlet state (E_0^S) decreases smoothly with r , while the lowest energy of the triplet state (E_0^T) exhibits a kink at $r = 3.9$ because of the crossing of the lowest two triplet state energy levels. Here, “singlet state” and “triplet state” refer to the singlet and triplet states lowest in energy, respectively. This kink results in a sharp variation

in the exchange energy dependence on r , which is shown in the inset of the lower panel of Fig. 4.6. In the same inset, we show the variation of the tunnel coupling $2t = e_1 - e_0$. Here, e_0 (e_1) denotes the single-particle ground (first excited) state energy. For $r \leq 4.3$, the single-particle ground and first excited states have s and p_x characters, respectively, and $2t$ barely increases from 1.8105 to 1.8114 meV with increasing r because the energy contributions from the y -direction to e_0 and e_1 cancel out. For $r > 4.3$, the single-particle first excited state bears a p_y character, due to which $2t$ decreases monotonically with r .

The behavior of $2t$ and J as r increases is rather counterintuitive because one expects a decrease in J as $2t$ decreases, which is indeed the case as one increases the interdot barrier height or interdot distance [cf. Fig. 5.3 on page 62]. Here, because of the effects of the 2D confinement potential variation and the resulting coulomb interaction, we have observed a specific situation in which the exchange energy is increasing while the tunnel coupling remains constant (inset of lower panel of Fig. 4.6). Another important observation from Fig. 4.6 is that the exchange energy is enhanced as the aspect ratio r is increased as long as r is not larger than a critical value; e.g., in the case of $d = 50$ nm, the exchange energy is enhanced by a factor larger than 3 as r increases from 1 to 3.9. Further analysis shows that even stronger J enhancement (of a factor more than 10) is possible for $d = 60$ nm. This enhancement of J could benefit quantum computing because the quantum logic gate operation would be faster for a larger J ($J\tau_s/\hbar = \pi$, where τ_s denotes the operation time).

4.2.2 Density and spectral function

In this section, we explain the crossing of the lowest two triplet levels in the lower panel of Fig. 4.6 to find the origin of the sharp variation of the exchange energy. By illustrating the electron density and spectral decomposition of the two-electron wavefunction, we will show that the sharp variations exemplify the Pauli principle and the many-body nature of the wavefunction.

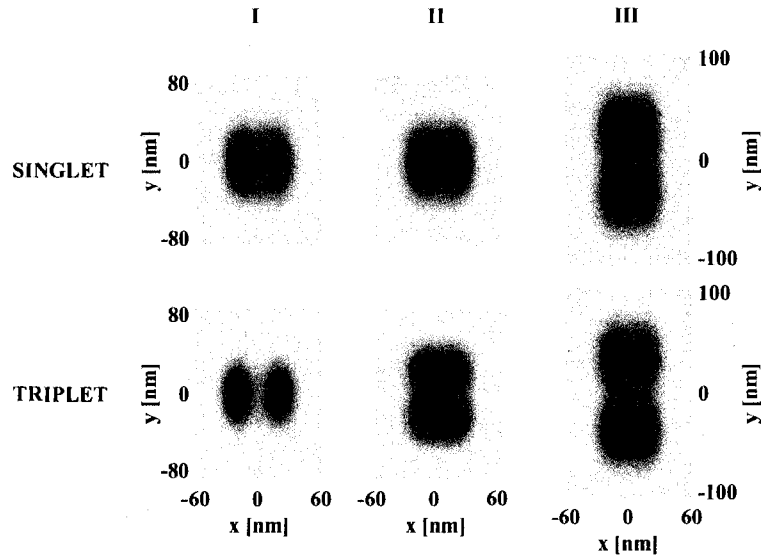


Figure 4.7 Contour plots of the electron density for singlet (upper row) and triplet (lower row). Columns I, II, and III are for $r = 3.9$, $r = 4$, and $r = 8$, respectively. Darker regions correspond to higher electron density.

Figure 4.7 shows the contour plots of the electron densities of the singlet (upper row) and triplet (lower row) states for $r = 3.9$ (column I), $r = 4$ (column II), and $r = 8$ (column III). At $r = 3.9$, the electron densities of the singlet and triplet states show two peaks separated in the coupling (x) direction, and it is seen that the two electrons localized in the left and right dots are more coupled in the singlet state than in the triplet state. For $1 \leq r < 3.9$, the singlet and triplet densities are similar to those at $r = 3.9$, and increasing r simply increases the density extension along the y -direction. At $r = 4$, the singlet density is indiscernible from that at $r = 3.9$. However, from $r = 3.9$ to $r = 4$, the triplet state density changes drastically from two peaks localized in the left and right dots (the separation of two peaks in the x -direction is ~ 40 nm) to four peaks separated along both x and y directions. The separation of the two peaks on the top (bottom) in the x direction is 20 nm; the separation of the two peaks on the left (right) in the y direction is 40 nm.

Although one can see the correlation between the triplet level crossing (lower panel of Fig. 4.6), which gives an abrupt variation of the triplet ground state energy, and the abrupt

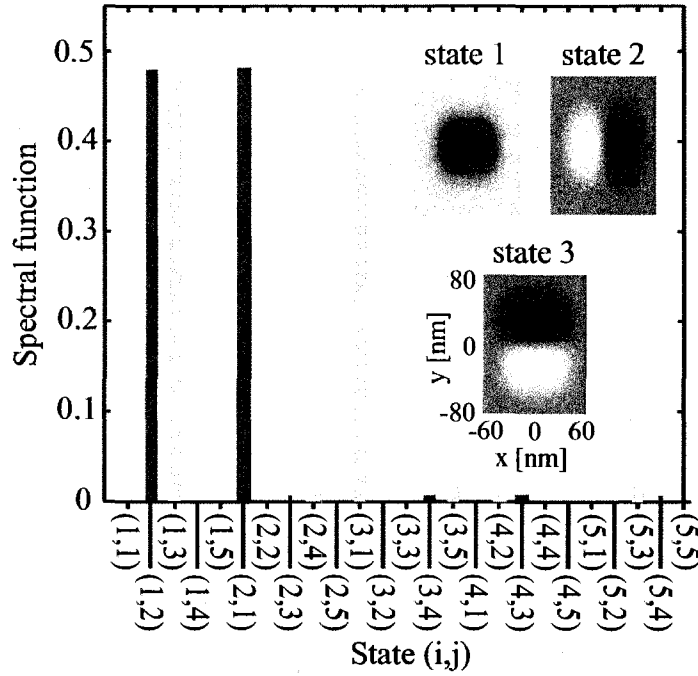


Figure 4.8 Spectral decomposition of the two-electron wavefunction onto different single-particle pairs. The red (dark) columns are for $r = 3.9$, while the yellow (bright) columns are for $r = 4$. The inset shows the contour plots of the lowest three single-particle states in ascending order of energy for both $r = 3.9$ and $r = 4$.

density variation (Fig. 4.7), this does not provide a fundamental explanation of the crossing behavior. In order to understand this, in Fig. 4.8, main panel, we plot the expansion coefficient (spectral function) of the two-electron wavefunction onto different single-particle pairs (see Appendix A and [54]). It is seen that at $r = 3.9$ the triplet mainly occupies the $(1, 2)$ $[(2, 1)]$ pair, while at $r = 4$ it mainly occupies the $(1, 3)$ $[(3, 1)]$ pair. Here, 1, 2, and 3 denote the single-particle states in ascending order of energy. The inset shows these states have s , p_x , and p_y characters, respectively. This ordering does not change as r changes from 3.9 to 4. Therefore, the abrupt variation of the triplet ground state is due to a sudden transition of the two-electron wavefunction from occupying an sp_x pair to an sp_y pair, which is observed as a kink in the r dependence of the lowest triplet state energy [lower panel of Fig. 4.6].

Column III in Fig. 4.7 shows that at $r = 8$, both the singlet and triplet densities exhibit four peaks separated in both the x and y directions. Our analysis shows that from $r = 4$ to $r = 8$, the left and right peaks in the singlet state density gradually separate into four peaks, and the separation between the top two and bottom two peaks in the triplet state density smoothly increases. Here, we see that the coulomb interaction plays an important role in determining the electron density: as the confinement is weak in both x and y directions, the electrons are localized into four “corners” along the two diagonals, minimizing the coulomb energy between them [55, 56, 57].

4.2.3 Von Neumann-Wigner theorem

In Fig. 4.7, we find that at $r = 3.9$, the occupation of the triplet ground state abruptly transitions from occupying an sp_x pair to an sp_y pair, leading to the abrupt variation of the triplet ground state energy. Because the triplet state wavefunction is constructed by

$$\Psi^T(\mathbf{r}_1, \mathbf{r}_2) = \sum_{ij} \beta_{ij} [\psi_i(\mathbf{r}_1)\psi_j(\mathbf{r}_2) - \psi_j(\mathbf{r}_1)\psi_i(\mathbf{r}_2)], \quad (4.1)$$

and the p_x and p_y states have opposite symmetry with respect to $y = 0$, one expects the triplet ground state wavefunction abruptly changes from even to odd in the y -direction. In order to confirm this, we explicitly calculate the y -parity

$$\langle \hat{P}_y \rangle = \langle \Psi^T(x_1, y_1; x_2, y_2) | \Psi^T(x_1, -y_1; x_2, -y_2) \rangle \quad (4.2)$$

of the triplet ground and first excited states near $r = 3.9$. Here, (x_1, y_1) , (x_2, y_2) are the coordinates of the first and second electrons, respectively. By this analysis, we indeed find that at $r = 3.9$, the y -parities of these states interchange their signs.

The abrupt variation of the triplet state symmetries exemplifies the general von Neumann-Wigner theorem which states that under perturbation in the Hamiltonian, the energy levels

of states bearing different symmetries can intersect, while the energy levels of states bearing the same symmetry cannot intersect [58, 59]. This fundamental theorem has found successful applications in the spectroscopy of alkaline salts [60], the interpretation of the Zeeman spectrum of hydrogen molecules [61], and more recently in the explanation of the magnetic anisotropy in thin metallic films [62].

In our case, the perturbation in the system Hamiltonian is induced by the elongation of the confinement potential in the y -direction. Before and after the crossing (at $r = 3.9$) of the lowest two triplet levels, the triplet ground state in fact occupies two states with complete opposite y -symmetry. We note that the von Neumann-Wigner theorem is equally applicable to the evolution of the singlet energy levels. Because the two electrons in the singlet states mainly occupy the same orbitals, e.g., the ss , $p_x p_x$ pairs, etc., neighboring energy levels always bear the same Cartesian symmetries and can only anticross, as predicted by the von Neumann-Wigner theorem. In Section 4.2.6 on page 62, we will see another specific example as a result this general theorem, in which case the perturbation is induced by the interdot detuning.

4.2.4 Spin phase diagram

At magnetic field $B = 0$, the ground state of a two-electron system is always a singlet, as predicted by a general theorem [63] and shown by our simulation result (see Fig. 4.9). If magnetic field effect is taken into account (without the Zeeman effect), one expects singlet-triplet transition in which triplet becomes the ground state at high magnetic field. In this section we present the exchange energy J as a function of both r and B . By identifying the different regions where J assumes different signs, we find the two-electron ground state spin state (either $S = 0$ or $S = 1$) as a function of r and B , the so-called spin phase diagram [19, 64].

In Fig. 4.9, we plot the exchange energy J as a function of the QD aspect ratio r and the magnetic field B perpendicular to the xy -plane (the Zeeman effect is excluded here).

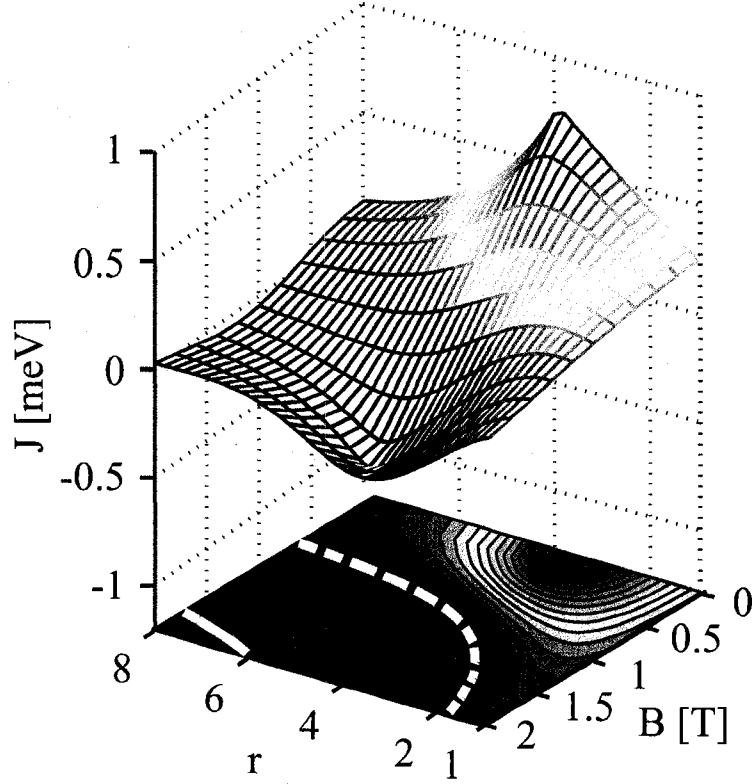


Figure 4.9 Mesh (contour) plot of the exchange energy J as a function of QD aspect ratio r and the magnetic field B . The thick white curves (solid and dashed) on the contour plot correspond to $J = 0$.

At fixed r , as B increases, J decreases from its maximum value to become negative and saturate at very large magnetic field, which follows the singlet-triplet transition behavior studied in other works [17, 18, 19, 20, 21, 33, 53]. It is seen that at intermediate r ($r \sim 4$), J changes much faster with B than at very small or large r . We note that the prominent B field effect on J at intermediate r values is associated with the 2D confinement of the QDs; i.e., near $r = 4$ the single-particle level separation in the x - and y -directions is comparable [cf. Fig. 4.7, lower inset]. With increasing r , the relative change of J is small for $B \sim 1$ T while much larger for $B \sim 0$ T or $B \sim 2$ T. The kink in J at $B = 0$, due to the crossing of two lowest triplet levels, does not exist for $B \neq 0$ T because the magnetic field couples single-particle states with different Cartesian symmetries, thereby removing the condition for the crossing of the lowest two triplet states.

We note that the first singlet-triplet transition (at which J first crosses zero as B increases from zero at fixed r) occurs at a smaller B value as r increases, which is shown by the thick white dashed curve on the contour plot in Fig. 4.7. One can understand the dependence of singlet-triplet transition B field value on r by the following observation: in the absence of the B field, as r increases the single-particle energy spacing decreases, which results in a smaller exchange energy, and, for a larger r , a smaller magnetic field is needed to further decrease the single-particle spacing and bring the triplet state to the ground state with the aid of the coulomb energy difference between the singlet and triplet states. At higher magnetic field and larger r , we observe another contour line for $J = 0$ (thick solid white curve at the lower left corner). The reappearance of the singlet state as the ground state is reminiscent of the singlet-triplet oscillation found for a two-electron single dot and also reported elsewhere for two-electron double dots with strong confinement [19, 64, 65]. Figure 4.9 clearly shows the total spin of the two electrons for different B and r ; i.e., the two-particle ground state is a singlet (triplet) state outside (in between) the two white curves. In the investigated ranges of r and B , J assumes a maximum (minimum) value of 0.773 (−0.372) meV at $r \approx 3.9$, $B \approx 0$ T ($r \approx 4.4$, $B \approx 1.6$ T). The J values in between the minimum and maximum set a theoretical range in which the exchange energy is tunable under a symmetric bias configuration.

4.2.5 Stability diagrams

In Fig. 4.10, upper panels, we plot the stability diagrams [14] of the coupled QDs for $r = 1$ (left), $r = 3$ (middle), and $r = 5$ (right). The solid curves indicated by arrows show the computed contours where chemical potentials of the first electron (red), the second electron in the singlet state (green), and second electron in the triplet state (blue) are equal to the reference value [$\mu(1) = \mu^S(2) = \mu^T(2) = -21$ meV]. According to the general shape of the stability diagram for coupled QDs [14], we place dotted straight lines on the diagrams to separate different charge states indicated by discrete electron numbers on the

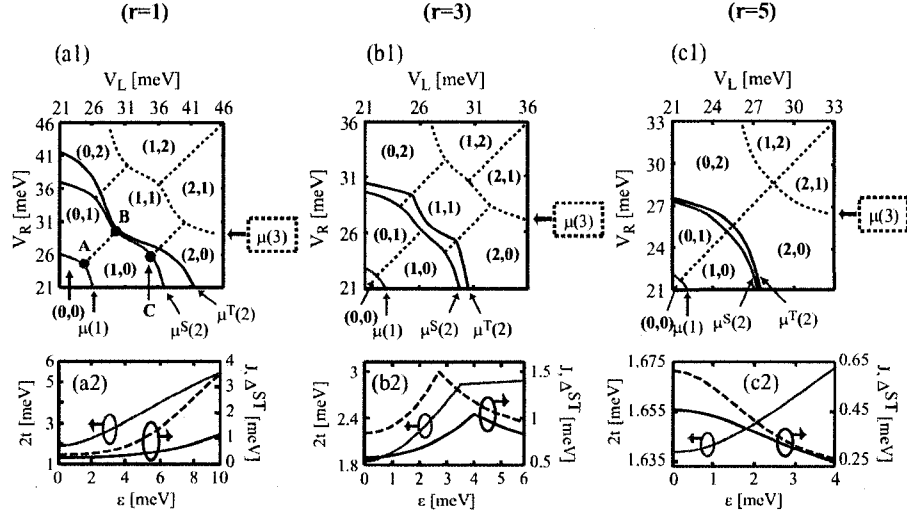


Figure 4.10 Top panels: stability diagrams for $r = 1$ (left), $r = 3$ (middle), and $r = 5$ (right). In each diagram, the red, green, and blue curves (solid) are computed contour lines at which the chemical potentials $\mu(1)$, $\mu^S(2)$, and $\mu^T(2)$, respectively, equal to the reference value $\mu_{ref} = -21$ meV. Curves for different chemical potentials are also indicated by arrows. The dashed lines are a guide for eyes separating different stable charge states. Note that the exact locations of the $\mu(3)$ curve and (1, 2), (2, 1) regions are not computed. In the leftmost upper panel, we also indicate the double-triple points A and B. Point C is where the $\mu^S(2)$ curve has the largest curvature for $V_L \neq V_R$. The bottom panels show the computed $2t$ and J (solid curves) as a function of interdot detuning $\epsilon = V_L - V_R$ from the center of the (1, 1) region for corresponding dot aspect ratios. The dashed curves on the bottom panels show the separation (Δ^{ST}) between the contour lines of $\mu^S(2)$ and $\mu^T(2)$ projected along the main diagonal of the stability diagram above as a function of interdot detuning $\epsilon = V_L - V_R$. All data are obtained at $R_x = 30$ nm, $d = 50$ nm, and $B = 0$ T.

left and right dots; e.g., (0, 1) means zero electrons on the left dot and one electron on the right dot. Specifically, the boundaries between the (1, 1) and (0, 2) [or (2, 0)] states are taken extending from the point on the $\mu^S(2)$ curve at which the curvature is the largest for $V_L \neq V_R$, e.g., point C on the upper left panel and parallel to the main diagonal. In the absence of magnetic field ($B = 0$), the $\mu^S(2)$ curve is the boundary between one and two electrons in the system (in the linear transport regime wherein the source and drain chemical potentials are nearly the same). Based on this fact and the separation between the (0, 0) and two-electron states along the main diagonal, we extrapolate to get the boundary between two- and three-electron states [green dotted curve indicated by $\mu(3)$]. Here, we note that the boundary between two- and three-electron states is not computed. In other

words, the $\mu(3)$ curves on the diagrams only serve to delimit the charge states for two electrons in the coupled dots.

As r increases, the crossing points of the $\mu(1)$, $\mu^S(2)$, and $\mu^T(2)$ curves with the main diagonal shift to smaller $V_L = V_R$ values because the single-particle energies decrease as r increases. For the same reason, the double-triple point (DTP) separation, i.e., the separation between the crossing points of $\mu(1)$ and $\mu(2)$ curves with $V_L = V_R$, decreases with r . For the singlet (triplet) state, the DTP separation measured in $\Delta V_L = \Delta V_R$ is 5.181 (5.269), 4.128 (4.725), and 3.473 (3.907) for $r = 1, 3$, and 5, respectively. If one takes a measure of the $(1, 1)$ region size as the distance between the two points where the chemical potential contour curve has the largest curvature, e.g., point C on the upper left panel, it is interesting to note that as r increases, the $(1, 1)$ stable region shrinks and finally vanishes. This is because it becomes progressively easier to localize both electrons into one dot as r increases.

After locating the different charge stable regions on the stability diagram, one can now investigate the interdot detuning effect by deviating from the center of the $(1, 1)$ region and going along a line perpendicular to the main diagonal, i.e., $V_L + V_R = \text{constant}$. Such detuning effects are important as two electrons transfer to a single dot, which is a key step in spin coherent manipulation and spin-to-charge conversion in two-electron double dot experiments for quantum logic gate applications [11, 15].

In Fig. 4.10, lower panels, we observe a drastic difference in tunnel coupling $2t$ and exchange coupling J as a function of detuning $\epsilon = V_L - V_R$ between different dot aspect ratios. In order to understand the behavior of $2t$ and J for the different cases, we resort to the general discussion that the exchange energy results from the competing effects of single-particle separation and the difference in the coulomb interaction between the singlet and triplet states. While the single-particle separation is determined by the strength of the confinement potential, the coulomb energy difference can be qualitatively deduced from the electron density in the singlet and triplet states.

The above qualitative analysis of $2t$ and J is well applicable to cases for $r = 1$ and $r = 5$: for both $r = 1$ and 5 , $2t$ increases as a result of stronger confinement due to detuning. For $r = 1$, the density variation due to detuning is similar in singlet and triplet so that the coulomb energy difference does not change significantly. Consequently, the exchange energy increases with ϵ . For $r = 5$, the spatial configuration of the densities of singlet and triplet are quite different at $\epsilon = 0$: the singlet density is localized at the two minima of the potential, while the triplet density is localized at the four “corners,” similar to the $r = 4$ case shown in Fig. 4.7. As detuning is introduced, both electrons localize into a single dot, leading to an enhanced coulomb energy difference. This counteracts the increasing $2t$ and results in the decrease of J with ϵ .

For $r = 3$, however, the behavior of $2t$ and J is complicated by the energy ordering of the single-particle p_x and p_y states: the kink at $r = 3.6$ in $2t$ is because the p_y state replaces the p_x state to be the first excited state, while the kink at $r = 4.1$ in J is due to the sudden transition of the triplet state from occupying an sp_x to an sp_y pair. Except for the kink behavior, the qualitative analysis of $2t$ and J also applies to the $r = 3$ case: as ϵ increases, $2t$ increases (before and after the kink) as a result of enhanced confinement. We find that the exchange energy behavior is similar to the $r = 1$ ($r = 5$) case before (after) the kink by considering the electron density variations.

In transport experiments on quantum dots, it is difficult to measure the system energy directly. Instead, the chemical potential contour curves (given by the single-electron charging instances) are probed to obtain an indirect measurement by introducing a linear factor between chemical potentials and system energy [14, 26]. For example, the difference Δ^{ST} between the $\mu^S(2)$ and $\mu^T(2)$ curves on the stability diagram is an experimental measure of the exchange energy [66]. In Fig. 4.10, we show that although the general behavior of Δ^{ST} and the calculated J as a function of ϵ are similar to each other, their magnitudes differ significantly. The reason for this difference is twofold: (1) Δ^{ST} gives a measurement on the scale of V_L and V_R , which needs to be scaled by a linear factor to obtain its corre-

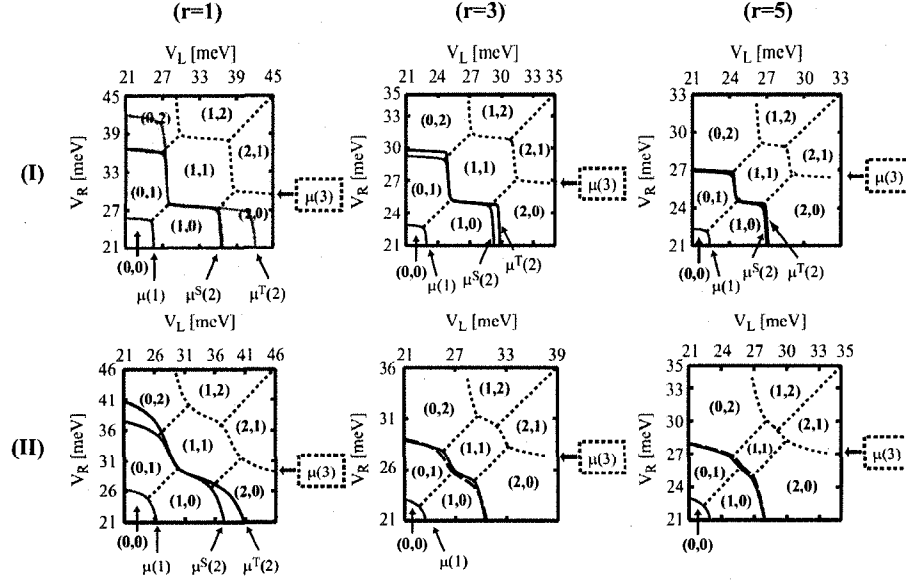


Figure 4.11 Same as the stability diagrams in Fig. 4.10, but for row (I) $d = 60$ nm, $B = 0$ T. (II) $d = 50$ nm, $B = 2$ T.

sponding value in terms of the system energy. (2) Clearly, Δ^{ST} and J are obtained under different bias conditions (V_L and V_R values); especially for Δ^{ST} , at a fixed detuning value ($V_L - V_R = \text{constant}$), the bias condition is different for singlet and triplet. The magnitude difference between Δ^{ST} and the calculated J observed in Fig. 4.10 is due to both reasons above, while the displacement of the kink location in Fig. 4.10(b2) is mainly due to the second reason. The above argument should be taken into account when one compares the data between transport experiments and electronic energies calculated theoretically.

In Fig. 4.11, we show the computed stability diagrams for a larger interdot distance (row I, $d = 60$ nm, $B = 0$ T) and under a nonzero magnetic field (row II, $d = 50$ nm, $B = 2$ T). Without going into further analysis, which would be similar to that of Fig. 4.11, we point out that at larger interdot distance, because the dots are more decoupled, the chemical potential contour lines exhibit sharper corners instead of the more smooth variations for smaller interdot distance. The (1,1) region is seen to shrink but not vanish at $r = 5$ as it is comparably difficult to localize both electrons into one dot. For stability diagram under nonzero magnetic field, the (1,1) region barely exists at $r = 5$, due to the decoupling

effects from the compression of single-particle orbitals by the magnetic field. We also observe that the ordering of the $\mu^S(2)$ and $\mu^T(2)$ contour lines changes due to single-triplet transition.

4.2.6 Detuning effects

In Section 4.1.3, we have discussed the interdot detuning effects on QDs with relatively small aspect ratios. In this section, we extend the discussion to dots with large aspect ratios and provide detailed analysis of the system energy and density variations with respect to interdot detuning. The results turn out to give a sound explanation of the exchange energy behavior in Fig. 4.10 on page 45 and another specific exemplification of the von Neumann-Wigner theorem. In this section, we focus on QDs with weak interdot coupling ($R_x = 30$ nm, $d = 60$ nm).

Figure 4.12, top panels, show the potential contour plots for circular ($r=1$, left two panels) and elliptical ($r=3$, right two panels) QDs under symmetric and asymmetric biases. As ϵ increases the coupled QD system becomes effectively a single QD centered at the lowest point of the confinement potential (the left dot center for both cases). In Fig. 4.12, bottom panels, we plot the two lowest singlet and the two lowest triplet energy levels for the coupled QDs with $r = 1$ [Fig. 4.12(a)] and $r = 3$ [Fig. 4.12(b)] as a function of detuning ϵ . All energy levels decrease as V_L increases because the single-particle energies that give the main contribution to the two-electron energy are lowered with the electric potential. For both aspect ratios, $r = 1$ and 3, and at small ϵ [$21 \leq V_L \leq 29$ meV in Fig. 4.12(a) and $21 \leq V_L \leq 25$ meV Fig. 4.12(b)], we observe singlet and triplet energies decrease with nearly the same slope as ϵ increases. Then, the singlet energy slope becomes steeper as both electrons localize into one QD, which are indicated by points U and U' in Fig. 4.12. For $r = 1$ and $V_L > 34$ meV, the slope of the triplet energy increases in value (yet smaller than that of singlet), while for $r = 3$ the triplet energy experiences a *sudden* change of slope at $V_L = 25.46$ meV [point V' in Fig. 4.12(b)], and with increasing V_L values afterwards, the

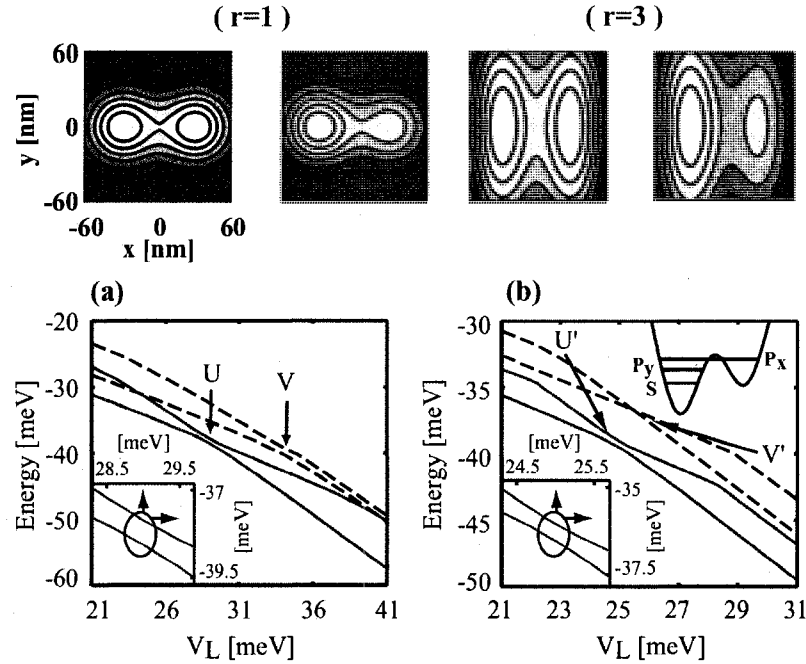


Figure 4.12 Top panels: potential contour plots of coupled QD with $r = 1$ (left two) and $r = 3$ (right two). For each r , the panel on the left (right) is for $V_L = V_R = 21$ ($V_L = 31$, $V_R = 21$) meV. (a) $r = 1$. Main panel: two lowest singlet (red, solid lines) and triplet (blue, dashed lines) energy levels as a function of detuning. U (V) indicates the anticrossing point for the two lowest singlet (triplet) levels. Lower inset: zoom-in region near the anticrossing point of the singlet energy levels. (b) $r = 3$. Main panel and lowest inset same as in (a) but for $r = 3$. U' (V') indicates the anticrossing (crossing) point of the two lowest singlet (triplet) energy levels. Upper inset: three lowest single-particle energy levels in asymmetric confinement. In (a) and (b), the singlet energy levels are lowered by 3 meV for clarity.

spacing between singlet and triplet energies first decreases, and then gradually increases for $V_L \geq 27.2$ meV (cf. J curve in Fig. 4.14).

The detuning effects on the singlet and triplet states can be further illustrated by inspecting the electron density variations. In Fig. 4.13(a) we see that for coupled circular QDs ($r = 1$), with increasing ϵ , electrons gradually move into the lower (left) QD for both singlet and triplet states, albeit more quickly for the singlet state. When both electrons are in the left dot [Fig. 4.13(a), column (III)], the singlet density has a single maximum corresponding to the state with nearly zero angular momentum [65], while the triplet state exhibits two maxima along the QD coupling direction (x) as the constituent QDs are slightly more extended in the x -direction than in the y -direction. For $r = 3$, as ϵ increases, the singlet

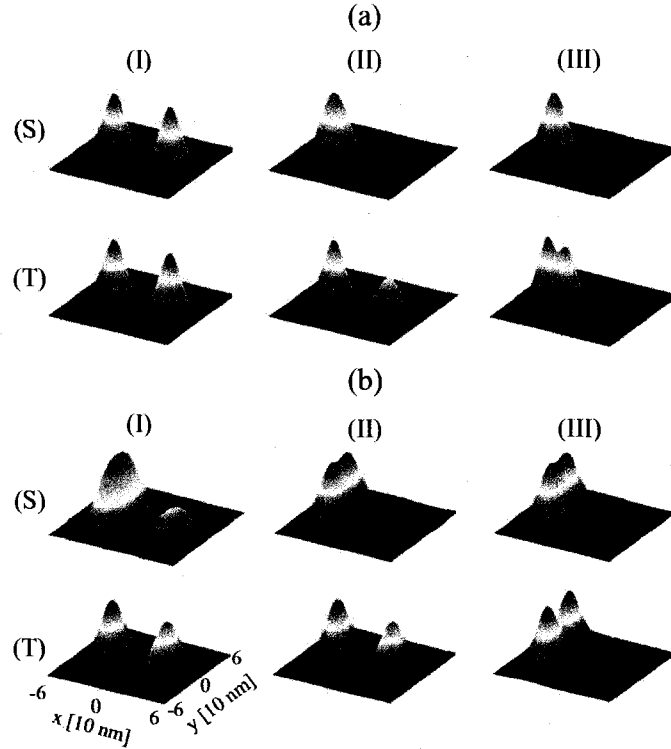


Figure 4.13 (a) Two-dimensional density plots for $r = 1$ at zero magnetic field. Columns (I), (II), and (III) correspond to $V_L = 21, 29$, and 42 meV, respectively. First (second) row, labeled S (T), is for the lowest singlet (triplet) state. (b) Same as (a) but for $r = 3$. Columns (I), (II), and (III) correspond to $V_L = 25, 25.45$, and 25.47 meV, respectively. Coordinates are shown in lower left panel and are the same for all panels. For $r = 3$, the peak separation along the x (y) direction in the density of the triplet state is ~ 60 (~ 40) nm for column (II) [(III)].

density gradually localizes into the left dot with the electron density showing two maxima in the y -direction once $V_L > 25$ meV because of the relaxed confinement in that direction [cf. Fig. 4.13(b) columns (I) and (II)]. For the triplet state, however, it is seen that the electron density abruptly changes from being spread over the two QDs with a higher peak in the left dot [$V_L = 25.45$ meV, column (II) in Fig. 4.13(b)] to occupying only the left dot with two peaks of equal height in the y -direction [$V_L = 25.47$ meV, column (III) in Fig. 4.13(b)]. This abrupt transition (or “rotation”) of the electron density occurs at $V_L = 25.46$ meV [point V' in Fig. 4.13(b)].

In order to understand the drastic difference in the dependences of the energy levels on ϵ between the QD configurations with $r = 1$ and $r = 3$, we compute the expectation values

of the parity operator $\langle \hat{P} \rangle = \langle \Psi(x_1, y_1, x_2, y_2) | \Psi(-x_1, -y_1, -x_2, -y_2) \rangle$, and of the parity operator with respect to the y -axis $\langle \hat{P}_y \rangle = \langle \Psi(x_1, y_1, x_2, y_2) | \Psi(x_1, -y_1, x_2, -y_2) \rangle$. Here, Ψ is the two-electron wavefunction, and (x_1, y_1) , (x_2, y_2) are the coordinates of the first and second electrons, respectively. In the investigated detuning range, we find that for the singlet state, $0 < P < 1$ and $P_y = 1$ for all r ; while for the triplet state at $r = 1$, $P < 0$ and $P_y = 1$, as expected from the symmetry of the Hamiltonian. However, in the triplet state for $r = 3$ at $V_L = 25.46$ meV, our calculation shows that the value of $\langle \hat{P} \rangle$ sharply increases from -0.98 to -0.02 , while $\langle \hat{P}_y \rangle$ changes sign from 1 to -1 . This indicates that the parity of the singlet state with respect to the y -axis remains even, while the triplet wavefunction parity changes from even to odd, thereby changing its symmetry along the y -direction. In fact, we find that as the interdot detuning is increased, the two lowest singlet states at any r have the same symmetry, and their energy levels anticross; the same is true for the two lowest triplet states at $r = 1$ (see Fig. 4.12), whereas the energy levels of the two lowest triplet states at $r > 1$ [Fig. 4.12(b)] cross due to their different symmetries in agreement with the von Neumann-Wigner theorem [58]. Near the crossing point of the two lowest triplet energy levels [point V' in Fig. 4.12(b)], the analysis of the spectral function [54] reveals that the first excited single-particle state localized in the left QD has the p_y -character [see schematic energy diagram in the upper inset of Fig. 4.12(b)]. Before the level crossing, this p_y -like orbital is unoccupied so that the electronic states form an sp_x -pair consisting of the s -like state mostly localized in the left QD, and the lowest antisymmetric p_x -like state spreading over both QDs. After the level crossing, it becomes energetically favorable for the triplet electrons to be in the same QD as an sp_y -pair, even though the expectation value of the coulomb interaction in the triplet state increases from 2.0 meV before the transition $sp_x \rightarrow sp_y$ to 2.9 meV afterwards.

Figure 4.14 displays the exchange coupling J as a function of V_L , or effectively as a function of $\epsilon = V_L - V_R$ (V_R is fixed at 21 meV). Each curve in Fig. 4.14 depicts the variation of J as the coupled QDs undergo the transition from the $(1, 1)$ to $(2, 0)$ charge

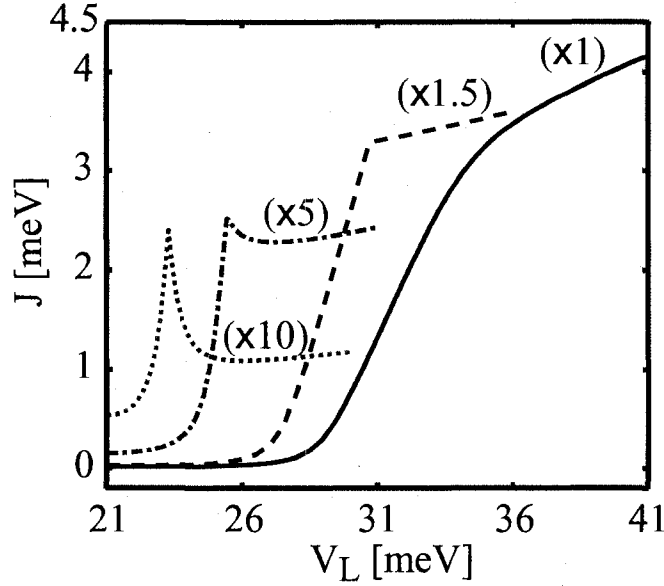


Figure 4.14 Exchange coupling J as a function of V_L (V_R fixed at 21 meV) for QD aspect ratios $r = 1$ (black, solid), $r = 1.5$ (blue, dashed), $r = 3$ (green, dashed-dotted), and $r = 5$ (red, dotted) at zero magnetic field. The scaling factor for each curve is shown in parenthesis.

states (the right end of each curve is chosen at a bias point where ϵ is large enough to localize both electrons into the left dot). For small departure from equal biases ($\epsilon \gtrless 0$), as V_L increases from 21 meV, J maintains a small and approximately constant value before it increases superlinearly, as was recently observed both experimentally [15] and reproduced theoretically [52]. For $r = 1$, J continues to increase monotonically with ϵ as the two electrons strongly localize in one QD. In this case, the localization of the first excited single-particle state that has p_x -character in the left dot occurs at larger detuning value than the ground state [points U and V in Fig. 4.12(a)], and J can only increase as the interlevel separation in the individual QD is larger than that in the coupled QD system. However, with increasing aspect ratios ($r \geq 1.5$), dramatic changes in the J behavior appear: a kink in J occurs at $V_L = 30.70$ meV with a sudden slope change for $r = 1.5$, while sharp maxima in J arise at 25.46 and 23.30 meV for $r = 3$ and $r = 5$, respectively. In the latter cases, there is also a local J minimum at $V_L = 27.20$ and 26.20 meV, respectively. For increasing r , electron localization in the left dot occurs at progressively smaller detuning

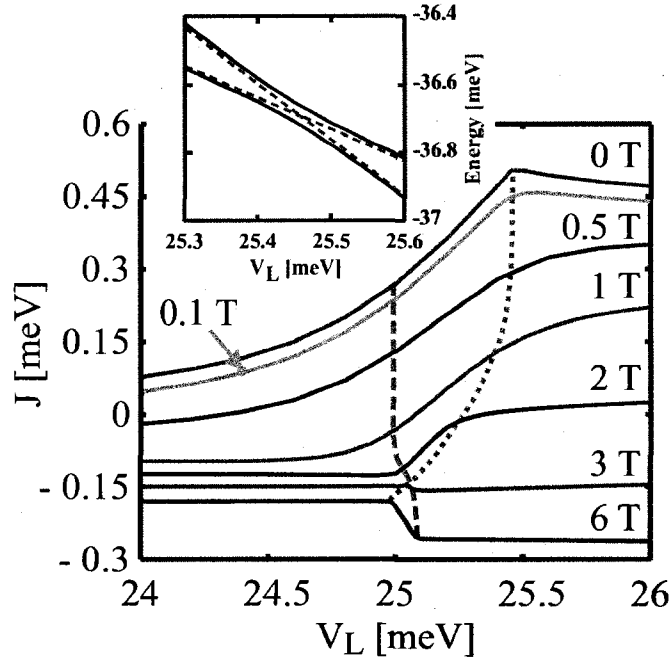


Figure 4.15 Main panel: J as a function of V_L for $r = 3$ at different magnetic fields. The magnetic field value is given on top of each curve. The curve for $B = 0.1$ T is indicated by an arrow. For clarity, curves at different B fields are shifted vertically in multiples of 0.03 meV. The dashed (dotted) gray line is a guide for the eyes tracing the localization point of the singlet (triplet) state at different magnetic fields. Inset: two lowest triplet energy levels at $B = 0$ T (red, dashed) and $B = 0.1$ T (blue, solid).

(Fig. 4.14), as it becomes easier for the system to lower its energy in a configuration where the two electrons are located at the opposite “ends” of the elliptical QD [Fig. 4.13(b)] to minimize their coulomb interaction. As a result, both singlet and triplet electrons move into the left dot at close V_L values [e.g., points U' and V' in Fig. 4.12(b) for $r = 3$]. Depending upon the difference between the biases required to localize singlet and triplet states into a single dot, the crossing between the two lowest triplet states associated with the electron density rotation is observed as a kink ($r \gtrsim 1$) or a sharp maximum ($r \gg 1$) in the exchange coupling at intermediate values of detuning.

Figure 4.15, main panel, shows the J -dependence on V_L for $r = 3$ in the detuning range corresponding to the $(1, 1) \Rightarrow (2, 0)$ transition ($24 \leq V_L \leq 26$ meV; $V_R = 21$ meV) for different magnetic fields normal to the xy -plane. We observe that the sharp discontinuities in dJ/dV_L due to abrupt electron density rotation with detuning disappear for $0 < B \leq 2$

T , and evolves into a smooth J -increase with V_L . By adding angular momentum to the electron motion, the magnetic field mixes the p_x and p_y state parities, breaking the Cartesian symmetry of the two-electron wavefunction, and quenching the abruptness of the density rotation. This symmetry breaking (from p_y -symmetry to p_x - p_y symmetry mixing) removes the crossing conditions between the two lowest triplet states to produce level anticrossing, in agreement with the von Neumann-Wigner theorem (Fig. 4.15 inset). Our analysis also indicates smooth variations of the electron density with detuning at small nonzero ($0 < B \leq 2$ T) magnetic fields: for small ϵ , the triplet electron density has a higher peak in the left dot than in the right dot, which, with increasing ϵ , evolves into two peaks along the y -direction, while the peak in the right dot gradually disappears. At higher magnetic fields ($B = 3$ and 6 T), the localization of both singlet and triplet states in the left dot occurs abruptly with increasing detuning because of the strong magnetic compression of the electron orbitals. We observe that for increasing magnetic fields the triplet state localization requires progressively smaller detuning (shown by the dotted line on Fig. 4.15, main panel), while the singlet state localization occurs at almost the same detuning (shown by the dashed line on Fig. 4.15, main panel) for all investigated magnetic fields (the localization of the singlet and triplet states is determined at the point where the two lowest two-particle energy levels cross or anticross as detuning increases.).

Experimentally, the predicted variations in the two-electron density and exchange coupling can be obtained from the conductance responses of quantum point contacts adjacent to the dots, which are sensitive enough to register very slight changes in the coulomb potential distributions in the coupled QD system [13, 15]. One can also detect the existence of the maximum in the exchange coupling from the coherent Rabi oscillations in the two-electron system by properly biasing the QD system [15]. Finally, electron imaging spectroscopy can be utilized to directly probe the electron density in QDs [67].

CHAPTER 5

COUPLED QUANTUM WIRE QUANTUM DOTS

In this chapter, we investigate coupled quantum dots formed in a single quantum wire. We use the variational Heitler-London method to compute the system energies. Our analysis aims not at quantitative exactness, but rather at showing the interesting behavior of the system energies induced by the size effects.

5.1 Three-Dimensional Confinement Potential

Figure 5.1(a) shows a schematic of coupled QDs $D1$ and $D2$ formed in a single quantum wire: gates $G1$ and $G5$ define the outer barriers of the QDs, $G3$ controls the interdot coupling, and $G2$ and $G4$ are used as plunger gates for fine tuning of the potential in each QD. The charging current flows from source to drain along the wire. The material under consideration is InAs, for which we use the electron effective mass $m = 0.023m_0$ ([68], in previous chapters we use m^* to denote electron effective mass) and dielectric constant $\epsilon = 14.6$. Hence, the effective Bohr radius $r_0 = \hbar^2\epsilon/me^2 = 33.6$ nm and effective Rydberg constant $Ry = me^4/2\epsilon^2\hbar^2 = 1.468$ meV. We assume a parabolic confinement potential in the xy -plane $V(\rho) = m\Omega_\rho^2\rho^2/2$, wherein we take $\Omega_\rho = \hbar/m(D/2)^2$, and D is the nominal value of the wire diameter. In the z -direction (along which the QDs are coupled), the

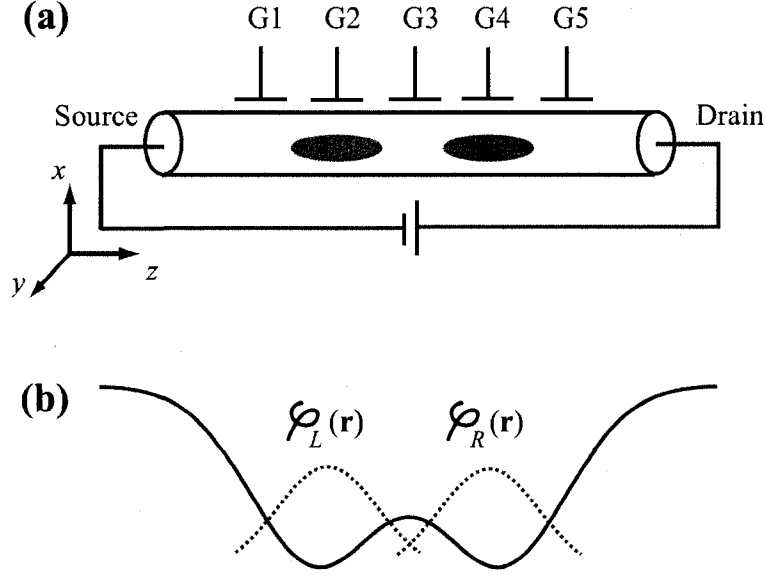


Figure 5.1 (a) Schematic of coupled QDs $D1$ and $D2$ formed in a quantum wire. Gates $G1$ and $G5$ define the outer barriers of the two QDs; $G3$ controls the interdot coupling; $G2$ and $G4$ are plungers tuning the confinement in each QD. Charging current flows along the wire from source to drain. (b) Schematic of the confinement potential of the coupled QDs along the z (wire axial) direction. $\varphi_L(r)$ and $\varphi_R(r)$ denote the localized s states in the left and right QDs, respectively.

confinement potential is modeled by a linear combinations of three Gaussians:

$$V(z) = -V_0 \left\{ \exp \left[-\frac{(z-d)^2}{l_z^2} \right] + \exp \left[-\frac{(z+d)^2}{l_z^2} \right] \right\} + V_b \exp \left(-\frac{z^2}{l_{bz}^2} \right), \quad (5.1)$$

where V_0 gives the depth of two Gaussian wells describing the confinement of the two individual QDs (we fix $V_0 = 20$ meV), V_b controls the barrier height between the two wells ($V_b = 0$ except otherwise specified), l_z is the radius of each QD, $2d$ is the nominal separation between the two QDs (in previous chapters, we used d to denote the interdot separation), and l_{bz} denotes the radius of the central barrier. A schematic of $V(z)$ is shown in Fig. 5.1(b) by the solid line.

5.2 The Variational Heitler-London Method

The two electrons in the coupled QDs are described by the following Hamiltonian:

$$\hat{H} = \hat{H}_{orb} + \hat{H}_Z, \quad (5.2)$$

$$\hat{H}_{orb} = \hat{h}_1 + \hat{h}_2 + \frac{e^2}{\epsilon |\mathbf{r}_1 - \mathbf{r}_2|}, \quad (5.3)$$

$$\hat{h}_i = \frac{1}{2m} \left(\mathbf{p}_{\rho_i} + \frac{e}{c} \mathbf{A}_i \right)^2 + V(\rho_i) + \frac{1}{2m} \mathbf{p}_{z_i}^2 + V(z_i), \quad (5.4)$$

$$\hat{H}_Z = g\mu_B \sum_i \mathbf{B} \cdot \mathbf{S}_i. \quad (5.5)$$

Note that we separate the motion of the electron in the xy -plane and in the z -direction in the single-particle Hamiltonian \hat{h}_i . In this work, we only consider magnetic fields applied in the z -direction for which $\mathbf{A} = (-yB\hat{x} + xB\hat{y})/2$. Such a magnetic field effectively enhances the confinement of the in-plane (xy -plane) ground state while preserving its cylindrical symmetry.

In order to obtain the system energies, we use the following trial wavefunctions:

$$\chi_{\pm}(\mathbf{r}) = \frac{\varphi_L(\mathbf{r}) \pm \varphi_R(\mathbf{r})}{\sqrt{2(1 \pm S)}}, \quad (5.6)$$

$$\Psi_{\pm}(\mathbf{r}_1, \mathbf{r}_2) = \frac{\varphi_L(\mathbf{r}_1)\varphi_R(\mathbf{r}_2) \pm \varphi_L(\mathbf{r}_2)\varphi_R(\mathbf{r}_1)}{\sqrt{2(1 \pm S^2)}}. \quad (5.7)$$

Here, χ_+ , χ_- , Ψ_+ , and Ψ_- denote the single-particle ground and first excited states, two-electron singlet and triplet states, respectively. $S = \langle \varphi_L | \varphi_R \rangle$ is the overlap between s orbitals $\varphi_L(\mathbf{r})$ and $\varphi_R(\mathbf{r})$ localized in the left and right QDs, respectively. Their specific expressions are

$$\varphi_{L/R}(\mathbf{r}) = \left(\frac{m\omega_{\rho}}{\pi\hbar} \right)^{\frac{1}{2}} \exp \left[-\frac{m\omega_{\rho}}{2\hbar} (x^2 + y^2) \right] \left(\frac{m\omega_z}{\pi\hbar} \right)^{\frac{1}{4}} \exp \left[-\frac{m\omega_z}{2\hbar} (z \pm a)^2 \right]. \quad (5.8)$$

Figure 5.1(b) shows the schematic of $\varphi_L(\mathbf{r})$ and $\varphi_R(\mathbf{r})$ in the z -direction by dashed lines on top of the potential. With the variational wavefunctions, we calculate the single-particle ground and first excited state energies $e^{0/1} = \langle \chi_{\pm} | \hat{h} | \chi_{\pm} \rangle$, two-electron singlet and triplet state energies $E^{S/T} = \langle \Psi_{\pm} | \hat{H}_{orb} | \Psi_{\pm} \rangle$. The detailed expressions of these matrix elements are given in the Appendix B.

In our VHL approach, we use the effective in-plane confinement strength ω_{ρ} , z -direction confinement strength ω_z , and effective half interdot separation a as variational parameters to minimize the system energies.¹ By fixing these variational parameters equal to their nominal values $\omega_{\rho} = \sqrt{\Omega_{\rho}^2 + \omega_c^2}$ with $\omega_c = eB/mc$, $\omega_z = \Omega_z = \sqrt{2V_0/ml_z^2}$, and $a = d$, we recover the results from the conventional HL method. We calculate the coulomb energies in the singlet and triplet states by

$$\begin{aligned} E_{Coul}^{S/T} &= \langle \Psi_{\pm} | C | \Psi_{\pm} \rangle \\ &= \frac{1}{1 \pm S^2} (\langle \varphi_L \varphi_R | C | \varphi_L \varphi_R \rangle \pm \langle \varphi_L \varphi_R | C | \varphi_R \varphi_L \rangle), \end{aligned} \quad (5.9)$$

where $C = e^2/\epsilon|\mathbf{r}_1 - \mathbf{r}_2|$, and we have used the notation

$$\langle \varphi_L \varphi_R | C | \varphi_L \varphi_R \rangle = \langle \varphi_L(\mathbf{r}_1) \varphi_R(\mathbf{r}_2) | C | \varphi_L(\mathbf{r}_1) \varphi_R(\mathbf{r}_2) \rangle, \quad (5.10)$$

$$\langle \varphi_L \varphi_R | C | \varphi_R \varphi_L \rangle = \langle \varphi_L(\mathbf{r}_1) \varphi_R(\mathbf{r}_2) | C | \varphi_R(\mathbf{r}_1) \varphi_L(\mathbf{r}_2) \rangle. \quad (5.11)$$

The same notation has been used in expressing the matrix elements in Appendix B. Using both HL and VHL methods, we calculate the tunnel coupling $2t = e_1 - e_0$ and the exchange coupling $J = E_0^T - E_0^S$. From the two electron wavefunctions, we compute the electron

¹An initial guess for the variational parameters is given near their nominal values, and then we use the `fminsearch` subroutine in MATLAB that employs the Nelder-Mead simplex method to search for the minima of the system energies with respect to these parameters. It turns out that unless the overlap between the localized s states is too large, the simplex method always finds a global minimum within the physically reasonable range of the variational parameters.

density as $[\varphi_{L/R}(\mathbf{r})$ are real]

$$\begin{aligned}\rho^{S/T}(\mathbf{r}_1) &= 2 \int |\Psi_{\pm}(\mathbf{r}_1, \mathbf{r}_2)|^2 d\mathbf{r}_2 \\ &= \frac{1}{1 \pm S^2} [\varphi_L^2(\mathbf{r}_1) + \varphi_R^2(\mathbf{r}_1) \pm 2S\varphi_L(\mathbf{r}_1)\varphi_R(\mathbf{r}_1)].\end{aligned}\quad (5.12)$$

5.3 Exchange Energy

In Fig. 5.2, we plot (a) the single-particle ground state energy e_0 , (b) single-particle first excited state energy e_1 , (c) two-electron singlet state energy E_0^S and (d) two-electron triplet state energy E_0^T as a function of the half interdot separation d for $l_z = 30$ nm and $D = 20$ nm. The solid and dashed lines show the results obtained from VHL and HL methods, respectively, from which we see that VHL method indeed gives lower system energies than the HL method. Here, we note that each energy is minimized with respect to a set of its own variational parameters. We also note that the single-particle energies are positive simply because of the large energy contribution from the in-plane confinement: for $D = 20$ nm, $\hbar\omega_p \approx 33$ meV and is changed by less than 1% by varying d .

For $l_z = 30$ nm and $d = 20$ nm, the two Gaussian wells in Eq. (5.1) are strongly coupled. As a result, the z -direction potential has a single minimum at $z = 0$, corresponding to a single QD. As d increases, a potential barrier between the QDs starts to emerge (for $d > 21.2$ nm). Meanwhile, the potential minimum is raised, and the z confinement in each individual QD becomes stronger. The behavior of the single-particle energies is a result of these combined effects. For example, as d increases from 20 to 38 nm, both e_0 and e_1 sharply increase due to the large increase of the potential minimum [Figs. 5.2(a) and (b)]. For $38 < d < 60$ nm, e_0 still slowly increases, while e_1 starts to decrease. Our analysis based on the variational parameters shows competing effects of the kinetic and potential energies in this region: for e_0 , the kinetic energy increase dominates a slight drop of the potential energy, whereas for e_1 , the potential energy increase is offset by the drop in the

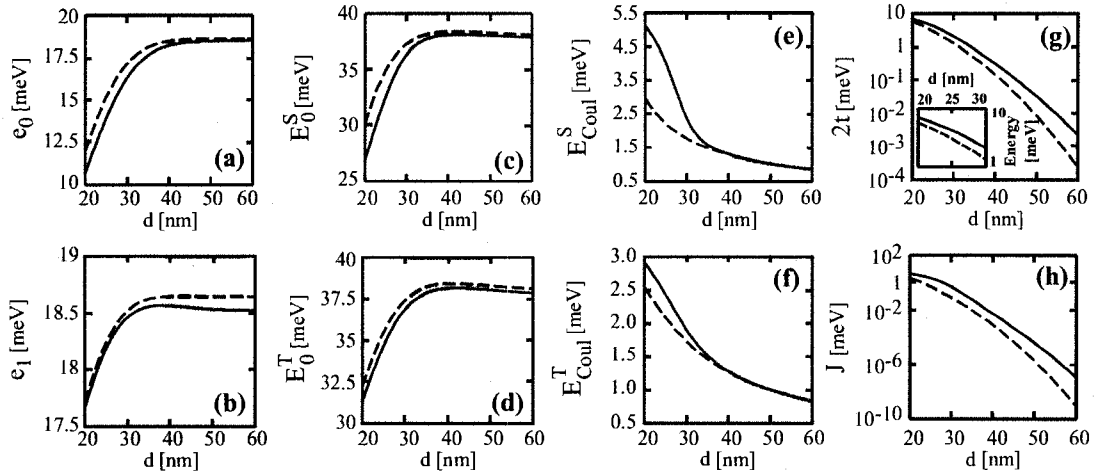


Figure 5.2 (a) Single-particle ground state energy, (b) single-particle first excited state energy, (c) two-electron singlet state energy, (d) two-electron triplet state energy, (e) coulomb energy in the singlet state, (f) coulomb energy in the triplet state, (g) tunneling coupling $2t$, and (h) exchange interaction as a function of the half interdot separation d for $l_z = 30$ nm and $D = 20$ nm. The inset in (g) shows $2t$ in the zoom-in region $20 < d < 30$ nm. On each panel, the solid (dashed) line shows the VHL (HL) result.

kinetic energy. For very large d , both e_0 and e_1 approach a constant value (18.53 meV), which corresponds to the limit of two decoupled quantum wells.

The behavior of E_0^S and E_0^T [Figs. 5.2(c) and (d)] resembles that of e_0 and e_1 , albeit a drop for $d > 41$ nm is observed for both quantities. The similarity implies that the single-particle energies are the dominant contributions to E_0^S and E_0^T , whereas the decrease of coulomb energy with increasing d [Figs. 5.2 (e) and (f)] has a minor influence. It is seen that at fixed d , the coulomb interaction is stronger in the singlet state, due to the larger overlap (S) in the two-electron wavefunction, which is a signature of the Pauli exclusion principle.

In Figs. 5.2 (g) and (h), we plot the tunnel coupling $2t$ and exchange coupling J as a function of d , respectively, both of which exhibit rapid decay with increasing d . In these figures, the solid (dashed) line corresponds to the VHL (HL) result. A much larger decrease of J ($\sim 10^{-8}$) than $2t$ ($\sim 10^{-4}$) as d increases from 20 to 60 nm agrees qualitatively with the Hubbard model $J \propto (2t)^2/U_H$, assuming that the intradot coulomb interaction U_H retains the same order of magnitude as d varies. Figures 5.2(g) and (h) show a large

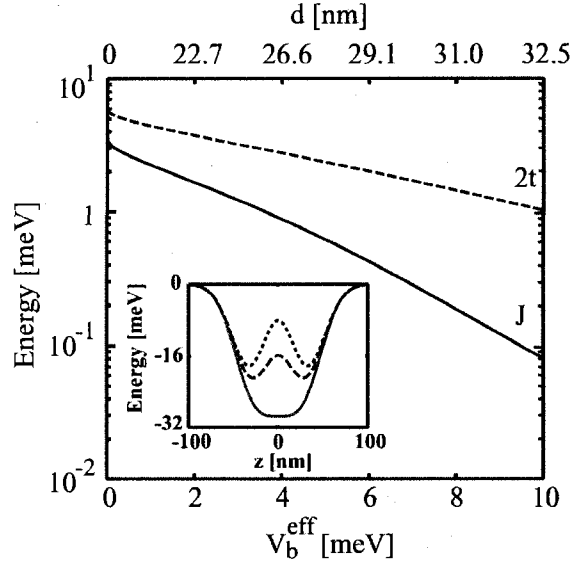


Figure 5.3 Main panel: Exchange coupling J (solid curve) and tunnel coupling $2t$ (dashed curve) as a function of the effective barrier height V_b^{eff} . Values of half interdot separation d corresponding to different V_b^{eff} values are shown on the upper horizontal scale. Inset: z -direction potential profile at V_b^{eff} values 0 meV (red, solid), 5 meV (green, dashed), and 10 meV (blue, dotted). Corresponding V_b values are -14.71 meV, -1.16 meV, and 6.65 meV, respectively. Values of other parameter are: $D = 20$ nm, $d = l_z = 30$ nm, and $l_b = 30$ nm.

difference between the tunnel and exchange couplings obtained by using the HL and VHL methods, from which we notice that the HL method substantially *underestimates* the coupling between the two electrons [36], especially for large interdot separations. For example, at $d = 60$ nm, the VHL result of $2t$ (J) is ~ 10 (~ 100) times of the HL result.

The inset in Fig. 5.3 indicates that both the effective barrier height V_b^{eff} (i.e., the energy difference between the minima of the potential and its value at $z = 0$) and the distance between the two QDs (i.e., the distance between the two minima of the potential) become larger as V_b is increased. Consequently, both $2t$ and J exhibit rapid decay with increasing V_b^{eff} as shown in the main panel of Fig. 5.3 [18, 69], similar to the rapid drop of these two quantities with increasing QD separation $2d$ [cf. Figs. 5.2(g) and (h)]. Again, we observe that J decays at a much faster rate than $2t$. In experimental QWQD devices, the effective barrier height between the two QDs can be tuned by varying the central gate bias [22, 23],

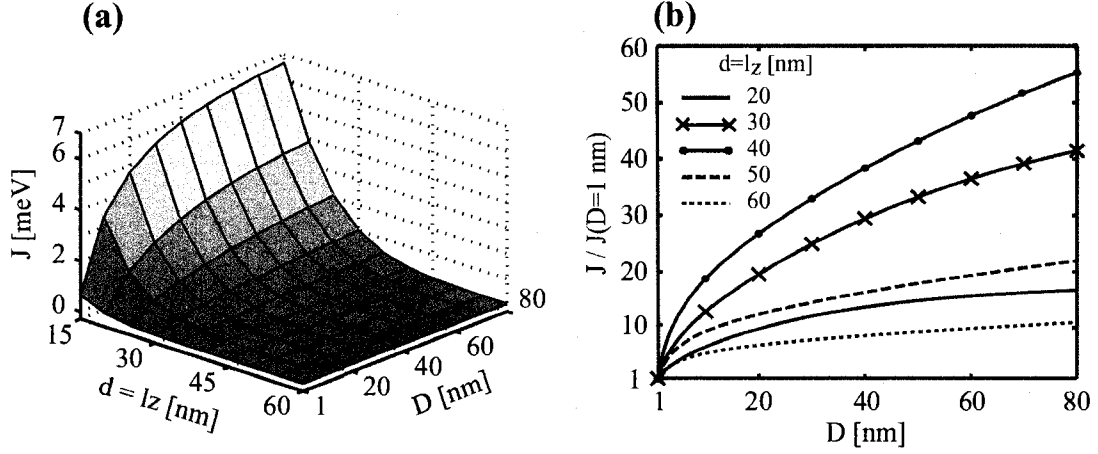


Figure 5.4 (a) Exchange coupling J as a function of wire diameter D and half separation between the QDs d , which is set equal to QD radius l_z ($d = l_z$). (b) J as a function of D for different $d = l_z$ values (shown in the figure). The J value on each curve is normalized to its value at $D = 1$ nm. For $(d = l_z) = 20, 30, 40, 50, 60$ nm, $J(D = 1 \text{ nm}) = 2.33 \times 10^{-1}, 2.47 \times 10^{-2}, 3.53 \times 10^{-3}, 1.37 \times 10^{-3}, 4.81 \times 10^{-4}$ meV, respectively.

and our analysis shows that the magnitude of the exchange coupling can be controlled by proper biasing of the central gate as in 2DEG-based coupled QDs [18].

5.4 Size Effects

Figure 5.4(a) displays the exchange coupling J as a function of both the wire diameter D and the half interdot separation d . Here, we set $d = l_z$ noting that in experiments coupled QWQDs are defined on top of a linear gate grid with a particular periodicity [22, 23], which indicates that the effective QD size and interdot separation are approximately the same. For the confinement potential given by Eq. (5.1), this configuration leads to a constant effective barrier height of 5.68 meV, independent of the value of $d = l_z$. The nominal confinement strength for a single Gaussian well ($V_0 = 20$ meV) with $l_z = 15$ nm ($0.45r_0$) and 60 nm ($1.78r_0$) is $\hbar\Omega_z = 24.27$ and 6.07 meV, respectively. For a wire diameter $D = 1$ nm, the nominal confinement is $\hbar\Omega_\rho = 1.33 \times 10^4$ meV, which physically corresponds to the *quasi-1D limit* of the systems with aspect ratio $(\lambda_\rho/\lambda_z = \sqrt{\Omega_z/\Omega_\rho}) < 0.05$ for the investigated range of $d = l_z$ from 15 to 60 nm. In the opposite limit, where $D = 80$ nm, $\hbar\Omega_\rho = 2.07$

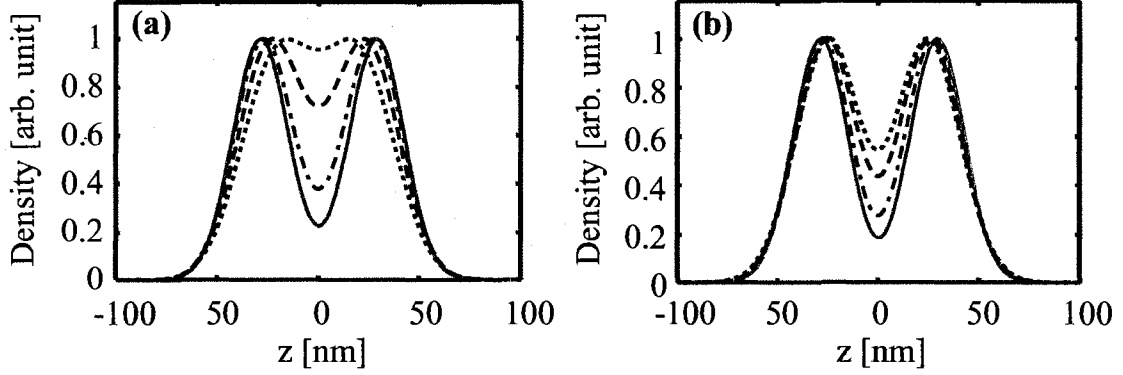


Figure 5.5 Electron density plot in the z -direction for (a) singlet and (b) triplet states at $d = l_z = 30$ nm. In each figure, the density is plotted at $D = 1$ nm (red, solid), $D = 10$ nm (green, dashed-dotted), $D = 40$ nm (blue, dashed), and $D = 80$ nm (black, dotted). For each D , the density is normalized to its peak value.

meV, the aspect ratio $\lambda_\rho/\lambda_z > 1.71$. At fixed D , J exhibits rapid decay with $d = l_z$ in Fig. 5.4(a), where it is also observed that J decreases with decreasing D at fixed $d = l_z$. This trend is shown explicitly in Fig. 5.4(b) for different $d = l_z$. For comparison, the data on each curve are normalized to the value of J at $D = 1$ nm. At fixed $d = l_z$, as D is decreased from 80 nm, J decreases, and the decreasing rate becomes larger as D approaches 1 nm, which is the *quasi* - 1D limit. The faster dropping rate of J near $D = 1$ nm is due to $\Omega_\rho \propto 1/D^2$, and the influence of the variation of Ω_ρ on J becomes stronger at smaller D (through the coulomb interaction). Here, we note that although the general trend of J is to decrease as D is made smaller, the decreasing rates are much larger for intermediate $d = l_z$ values than for small or large values.

These effects of the wire diameter variation on the exchange coupling are rather unexpected as they show that J depends on the wire confinement perpendicular to the coupling direction. In fact, we find that the D variation not only changes ω_ρ , but also induces significant changes in ω_z and a , which minimize the singlet and triplet state energies. One can directly visualize such changes by inspecting the electron density variation with respect to the wire diameter. In Fig. 5.5, we plot the electron density [Eq. (5.12)] for different D values ($d = l_z = 30$ nm) in the (a) singlet and (b) triplet states, respectively. For the singlet

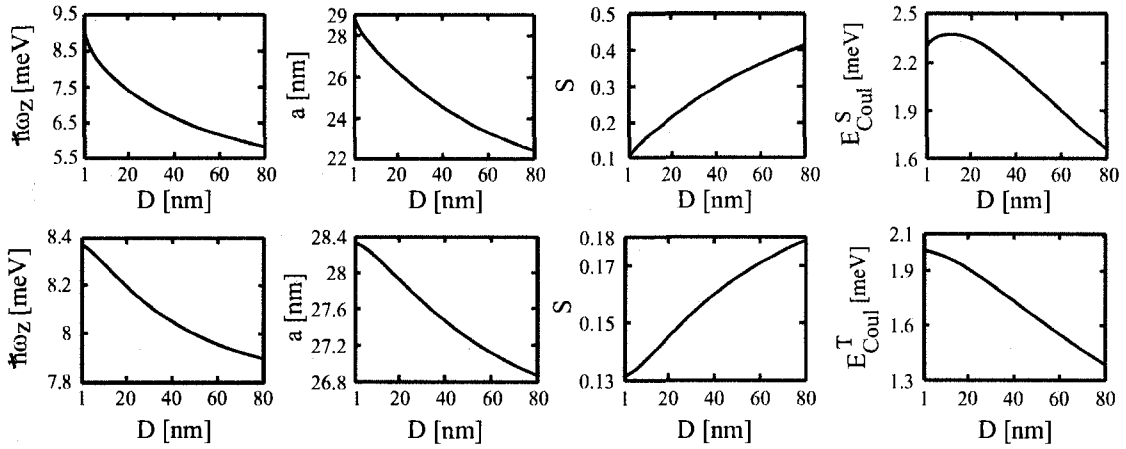


Figure 5.6 Variational parameters ω_z (shown as $\hbar\omega_z$), half separation a , the overlap S , and the coulomb energies as a function of D at $d = l_z = 30$ nm. Upper (lower) row is for the singlet (triplet) state.

state, as D decreases, the separation between the two density peaks becomes larger, and the width of each peak becomes smaller. Consequently, the overlap between the two electrons is reduced. Similar effects are observed in the density of the triplet state to a lesser extent.

We now provide a physical argument about the $3D$ dimensionality effect on the two-electron behavior. One can imagine the interaction between the two electrons in separate QDs as a summation of the interaction between parallel charged disks. As the wire diameter decreases, if the z profile of the density were unchanged, then two disks belonging to different dots would have a stronger coulomb interaction since greater portions on the two disks interact at an effectively shorter distance. This enhanced coulomb interaction will “push” the two electrons farther away in the coupling (z) direction. However, since the electrons are confined by the outer energy barriers, they can only become more localized in each dot with a larger separation.

The above argument is confirmed by the D dependence of ω_z and a on the top two rows in Fig. 5.6, where it is shown that both variational parameters increase as D is reduced, and the relative increase is more significant in the singlet than in the triplet state. As a consequence, the overlap $S = \langle \varphi_L | \varphi_R \rangle = \exp(-m\omega_z a^2 / \hbar)$ between the localized s states decreases with decreasing D in both states, and the relative decrease is larger in the

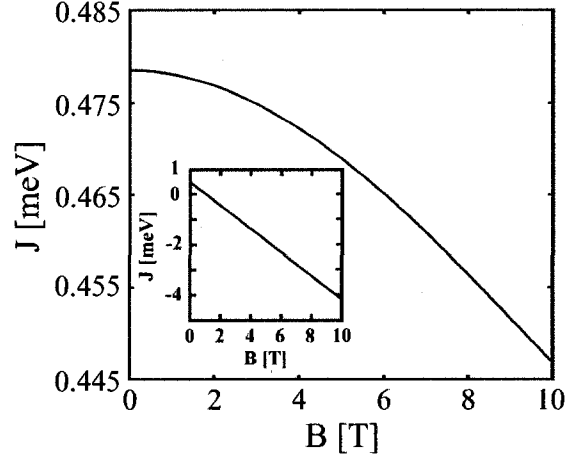


Figure 5.7 Main panel: Exchange coupling as a function of the magnetic field applied along the wire without the Zeeman effect for $D = 20$ nm, $d = l_z = 30$ nm. Inset: same as main panel but with Zeeman effect.

singlet state [Fig. 5.6, third row]. It is interesting to note that despite the reduced overlap, the coulomb interaction (E_{Coul}) still becomes stronger with decreasing D [Fig. 5.6, bottom row] for both states. We also performed analysis for different $d = l_z$ and observed similar behavior as shown in Figs. 5.5 and 5.6.

The in-plane electron confinement can also be enhanced by applying a magnetic field (B) along the wire without reducing the wire diameter. As with reducing D , J drops with increasing B as seen in Fig. 5.7, main panel. The drop is nearly linear at large B , which is smaller than the drop rate when D approaches 1 nm [cf. Fig. 5.4(b)]. This is because the in-plane effective (variational) confinement strength $\omega_p \approx \sqrt{\Omega_p^2 + \omega_c^2}$. Since $\omega_c \propto B$, $\omega_p \propto B$, while since $\Omega_p \propto 1/D^2$, $\omega_p \propto 1/D^2$. It should be pointed out that the relatively small J drop in Fig. 5.7 is obtained in the absence of the Zeeman effect, and it is well known that unlike the small g factor in GaAs ($g \approx -0.44$), InAs QWQD has a much larger g factor (2 to 15.5) [24], for which the Zeeman effect is dominant over the orbital effect in the J dependence on B . For example, the inset of Fig. 5.7 shows that for $g = 8$,² the

²Recently, the VHL method has been applied to calculate the two-electron energies in a single two-dimensional elliptical QD. By comparing the results to numerical exact diagonalization results, it is shown that the VHL method is successful in reproducing the magnetic field dependence of J .

Zeeman effect totally smears out the orbital effect illustrated in the main panel of Fig. 5.7, which leads to a negative J for $B > 1.1$ T.

Because we model the confinement in the xy -plane by a two-dimensional harmonic oscillator potential, the single-particle levels in that plane are given by the Fock-Darwin spectrum, whereby the energy separation between the ground and first excited states decreases as B increases (in contrast, this separation increases with decreasing D). In our calculations in Fig. 5.7, we take $D = 20$ nm and $d = l_z = 30$ nm. At $B = 10$ T, the separation is 16.44 meV, which is considerably larger than the sum of the single-particle energy separation in the z -direction (2.11 meV) and the coulomb energy in the triplet state (1.91 meV). This observation validates the assumptions of the HL method in which the wavefunctions are taken as linear combinations of localized Gaussians separated in the z -direction, and only the ground state in the xy -plane is taken into account.

Experimentally, the measurement of the addition energy is frequently performed to probe the energy levels of the QD [14, 25]. The addition energy of the N -th electron is defined as $E^a(N) = \mu(N) - \mu(N - 1)$, where $\mu(N)$ is the chemical potential of an N -electron QD. Within the VHL method, we are able to calculate the addition energy of the second electron as $E^a(2) = \mu(2) - \mu(1) = E_0^S - 2e_0$, where E_0^S and e_0 denote the singlet state energy and the single-particle ground state energy, respectively. We plot $E^a(2)$ as a function of the geometric parameters $d = l_z$ and D in Fig. 5.8. In general, as the QDs become larger (larger $d = l_z$ or D), the addition energy decreases, for both coulomb interaction and size quantization effects are reduced. We find (not shown) that at fixed $d = l_z$ and D , the coulomb energy between the two electrons is uniformly smaller than $E^a(2)$, which is due to the size quantization effects in the coupled QWQDs.

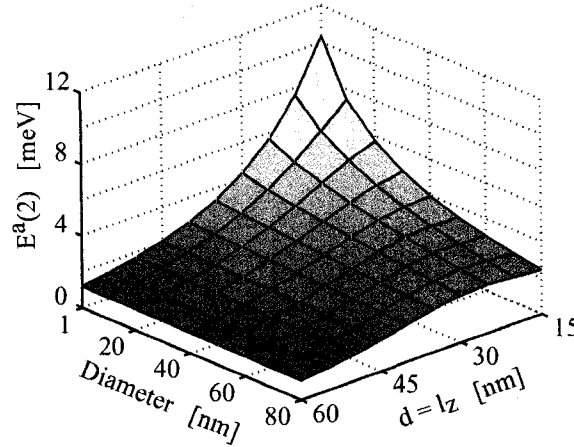


Figure 5.8 Addition energy of the second electron $E^a(2)$ as a function of wire diameter D and half interdot separation $d = l_z$.

5.5 Discussions

5.5.1 Limitation of the variational Heitler-London method

As an inherent drawback of the HL method, our variational scheme breaks down when the overlap between the localized s states is large, which occurs for small interdot separations. For example, in our calculations of the system energies, the VHL method fails for $(d = l_z) < 12$ nm ($0.57r_0$) independent of D . A signature of the VHL approach breakdown at small d is that the variational parameter a becomes zero in the minimization process. This numerical behavior stems from the fact that at small d a global minimum in the system energies does not exist for the physical range of a , given the expression of the variational wavefunction. We note that this shortcoming in the HL method is not apparent in the conventional HL approach. As long as $(d = l_z) > 0$, one can still use the HL method (without variation) to calculate the system energies even though the obtained result is likely to be nonphysical. We also find that the breakdown points depend upon the material parameters. For comparison, we list in Table 5.1 the breakdown points if the material parameters of GaAs ($m = 0.067m_0$, $\epsilon = 13.1$) were used. In Fig. 5.2, we fix $l_z = 30$ nm and vary the half separation d . In this scenario, the variational Heitler-London scheme breaks down

Table 5.1 Values of $d = l_z$ at which the variational Heitler-London calculation breaks down due to large overlap of the localized s states for energies of different states (shown on the leftmost column) at $D = 20$ nm. The second (third) column gives the values for InAs (GaAs). The unit of $d = l_z$ is effective Bohr radius r_0 . For InAs (GaAs), $r_0 = 33.59$ (10.35) nm.

Energy	$d = l_z$ for InAs	$d = l_z$ for GaAs
e_0	0.36	0.77
e_1	0.57	1.16
E_0^S	0.15	0.39
E_0^T	0.36	0.58

at d values similar to those listed in Table 5.1, whereas in this case the coupled Gaussian potential results in a single quantum well confinement with its minimum located at $z = 0$.

In [37, 69], it was pointed out that the HL method breaks down as the quantity $c = \sqrt{\pi/2}(e^2/\epsilon a_B)/\hbar\omega_0$ ($a_B = \sqrt{\hbar/m\omega_0}$) is larger than 1.95, 2.8, and 5.8 for coupled QDs with harmonic oscillator confinement $\hbar\omega_0$ in each direction for 1D, 2D, and 3D potential models, respectively (this is an extension of the result in [17]). We investigate l_z from 15 to 60 nm, which corresponds to c ranging from 0.44 to 0.87, and is uniformly smaller than the smallest breakdown value $c = 1.95$. However, as a check of this criterion, we extend our calculation to very large value of $d = l_z$ and find that for $D = 20$ nm, J becomes very noisy and oscillates randomly for $(d = l_z) > 206$ nm, for which the variational parameter $\hbar\omega_z$ is 1.553 meV, corresponding to $c = 1.723$, which is similar to the 1D limit claimed above. However, at this point, $J \sim 10^{-14}$ meV, which bears no practical interest.

5.5.2 Comparison with experiments

In recent experiments on InAs QWQDs, $J = 2.8$ to 3.2 meV was reported for a single QD formed in a wire with effective harmonic confinement strength $\hbar\Omega_z = 6.3$ meV (corresponding to confinement length $2\lambda_z = 2\sqrt{\hbar/m\Omega_z} = 46$ nm) and $\hbar\Omega_p = 40$ meV ($2\lambda_p = 2\sqrt{\hbar/m\Omega_p} = 18$ nm) [25]. By fitting these values in our model ($D = 18$ nm,

$V_0 = 41.6$ meV, $V_b = 0$ meV, $d = 0$ nm and $l_z = 117.9$ nm), we obtain $J = 3.51$ meV, which is comparable to the experimental result.

We note that $J \sim 3$ meV as obtained above is the result for a single QD with potential minimum at $z = 0$. For double QDs with $D = 20$ and $d = l_z = 30$ nm, we obtain $J \sim 0.5$ meV (Fig. 5.7), which corresponds to a time scale $(\tau_J = \hbar/J) \sim 1.1$ ps, on the same order as the reported spin decoherence time $T_2 = 0.5 - 1$ ps in InAs QWQDs [68] and much smaller than the reported spin dephasing time $T_2^* = 50 - 500$ ps in self-assembled InAs QDs [70, 71].

CHAPTER 6

CONCLUSIONS AND OUTLOOKS

While exploring the possibility of using spin states of electrons in coupled solid-state quantum dot systems remains a formidable task, the project has a profound impact on various fields of scientific research. Experimentally, it catalyzes the research of nanoscale device design, fabrication, and characterization, based on which many novel solid-state device concepts have been realized such as confinement of single conduction electrons, manipulation of many-particle spin states by externally applied electromagnetic fields, and spin-charge conversion based on coupled quantum dots or quantum point contacts. Theoretically, it provides fundamental insights into many-body interactions in nanoscale structures and enriches the application of several conventional methods such as density functional theory, configuration interaction, and quantum Monte Carlo methods.

The central concept of the solid-state spintronic quantum logic gate relies on the physical interaction between confined electrons in coupled quantum dots, which is the main focus of this dissertation. Instead of taking a pure theoretical viewpoint, the discussion in this dissertation finds strong relevance to experimental studies, especially on the relationship between exchange energy and stability diagram and geometric effects on the exchange energy. We have employed two major methods to study different quantum dot systems:

The first method is numerical exact diagonalization of the two-electron Hamiltonian, and it is applied to study two-dimensional coupled quantum dots. By comparing this method with other theoretical methods for quantum dot studies, we show that numerical

exact diagonalization provides the most accurate results for the energies and also allows us to study excited states as well as single-particle spectrum. With this method, we first show that the stability diagram in circular dots is in accordance with the general theorem on the effects of interdot coupling strength. We then study coupled elliptical dot systems, and find interesting effects of molecular state energy level crossing and anticrossing, which exemplify the general von Neumann-Wigner theorem. Another important finding is that, for coupled quantum dots with high aspect ratios, the stability region of one electron in each dot vanishes.

The second method is the variational Heitler-London method, which is applied to study coupled quantum dots formed in a single quantum wire. By comparing with the conventional Heitler-London method, we show that the variational approach in general yields better results of the system energies. The most important finding from this study is the quasi-one-dimensional effect of the exchange energy, which is significantly reduced with respect to the fully three-dimensional case due to the dimensionality effects on the Coulomb interaction between the two electrons. Moreover, the exchange energy we find in our calculation is in good agreement with available experimental data.

Looking into the future, there are still major technical challenges confronting the realization of a solid-state quantum computer such as precise control of the many-electron spin states as well as the scalability of the system, which in turn requires, from theoretical studies, accurate calculation of the many-electron interactions and better understanding of the physical implementation of quantum logics. Even beyond the context of quantum computing, with the downscaling trend for electronic devices similar challenges will soon emerge. It is critical to have strong interaction between theoretical and experimental studies in searching for new computation paradigms as this approach has met with great success in silicon technology.

APPENDIX A

MATHEMATICAL RESULTS FOR THE EXACT DIAGONALIZATION METHOD

In order to calculate the matrix element $\langle \chi_i(\mathbf{r}) | \hat{h} | \chi_j(\mathbf{r}) \rangle$, we rewrite the the single-particle Hamiltonian \hat{h} in Eq. (2.6) as

$$\hat{h} = \hat{h}_1 + \hat{h}_2 + \hat{h}_3 + \hat{h}_4, \quad (\text{A.1})$$

$$\begin{aligned} \hat{h}_1 = & -\frac{1}{2m^*} \frac{\partial^2}{\partial x^2} + \frac{1}{2} m^* \omega_{0x}^2 x^2 + \frac{1}{8m^*} \frac{e^2 B^2}{c^2} x^2 \\ & -\frac{1}{2m^*} \frac{\partial^2}{\partial y^2} + \frac{1}{2} m^* \omega_{0y}^2 y^2 + \frac{1}{8m^*} \frac{e^2 B^2}{c^2} y^2, \end{aligned} \quad (\text{A.2})$$

$$\hat{h}_2 = -\frac{1}{2} m^* \omega_{0x}^2 x^2 - \frac{1}{2} m^* \omega_{0y}^2 y^2, \quad (\text{A.3})$$

$$\hat{h}_3 = \frac{e\hbar B i}{2m^* c} \left(y \frac{\partial}{\partial x} - x \frac{\partial}{\partial y} \right), \quad (\text{A.4})$$

$$\hat{h}_4 = V(x, y). \quad (\text{A.5})$$

In general, $V(x, y)$ can assume any form. In our work, we have used the coupled Gaussian form in Eq. (2.1). We use for the single-particle basis states a product of the harmonic oscillator states, i.e., $\chi_i(\mathbf{r}) = \phi_m(x)\phi_n(y)$. Here, i is a composite index of m and n ; m and n denote the quantum numbers of the oscillators (for the analytic expression of $\phi_m(x)$, see, e.g., [59]) in the x and y directions. It is apparent that \hat{h}_1 is the Hamiltonian for a

two-dimensional harmonic oscillator with oscillator strength

$$\omega_{x/y} = \sqrt{\omega_{0x/y}^2 + (eB/2m^*c)^2}, \quad (\text{A.6})$$

therefore,

$$\langle \chi_i(\mathbf{r}) | \hat{h}_1 | \chi_j(\mathbf{r}) \rangle = [(m+1/2)\hbar\omega_x + (n+1/2)\hbar\omega_y] \delta_{m_1, m_2} \delta_{n_1, n_2}. \quad (\text{A.7})$$

Here and in the following (m_1, n_1) and (m_2, n_2) denote the composite indices for j and i .

Using lowering and raising operators, it is easy to show that

$$\begin{aligned} \langle \chi_i(\mathbf{r}) | \hat{h}_2 | \chi_j(\mathbf{r}) \rangle &= \frac{-\hbar\omega_{0x}^2}{4\omega_x} \left[(2n_1+1)\delta_{n_1, n_2} + \sqrt{(n_1+1)(n_1+2)}\delta_{n_1+2, n_2} \right. \\ &\quad \left. + \sqrt{n_1(n_1-1)}\delta_{n_1-2, n_2} \right] \delta_{m_1, m_2} \\ &\quad - \frac{\hbar\omega_{0y}^2}{4\omega_y} \left[(2m_1+1)\delta_{m_1, m_2} + \sqrt{(m_1+1)(m_1+2)}\delta_{m_1+2, m_2} \right. \\ &\quad \left. + \sqrt{m_1(m_1-1)}\delta_{m_1-2, m_2} \right] \delta_{n_1, n_2}. \end{aligned} \quad (\text{A.8})$$

Here, the terms $\sqrt{n_1(n_1-1)}\delta_{n_1-2, n_2}$ and $\sqrt{m_1(m_1-1)}\delta_{m_1-2, m_2}$ are present only when $n_1 > 2$ and $m_1 > 2$, respectively. The matrix element for \hat{h}_3 is evaluated also using raising and lowering operators, and the result is

$$\begin{aligned} &\langle \chi_i(\mathbf{r}) | \hat{h}_3 | \chi_j(\mathbf{r}) \rangle \\ &= \frac{e\hbar Bi}{4m^*c} \left[\sqrt{\frac{\omega_x}{\omega_y}} \left(\sqrt{m_1(n_1+1)}\delta_{m_1-1, m_2}\delta_{n_1+1, n_2} + \sqrt{m_1 n_1}\delta_{m_1-1, m_2}\delta_{n_1-1, n_2} \right. \right. \\ &\quad \left. \left. - \sqrt{(m_1+1)(n_1+1)}\delta_{m_1+1, m_2}\delta_{n_1+1, n_2} - \sqrt{(m_1+1)n_1}\delta_{m_1+1, m_2}\delta_{n_1-1, n_2} \right) \right. \\ &\quad \left. - \sqrt{\frac{\omega_y}{\omega_x}} \left(\sqrt{(m_1+1)n_1}\delta_{m_1+1, m_2}\delta_{n_1-1, n_2} + \sqrt{m_1 n_1}\delta_{m_1-1, m_2}\delta_{n_1-1, n_2} \right. \right. \\ &\quad \left. \left. - \sqrt{(m_1+1)(n_1+1)}\delta_{m_1+1, m_2}\delta_{n_1+1, n_2} \right. \right. \\ &\quad \left. \left. - \sqrt{m_1(n_1+1)}\delta_{m_1-1, m_2}\delta_{n_1+1, n_2} \right) \right]. \end{aligned} \quad (\text{A.9})$$

The potential term in the single-particle Hamiltonian can be written as

$$\begin{aligned}
V(x, y) &= V_x(x)V_y(y), \\
V_x(x) &= -V_L e^{-(x+d/2)^2/R_x^2} - V_R e^{-(x-d/2)^2/R_x^2}, \\
V_y(y) &= e^{-y^2/R_y^2}.
\end{aligned} \tag{A.10}$$

Then, $\langle \chi_i(\mathbf{r}) | V(x, y) | \chi_j(\mathbf{r}) \rangle = \langle \phi_{m_2}(x) | V_x(x) | \phi_{m_1}(x) \rangle \langle \phi_{n_2}(y) | V_y(y) | \phi_{n_1}(y) \rangle$. In principle, the integration in the x and y direction can be calculated analytically since for both of them, the integrand has the form of a product of a polynomial and Gaussian function. In practice, we evaluate them using `dqagie` in QUADPACK (<http://www.netlib.org/quadpack/dqagie.f>). We finally note that for a nonanalytical potential, the above formulation is still applicable by performing numerical integration of the potential (e.g., a potential defined on a mesh), which is an important step for the hybrid method [38, 50].

So far, we have computed the matrix element for the single-particle Hamiltonian, which is H_{pq} in Eq. (2.13). The overlap matrix element for the single-particle problem is

$$S_{pq} = \langle \chi_p(\mathbf{r}) | \chi_q(\mathbf{r}) \rangle = \delta_{p,q}. \tag{A.11}$$

The matrix element H_{pq} in the two-particle Hamiltonian in Eq. (2.13) can be expanded as a sum of single-particle matrix elements and coulomb terms:

$$\begin{aligned}
&\langle \Lambda_p^{S/T}(\mathbf{r}_1, \mathbf{r}_2) | \hat{H}_{orb} | \Lambda_q^{S/T}(\mathbf{r}_1, \mathbf{r}_2) \rangle \\
&= \langle \chi_i(\mathbf{r}_1) \chi_j(\mathbf{r}_2) \pm \chi_j(\mathbf{r}_1) \chi_i(\mathbf{r}_2) | \hat{h}_1 + \hat{h}_2 + C | \chi_k(\mathbf{r}_1) \chi_l(\mathbf{r}_2) \pm \chi_l(\mathbf{r}_1) \chi_k(\mathbf{r}_2) \rangle \\
&= 2 \left[\langle \chi_i(\mathbf{r}) | \hat{h} | \chi_k(\mathbf{r}) \rangle \delta_{j,l} \pm \langle \chi_j(\mathbf{r}) | \hat{h} | \chi_k(\mathbf{r}) \rangle \delta_{i,l} \right. \\
&\quad + \langle \chi_j(\mathbf{r}) | \hat{h} | \chi_l(\mathbf{r}) \rangle \delta_{i,k} \pm \langle \chi_i(\mathbf{r}) | \hat{h} | \chi_l(\mathbf{r}) \rangle \delta_{j,k} \\
&\quad \left. + \langle \chi_i(\mathbf{r}_1) \chi_j(\mathbf{r}_2) | C | \chi_k(\mathbf{r}_1) \chi_l(\mathbf{r}_2) \rangle \pm \langle \chi_i(\mathbf{r}_1) \chi_j(\mathbf{r}_2) | C | \chi_l(\mathbf{r}_1) \chi_k(\mathbf{r}_2) \rangle \right].
\end{aligned} \tag{A.12}$$

To evaluate the coulomb matrix element, we have used the formulation in [72], and the result is similar to that in [73]. The overlap matrix element S_{pq} in Eq. (2.13) is

$$\begin{aligned}
& \langle \Lambda_p^{S/T}(\mathbf{r}_1, \mathbf{r}_2) | \Lambda_q^{S/T}(\mathbf{r}_1, \mathbf{r}_2) \rangle \\
&= \langle \chi_i(\mathbf{r}_1) \chi_j(\mathbf{r}_2) \pm \chi_j(\mathbf{r}_1) \chi_i(\mathbf{r}_2) | \chi_k(\mathbf{r}_1) \chi_l(\mathbf{r}_2) \pm \chi_l(\mathbf{r}_1) \chi_k(\mathbf{r}_2) \rangle \\
&= 2 [\delta_{i,k} \delta_{j,l} \pm \delta_{i,l} \delta_{j,k}].
\end{aligned} \tag{A.13}$$

In Eqs. (A.12) and (A.13), p is a composite index for i and j , and q for k and l .

We solve the generalized eigenvalue problem for the single- and two-particle problem by utilizing the `zhegv`d in LAPACK (<http://www.netlib.org/lapack/complex16/zhegv.d.f>). Upon completion of the diagonalization procedure, we obtain for the single-particle problem the k -th eigenvalue e_k and eigenvector

$$\begin{aligned}
\psi_k(\mathbf{r}) &= \sum_{ki} a_{ki} \chi_{ki}(\mathbf{r}) \\
&= \sum_{kn, km} a_{kn, km} \phi_{kn}(x) \phi_{km}(y).
\end{aligned} \tag{A.14}$$

Here, ki is the composite index for in and im . For the two-particle problem $E_k^{S/T}$

$$\begin{aligned}
\Psi_k^{S/T}(\mathbf{r}_1, \mathbf{r}_2) &= \sum_{ks} b_{ks} \Lambda_{ks}^{S/T}(\mathbf{r}_1, \mathbf{r}_2) \\
&= \sum_{ki, kj} b_{ki, kj} [\chi_{ki}(\mathbf{r}_1) \chi_{kj}(\mathbf{r}_2) \pm \chi_{kj}(\mathbf{r}_1) \chi_{ki}(\mathbf{r}_2)] \\
&= \sum_{ki, kj} b_{ki, kj} [\phi_{kn}(x_1) \phi_{km}(y_1) \phi_{kq}(x_2) \phi_{kp}(y_2) \\
&\quad \pm \phi_{kq}(x_1) \phi_{kp}(y_1) \phi_{kn}(x_2) \phi_{km}(y_2)],
\end{aligned} \tag{A.15}$$

where ks is the composite index for ki and kj , ki for kn and km , kj for kq and kp . Note that in the last step we have used $\sum_{ki, kj} b_{ki, kj}$ instead of $\sum_{kn, km, kq, kp} b_{kn, km, kq, kp}$ for later convenience. In most of the cases, we only care about the singlet and triplet ground states,

for which we simplify the indexing as

$$\begin{aligned}
\Psi_0^{S/T}(\mathbf{r}_1, \mathbf{r}_2) &= \sum_{i,j} b_{i,j} [\chi_i(\mathbf{r}_1)\chi_j(\mathbf{r}_2) \pm \chi_j(\mathbf{r}_1)\chi_i(\mathbf{r}_2)] \\
&= \sum_{i,j} b_{i,j} [\phi_{in}(x_1)\phi_{im}(y_1)\phi_{jn}(x_2)\phi_{jm}(y_2) \\
&\quad \pm \phi_{jn}(x_1)\phi_{jm}(y_1)\phi_{in}(x_2)\phi_{im}(y_2)].
\end{aligned} \tag{A.16}$$

With the above expression, the electron density given in Eq. (2.16) is

$$\begin{aligned}
\rho^{S/T}(\mathbf{r}_1) &= \int |\Psi_0^{S/T}(\mathbf{r}_1, \mathbf{r}_2)|^2 d\mathbf{r}_2 \\
&= \sum_{i',j',i,j} b_{i',j'} b_{i,j} [\delta_{i',i}\chi_{j'}^*(\mathbf{r}_2)\chi_j(\mathbf{r}_2) + \delta_{j',j}\chi_{i'}^*(\mathbf{r}_2)\chi_i(\mathbf{r}_2) \\
&\quad \pm \delta_{i',j}\chi_{j'}^*(\mathbf{r}_2)\chi_i(\mathbf{r}_2) \pm \delta_{j',i}\chi_{i'}^*(\mathbf{r}_2)\chi_j(\mathbf{r}_2)].
\end{aligned} \tag{A.17}$$

The projection coefficient of two-particle states onto product of single-particle states (spectral function) is

$$\begin{aligned}
\alpha_{k,l}^{S/T} &= \langle \psi_k(\mathbf{r}_1)\psi_l(\mathbf{r}_2) | \Psi_0^{S/T}(\mathbf{r}_1, \mathbf{r}_2) \rangle \\
&= \left\langle \sum_{kn,km} a_{kn,km} \phi_{kn}(x_1)\phi_{km}(y_1) \sum_{ln,lm} a_{ln,lm} \phi_{ln}(x_2)\phi_{lm}(y_2) \right. \\
&\quad \left. | \sum_{i,j} b_{i,j} [\phi_{in}(x_1)\phi_{im}(y_1)\phi_{jn}(x_2)\phi_{jm}(y_2) \pm \phi_{jn}(x_1)\phi_{jm}(y_1)\phi_{in}(x_2)\phi_{im}(y_2)] \right\rangle \\
&= \sum_{kn,km} \sum_{ln,lm} \sum_{i,j} a_{kn,km}^* a_{ln,lm}^* b_{i,j} \\
&\quad [\delta_{kn,in}\delta_{km,im}\delta_{ln,jn}\delta_{lm,jm} \pm \delta_{kn,jn}\delta_{km,jm}\delta_{ln,in}\delta_{lm,im}].
\end{aligned} \tag{A.18}$$

We can also show that the parity operators are

$$\begin{aligned}
\langle \hat{P} \rangle &= \langle \Psi_0^{S/T}(x_1, y_1, x_2, y_2) | \Psi_0^{S/T}(-x_1, -y_1, -x_2, -y_2) \rangle \\
&= \sum_{i', j', i, j} b_{i', j'} b_{i, j} 2 [\delta_{i', i} \delta_{j', j} \pm \delta_{i, j'} \delta_{i', j}] (-1)^{in+im+jn+jm}, \\
\langle \hat{P}_y \rangle &= \langle \Psi_0^{S/T}(x_1, y_1, x_2, y_2) | \Psi_0^{S/T}(x_1, -y_1, x_2, -y_2) \rangle \\
&= \sum_{i', j', i, j} b_{i', j'} b_{i, j} 2 [\delta_{i', i} \delta_{j', j} \pm \delta_{i, j'} \delta_{i', j}] (-1)^{im+jm}. \tag{A.19}
\end{aligned}$$

Finally, the expectation value of the coulomb interaction in the singlet and triplet ground states is

$$\begin{aligned}
&\langle \Psi_0^{S/T}(\mathbf{r}_1, \mathbf{r}_2) | C | \Psi_0^{S/T}(\mathbf{r}_1, \mathbf{r}_2) \rangle \\
&= \sum_{i', j', i, j} b_{i', j'} b_{i, j} [\langle \chi_{i'}(\mathbf{r}_1) \chi_{j'}(\mathbf{r}_2) | C | \chi_i(\mathbf{r}_1) \chi_j(\mathbf{r}_2) \rangle \\
&\quad + \langle \chi_{j'}(\mathbf{r}_1) \chi_{i'}(\mathbf{r}_2) | C | \chi_j(\mathbf{r}_1) \chi_i(\mathbf{r}_2) \rangle \\
&\quad \pm \langle \chi_{j'}(\mathbf{r}_1) \chi_{i'}(\mathbf{r}_2) | C | \chi_i(\mathbf{r}_1) \chi_j(\mathbf{r}_2) \rangle \\
&\quad \pm \langle \chi_{i'}(\mathbf{r}_1) \chi_{j'}(\mathbf{r}_2) | C | \chi_j(\mathbf{r}_1) \chi_i(\mathbf{r}_2) \rangle]. \tag{A.20}
\end{aligned}$$

For the various coulomb matrix elements on the right-hand side, we have already tabulated them in previous calculations [Eq. (A.12)].

APPENDIX B

HEITLER-LONDON MATRIX ELEMENTS

In this appendix, we list the matrix elements used in the variational Heitler-London method we introduced in Chapter 5.

The single particle Hamiltonian \hat{h} can be rewritten as

$$\hat{h} = \hat{h}_{L/R}^0 + W_{L/R}, \quad (\text{B.1})$$

$$\begin{aligned} \hat{h}_{L/R}^0 = & \frac{1}{2m} \left(\mathbf{p}_\rho + \frac{e}{c} \mathbf{A} \right)^2 + \frac{1}{2} m \omega_{\rho 0}^2 \rho^2 \\ & + \frac{1}{2m} p_z^2 + \frac{1}{2} m \omega_z^2 (z \pm a)^2, \end{aligned} \quad (\text{B.2})$$

$$W_{L/R} = \frac{1}{2} m (\Omega_\rho^2 - \omega_{\rho 0}^2) \rho^2 + V(z) - \frac{1}{2} m \omega_z^2 (z \pm a)^2. \quad (\text{B.3})$$

Since $\hat{h}_{L/R}^0 \varphi_{L/R}(\mathbf{r}) = E_0 \varphi_{L/R}(\mathbf{r})$ and $E_0 = \hbar \omega_\rho + \hbar \omega_z/2$, we only need to calculate the matrix element of $W_{L/R}$. Thus, we have

$$\begin{aligned}
e^{0/1} &= \langle \chi_{\pm} | \hat{h} | \chi_{\pm} \rangle \\
&= \frac{1}{2} \hbar \omega_{\rho} + \frac{1}{4} \hbar \omega_z + \frac{\hbar}{2\omega_{\rho}} \left(\Omega_{\rho}^2 + \frac{\omega_c^2}{4} \right) \\
&\quad + \frac{1}{1 \pm S} \left\{ -V_0 \left(\frac{\hbar}{m\omega_z l_z^2} + 1 \right)^{-\frac{1}{2}} \exp \left[- \left(\frac{1}{l_z^2} + \frac{m\omega_z}{\hbar} \right)^{-1} \frac{m\omega_z}{\hbar l_z^2} (a+d)^2 \right] \right. \\
&\quad \left. - V_0 \left(\frac{\hbar}{m\omega_z l_z^2} + 1 \right)^{-\frac{1}{2}} \exp \left[- \left(\frac{1}{l_z^2} + \frac{m\omega_z}{\hbar} \right)^{-1} \frac{m\omega_z}{\hbar l_z^2} (a-d)^2 \right] \right. \\
&\quad \left. + V_b \left(\frac{\hbar}{m\omega_z l_{bz}^2} + 1 \right)^{-\frac{1}{2}} \exp \left[- \left(\frac{1}{l_{bz}^2} + \frac{m\omega_z}{\hbar} \right)^{-1} \frac{m\omega_z}{\hbar l_{bz}^2} a^2 \right] \right. \\
&\quad \left. \mp 2SV_0 \left(\frac{\hbar}{m\omega_z l_z^2} + 1 \right)^{-\frac{1}{2}} \exp \left[- \left(\frac{1}{l_z^2} + \frac{m\omega_z}{\hbar} \right)^{-1} \frac{m\omega_z}{\hbar l_z^2} d^2 \right] \right. \\
&\quad \left. \pm SV_b \left(\frac{\hbar}{m\omega_z l_{bz}^2} + 1 \right)^{-\frac{1}{2}} \mp \frac{S}{2} m\omega_z^2 a^2 \right\}. \tag{B.4}
\end{aligned}$$

Here, $S = \int d\mathbf{r} \varphi_L^*(\mathbf{r}) \varphi_R(\mathbf{r}) = \exp(-m\omega_z a^2/\hbar)$ is the overlap between the two localized s states.

The singlet and triplet energies are evaluated in a similar fashion and the results are

$$\begin{aligned}
E^{S/T} &= \langle \Psi_{\pm} | \hat{H}_{orb} | \Psi_{\pm} \rangle \\
&= 2E_0 + \frac{1}{1 \pm S^2} \\
&\quad \times [\langle \varphi_L \varphi_R | W_1 + W_2 + W_3 + C | \varphi_L \varphi_R \rangle \\
&\quad \pm Re \langle \varphi_L \varphi_R | W_1 + W_2 + W_3 + C | \varphi_R \varphi_L \rangle], \tag{B.5}
\end{aligned}$$

$$\begin{aligned}
\langle \varphi_L \varphi_R | W_1 | \varphi_L \varphi_R \rangle &= \langle \varphi_L \varphi_R | V(z_1) + V(z_2) | \varphi_L \varphi_R \rangle \\
&= -2V_0 \left(\frac{\hbar}{m\omega_z l_z^2} + 1 \right)^{-\frac{1}{2}} \\
&\quad \left\{ \exp \left[- \left(\frac{1}{l_z^2} + \frac{m\omega_z}{\hbar} \right)^{-1} \frac{m\omega_z}{\hbar l_z^2} (a+d)^2 \right] \right. \\
&\quad \left. + \exp \left[- \left(\frac{1}{l_z^2} + \frac{m\omega_z}{\hbar} \right)^{-1} \frac{m\omega_z}{\hbar l_z^2} (a-d)^2 \right] \right\} \\
&\quad + 2V_b \left(\frac{\hbar}{m\omega_z l_{bz}^2} + 1 \right)^{-\frac{1}{2}} \\
&\quad \exp \left[- \left(\frac{1}{l_{bz}^2} + \frac{m\omega_z}{\hbar} \right)^{-1} \frac{m\omega_z}{\hbar l_{bz}^2} a^2 \right], \tag{B.6}
\end{aligned}$$

$$\begin{aligned}
\langle \varphi_L \varphi_R | W_1 | \varphi_R \varphi_L \rangle &= \langle \varphi_L \varphi_R | V(z_1) + V(z_2) | \varphi_R \varphi_L \rangle \\
&= 2 \exp \left(-2 \frac{m\omega_z}{\hbar} a^2 \right) \left\{ -2V_0 \left(\frac{\hbar}{m\omega_z l_z^2} + 1 \right)^{-\frac{1}{2}} \right. \\
&\quad \exp \left[- \left(\frac{1}{l_z^2} + \frac{m\omega_z}{\hbar} \right)^{-1} \frac{m\omega_z}{\hbar l_z^2} a^2 \right] \\
&\quad \left. + V_b \left[\frac{\hbar}{m\omega_z l_{bz}^2} + 1 \right]^{-\frac{1}{2}} \right\}, \tag{B.7}
\end{aligned}$$

$$\begin{aligned}
\langle \varphi_L \varphi_R | W_2 | \varphi_L \varphi_R \rangle &= \left\langle \varphi_L \varphi_R \left| -\frac{1}{2} m \omega_z^2 (z_1 + a)^2 - \frac{1}{2} m \omega_z^2 (z_2 - a)^2 \right| \varphi_L \varphi_R \right\rangle \\
&= -\frac{1}{2} \hbar \omega_z, \tag{B.8}
\end{aligned}$$

$$\begin{aligned}
\langle \varphi_L \varphi_R | W_2 | \varphi_R \varphi_L \rangle &= \left\langle \varphi_L \varphi_R \left| -\frac{1}{2} m \omega_z^2 (z_1 + a)^2 - \frac{1}{2} m \omega_z^2 (z_2 - a)^2 \right| \varphi_R \varphi_L \right\rangle \\
&= -m \omega_z^2 \left(\frac{\hbar}{2m\omega_z} + a^2 \right) \exp \left(-2 \frac{m\omega_z}{\hbar} a^2 \right), \tag{B.9}
\end{aligned}$$

$$\begin{aligned}
\langle \varphi_L \varphi_R | W_3 | \varphi_L \varphi_R \rangle &= \left\langle \varphi_L \varphi_R \left| \frac{1}{2} m (\Omega_\rho^2 - \omega_{\rho 0}^2) (\rho_1^2 + \rho_2^2) \right| \varphi_L \varphi_R \right\rangle \\
&= \frac{\hbar}{\omega_\rho} \left(\Omega_\rho^2 + \frac{\omega_c^2}{4} - \omega_\rho^2 \right), \tag{B.10}
\end{aligned}$$

$$\begin{aligned}
\langle \varphi_L \varphi_R | W_3 | \varphi_R \varphi_L \rangle &= \left\langle \varphi_L \varphi_R \left| \frac{1}{2} m (\Omega_\rho^2 - \omega_{\rho 0}^2) (\rho_1^2 + \rho_2^2) \right| \varphi_R \varphi_L \right\rangle \\
&= \frac{\hbar}{\omega_\rho} \left(\Omega_\rho^2 + \frac{\omega_c^2}{4} - \omega_\rho^2 \right) \exp \left(-2 \frac{m\omega_z}{\hbar} a^2 \right). \tag{B.11}
\end{aligned}$$

The coulomb matrix elements in Eq. (5.9) are given by

$$\begin{aligned}\langle \varphi_L \varphi_R | C | \varphi_L \varphi_R \rangle &= \left\langle \varphi_L \varphi_R \left| \frac{e^2}{\epsilon |\mathbf{r}_1 - \mathbf{r}_2|} \right| \varphi_L \varphi_R \right\rangle \\ &= \frac{e^2}{\epsilon} \left(\frac{2m\omega_z}{\pi\hbar} \right)^{\frac{1}{2}} \int_0^1 \frac{1}{1 + \left(\frac{\omega_z}{\omega_\rho} - 1 \right) t^2} \exp \left(-2 \frac{m\omega_z}{\hbar} a^2 t^2 \right) dt, \quad (\text{B.12})\end{aligned}$$

$$\begin{aligned}\langle \varphi_L \varphi_R | C | \varphi_R \varphi_L \rangle &= \left\langle \varphi_L \varphi_R \left| \frac{e^2}{\epsilon |\mathbf{r}_1 - \mathbf{r}_2|} \right| \varphi_R \varphi_L \right\rangle \\ &= \frac{e^2}{\epsilon} \left(\frac{2m\omega_z}{\pi\hbar} \right)^{\frac{1}{2}} \exp \left(-2 \frac{m\omega_z}{\hbar} a^2 \right) \int_0^1 \frac{1}{1 + \left(\frac{\omega_z}{\omega_\rho} - 1 \right) t^2} dt \\ &= \frac{e^2}{\epsilon} \left(\frac{2m\omega_z}{\pi\hbar} \right)^{\frac{1}{2}} \exp \left(-2 \frac{m\omega_z}{\hbar} a^2 \right) \\ &\quad \times \begin{cases} \left(1 - \frac{\omega_z}{\omega_\rho} \right)^{-\frac{1}{2}} \operatorname{arctanh} \left[\left(1 - \frac{\omega_z}{\omega_\rho} \right)^{\frac{1}{2}} \right] & \text{for } \omega_z < \omega_\rho \\ \left(\frac{\omega_z}{\omega_\rho} - 1 \right)^{-\frac{1}{2}} \operatorname{arctan} \left[\left(\frac{\omega_z}{\omega_\rho} - 1 \right)^{\frac{1}{2}} \right] & \text{for } \omega_z > \omega_\rho \\ 1 & \text{for } \omega_z = \omega_\rho. \end{cases} \quad (\text{B.13})\end{aligned}$$

Here, we have used the transformation

$$\frac{e^2}{\epsilon |\mathbf{r}_1 - \mathbf{r}_2|} = \frac{e^2}{\epsilon \sqrt{\pi}} \int_0^\infty \frac{ds}{\sqrt{s}} \exp \{ -s[(x_1 - x_2)^2 + (y_1 - y_2)^2 + (z_1 - z_2)^2] \}. \quad (\text{B.14})$$

Practically, the one-dimensional integrals in Eqs. (B.12) and (B.13) are numerically evaluated using adaptive quadratures. We note that in the 1D limit ($\omega_\rho \rightarrow \infty$), the integrals have logarithmic divergence [37], while they both approach zero in the oppsite limit ($\omega_\rho \rightarrow 0$). For $\omega_\rho = \omega_z = \omega_0$, the integrals in Eqs. (B.12) and (B.13) simplify to $[e^2/(2a\epsilon)]\operatorname{Erf}(a\sqrt{2m\omega_0/\hbar})$ and $(e^2/\epsilon)\sqrt{2m\omega_0/(\pi\hbar)} \exp(-2m\omega_0 a^2/\hbar)$, respectively. These results are identical to the results in [37], where the coulomb matrix elements were calculated between coupled spherically symmetric Gaussian trial wavefunctions.

REFERENCES

- [1] R. C. Ashoori, H. L. Stormer, J. S. Weiner, L. N. Pfeiffer, S. J. Pearton, K. W. Baldwin, and K. W. West, "Single-electron capacitance spectroscopy of discrete quantum levels," *Physical Review Letters*, vol. 68, pp. 3088–3091, 1992.
- [2] M. A. Kastner, "The single-electron transistor," *Reviews of Modern Physics*, vol. 64, pp. 849–858, 1992.
- [3] D. Goldhaber-Gordon, H. Shtrikman, D. Mahalu, D. Abusch-Magder, U. Meirav, and M. A. Kastner, "Kondo effect in a single-electron transistor," *Nature*, vol. 391, pp. 156–159, 1998.
- [4] K. K. Likharev, "Single-electron devices and their applications," *Proceedings of IEEE*, vol. 87, pp. 606–632, 1999.
- [5] S. M. Reimann and M. Manninen, "Electronic structure of quantum dots," *Reviews of Modern Physics*, vol. 74, pp. 1283–1342, 2002.
- [6] L. Jacak, P. Hawrylak, and A. Wójs, *Quantum Dots*. Berlin: Springer, 1997.
- [7] L. P. Kouwenhoven, C. M. Marcus, P. L. McEuen, S. Tarucha, R. M. Westervelt, and N. S. Wingreen, *Mesoscopic Electron Transport, Proceedings of the Advanced Study Institute*, L. L. Sohn, L. P. Kouwenhoven, and G. Schön, Eds. Dordrecht, the Netherlands: Kluwer, 1997.
- [8] S. Tarucha, D. G. Austing, T. Honda, R. J. van der Hage, and L. P. Kouwenhoven, "Shell filling and spin effects in a few electron quantum dot," *Physical Review Letters*, vol. 77, pp. 3613–3616, 1996.
- [9] M. Ciorga, A. S. Sachrajda, P. Hawrylak, C. Gould, P. Zawadzki, S. Jullian, Y. Feng, and Z. Wasilewski, "Addition spectrum of a lateral dot from coulomb and spin-blockade spectroscopy," *Physical Review B*, vol. 61, p. R16315–R16318, 2000.
- [10] D. Loss and D. P. DiVincenzo, "Quantum computation with quantum dots," *Physical Review A*, vol. 57, pp. 120–126, 1998.
- [11] R. Hanson, L. P. Kouwenhoven, J. R. Petta, S. Tarucha, and L. M. K. Vandersypen, "Spins in few-electron quantum dots," *Reviews of Modern Physics*, vol. 79, pp. 1217–1265, 2007.

- [12] F. R. Waugh, M. J. Berry, D. J. Mar, R. M. Westervelt, K. L. Campman, and A. C. Gossard, "Single-electron charging in double and triple quantum dots with tunable coupling," *Physical Review Letters*, vol. 75, pp. 705–708, 1995.
- [13] J. M. Elzerman, R. Hanson, J. S. Geidanus, L. H. W. van Beveren, S. D. Franceschi, L. M. K. Vandersypen, S. Tarucha, and L. P. Kouwenhoven, "Few-electron quantum dot circuit with integrated charge read out," *Physical Review B*, vol. 67, p. 161308(R), 2003.
- [14] W. G. van der Wiel, S. D. Franceschi, J. M. Elzerman, T. Fujisawa, S. Tarucha, and L. P. Kouwenhoven, "Electron transport through double quantum dots," *Reviews of Modern Physics*, vol. 75, pp. 1–22, 2002.
- [15] J. R. Petta, A. Johnson, J. M. Taylor, E. A. Laird, A. Yacoby, M. D. Lukin, C. M. Marcus, M. P. Hanson, and A. C. Gossard, "Coherent manipulation of coupled electron spins in semiconductor quantum dot," *Science*, vol. 309, pp. 2180–2184, 2005.
- [16] T. Hatano, M. Stopa, and S. Tarucha, "Single-electron delocalization in hybrid vertical-lateral double quantum dots," *Science*, vol. 309, pp. 268–271, 2005.
- [17] G. Burkard, D. Loss, and D. P. DiVincenzo, "Coupled quantum dots as quantum gates," *Physical Review B*, vol. 59, pp. 2070–2078, 1999.
- [18] X. Hu and S. Das Sarma, "Hilbert-space structure of a solid-state quantum computer: Two-electron states of a double-quantum-dot artificial molecule," *Physical Review A*, vol. 61, p. 062301, 2000.
- [19] A. Harju, S. Siljamäki, and R. M. Nieminen, "Two-electron quantum dot molecule: Composite particles and the spin phase diagram," *Physical Review Letters*, vol. 88, p. 226804, 2002.
- [20] B. Szafran, F. M. Peeters, and S. Bednarek, "Exchange energy tuned by asymmetry in artificial molecules," *Physical Review B*, vol. 70, p. 205318, 2004.
- [21] W. Dybalski and P. Hawrylak, "Two electrons in a strongly coupled double quantum dot: From an artificial helium atom to a hydrogen molecule," *Physical Review B*, vol. 72, p. 205432, 2005.
- [22] C. Fasth, A. Fuher, M. T. Bjök, and L. Samuelson, "Tunable double quantum dots in InAs nanowires defined by local gate electrodes," *Nano Letters*, vol. 5, pp. 1487–1490, 2005.
- [23] A. Fuhrer, C. Fasth, and L. Samuelson, "Single electron pumping in InAs nanowire double quantum dots," *Applied Physics Letters*, vol. 91, p. 052109, 2007.
- [24] M. T. Björk, A. Fuhrer, A. E. Hansen, M. W. Larsson, L. E. Fröberg, and L. Samuelson, "Tunable effective g factor in InAs nanowire quantum dots," *Physical Review B*, vol. 72, p. 201307(R), 2005.

- [25] C. Fasth, A. Fuhrer, L. Samuelson, V. N. Golovach, and D. Loss, "Direct measurement of the spin-orbit interaction in a two-electron InAs nanowire quantum dot," *Physical Review Letters*, vol. 98, p. 266801, 2007.
- [26] L.-X. Zhang, D. V. Melnikov, and J.-P. Leburton, "Exchange interaction and stability diagram of coupled quantum dots in magnetic fields," *Physical Review B*, vol. 74, p. 205306, 2006.
- [27] S. Bednarek, B. Szafran, K. Lis, and J. Adamowski, "Modeling of electronic properties of electrostatic quantum dots," *Physical Review B*, vol. 68, p. 155333, 2003.
- [28] D. V. Melnikov, L.-X. Zhang, and J.-P. Leburton (unpublished), 2005.
- [29] E. A. Laird, J. R. Petta, A. C. Johnson, C. M. Marcus, A. Yacoby, M. P. Hanson, and A. C. Gossard, "Effect of exchange interaction on spin dephasing in a double quantum dot," *Physical Review Letters*, vol. 97, p. 056801, 2006.
- [30] J. Hubbard, "Electron correlations in narrow energy bands," *Proceedings of the Royal Society of London. Series A, Mathematical and Physical Sciences*, vol. 276, no. 1365, pp. 238–257, 1963.
- [31] J. Hubbard, "Electron correlations in narrow energy bands. II. The degenerate band case," *Proceedings of the Royal Society of London. Series A*, vol. 277, pp. 237–259, 1964.
- [32] J. Hubbard, "Electron correlations in narrow energy bands. III. An improved solution," *Proceedings of the Royal Society of London. Series A*, vol. 281, pp. 401–419, 1964.
- [33] J. Pedersen, C. Flindt, N. A. Mortensen, and A.-P. Jauho, "Failure of standard approximations of the exchange coupling in nanostructures," *Physical Review B*, vol. 76, p. 125323, 2007.
- [34] W. Heitler and F. London, "Wechselwirkung neutraler atome und homöopolare bindung nach der quantenmechanik," *Zeitschrift für Physik*, vol. 44, pp. 455–472, 1927.
- [35] C. Herring, "Critique of the Heitler-London method of calculating spin coupling at large distances," *Reviews of Modern Physics*, vol. 34, pp. 631–645, 1962.
- [36] R. de Sousa, X. Hu, and S. Das Sarma, "Effect of an inhomogeneous external magnetic field on a quantum-dot quantum computer," *Physical Review A*, vol. 64, p. 042307, 2001.
- [37] M. J. Calderon, B. Koiller, and S. Das Sarma, "Exchange coupling in semiconductor nanostructures: Validity and limitations of the Heitler-London approach," *Physical Review B*, vol. 74, p. 045310, 2006.

- [38] D. V. Melnikov and J.-P. Leburton, "Dimensionality effects in the two-electron system in circular and elliptic quantum dots," *Physical Review B*, vol. 73, p. 085320, 2006.
- [39] J. M. Thijssen, *Computational Physics*. Cambridge, UK: Cambridge University Press, 1999.
- [40] J. C. Slater, "The electronic structure of atoms—The Hartree-Fock method and correlation," *Reviews of Modern Physics*, vol. 35, pp. 484–487, 1963.
- [41] R. O. Jones and O. Gunnarsson, "The density functional formalism, its applications and prospects," *Reviews of Modern Physics*, vol. 61, pp. 689–746, 1989.
- [42] C. Yannouleas and U. Landman, "Spontaneous symmetry breaking in single and molecular quantum dots," *Physical Review Letters*, vol. 82, pp. 5325–5328, 1999.
- [43] S. Nagaraja, J.-P. Leburton, and R. M. Martin, "Electronic properties and spin polarization in coupled quantum dot," *Physical Review B*, vol. 60, pp. 8759–8766, 1999.
- [44] R. Ravishankar, P. Matagne, J.-P. Leburton, R. M. Martin, and S. Tarucha, "Three-dimensional self-consistent simulations of symmetric and asymmetric laterally coupled vertical quantum dots," *Physical Review B*, vol. 69, p. 035326, 2004.
- [45] L.-X. Zhang, P. Matagne, J.-P. Leburton, R. Hanson, and L. P. Kouwenhoven, "Single-electron charging and detection in a laterally coupled quantum-dot circuit in the few-electron regime," *Physical Review B*, vol. 69, p. 245301, 2004.
- [46] A. Wensauer, O. Steffens, M. Suhrke, and U. Rössler, "Laterally coupled few-electron quantum dots," *Physical Review B*, vol. 62, pp. 2605–2613, 2000.
- [47] F. Ancilotto, D. G. Austing, M. Barranco, R. Mayol, K. Muraki, M. Pi, S. Sasaki, and S. Tarucha, "Vertical diatomic artificial molecule in the intermediate-coupling regime in a parallel and perpendicular magnetic field," *Physical Review B*, vol. 67, p. 205311, 2003.
- [48] A. Harju, "Variational monte carlo for interacting electrons in quantum dots," *Journal of Low Temperature Physics*, vol. 140, pp. 181–210, 2005.
- [49] J. Kim, D. V. Melnikov, and J.-P. Leburton, "Coupled quantum dots as two-level systems: A variational monte carlo approach," vol. 1, pp. 1-6, 2008.
- [50] D. V. Melnikov, J.-P. Leburton, A. Taha, and N. Sobh, "Coulomb localization and exchange modulation in two-electron coupled quantum dots," *Physical Review B*, vol. 74, p. 041309, 2006.
- [51] P. Matagne and J.-P. Leburton, "Three-dimensional analysis of the electronic structure of cylindrical vertical quantum dots," *Physical Review B*, vol. 65, p. 235323, 2002.
- [52] M. Stopa and C. M. Marcus, "Magnetic field control of exchange and noise immunity in double quantum dots," *Nano Letters*, vol. 8, pp. 1778–1782, 2008.

- [53] D. Bellucci, M. Rontani, F. Troiani, G. Goldoni, and E. Molinari, "Competing mechanisms for singlet-triplet transition in artificial molecule," *Physical Review B*, vol. 69, p. 201308(R), 2004.
- [54] D. V. Melnikov and J.-P. Leburton, "Single-particle state mixing in two-electron double quantum dots," *Physical Review B*, vol. 73, p. 155301, 2006.
- [55] G. W. Bryant, "Electronic structure of ultrasmall quantum well boxes," *Physical Review Letters*, vol. 59, pp. 1140–1143, 1987.
- [56] C. E. Creffield, J. H. Jefferson, S. Sarkar, and D. L. J. Tipton, "Magnetic field dependence of the low-energy spectrum of a two-electron quantum dots," *Physical Review B*, vol. 62, pp. 7249–7256, 2000.
- [57] E. Räsänen, H. Saarikoski, M. J. Puska, and R. M. Nieminen, "Wigner-molecules in polygonal quantum dots: A density functional study," *Physical Review B*, vol. 67, p. 035326, 2003.
- [58] von J. v. Neumann and E. Wigner, "Über merkwürdige diskrete eigenwerte," *Physikalische Zeitschrift*, vol. 30, pp. 465–470, 1929.
- [59] L. D. Landau and E. Lifshitz, *Quantum Mechanics: Non-Relativistic Theory*. Oxford, UK: Pergamon Press, 1977.
- [60] W. Bron and M. Wagner, "Vibrational coupling of nearly degenerate electronic states," *Physical Review*, vol. 145, pp. 689–698, 1966.
- [61] W. Litchen, "Quantum mechanics of a double perturbation: Application to the Zeeman effect of metastable hydrogen molecules," *Physical Review A*, vol. 3, pp. 594–603, 1971.
- [62] Š. Pick and H. Dreysse, "Magnetic anisotropy of transition-metal thin films," *Physical Review B*, vol. 48, pp. 13 588–13 595, 1993.
- [63] N. W. Ashcroft and N. D. Mermin, *Solid State Physics*. New York, NY: Holt, Rinehart and Winston, 1976.
- [64] M. Helle, A. Harju, and R. M. Nieminen, "Two-electron lateral quantum dot molecules in a magnetic field," *Physical Review B*, vol. 72, p. 205329, 2005.
- [65] M. Wagner, U. Merkt, and A. V. Chaplik, "Spin-singlet-spin-triplet oscillations in quantum dots," *Physical Review B*, vol. 45, p. 1951, 1991.
- [66] A. C. Johnson, J. R. Petta, C. M. Marcus, M. P. Hanson, and A. C. Gossard, "Singlet-triplet spin blockade and charge sensing in a few-electron double quantum dot," *Physical Review B*, vol. 72, p. 165308, 2005.
- [67] P. Fallahi, A. C. Bleszynski, R. M. Westervelt, J. Huang, J. D. Walls, E. J. Heller, M. Hanson, and A. C. Gossard, "Imaging a single-electron quantum dot," *Nano Letters*, vol. 5, pp. 223–226, 2005.

- [68] A. E. Hansen, M. T. Björk, C. Fasth, C. Thelander, and L. Samuelson, “Spin relaxation in InAs nanowires studied by tunable weak antilocalization,” *Physical Review B*, vol. 71, p. 205328, 2005.
- [69] A. L. Saraiva, M. J. Calderon, and B. Koiller, “Reliability of the Heitler-London approach for the exchange coupling between electrons in semiconductor nanostructures,” *Physical Review B*, vol. 76, p. 233302, 2007.
- [70] I. A. Merkulov, A. L. Efros, and M. Rosen, “Electron spin relaxation by nuclei in semiconductor quantum dots,” *Physical Review B*, vol. 65, p. 205309, 2002.
- [71] P.-F. Braun, X. Marie, L. Lombez, B. Urbaszek, T. Amand, P. Renucci, V. K. Kalevich, K. V. Kavokin, O. Krebs, P. Voisin, and Y. Masumoto, “Direct observation of the electron spin relaxation induced by nuclei in quantum dots,” *Physical Review Letters*, vol. 94, p. 116601, 2005.
- [72] P. S. Drouvelis, P. Schmelcher, and F. K. Diakonov, “Global view on the electronic properties of two-electron anisotropic quantum dots,” *Physical Review B*, vol. 69, p. 035333, 2004.
- [73] J. Kyriakidis and S. J. Penney, “Coherent rotations of a single spin-based qubit in a single quantum dot at fixed Zeeman energy,” *Physical Review B*, vol. 71, p. 125332, 2005.

AUTHOR'S BIOGRAPHY

Lingxiao Zhang was born in Xi'an, China, on December 28, 1979. He received his B.S. degree in microelectronics from Peking University, China, in July 2001 and M.S. degree from the University of Illinois at Urbana-Champaign (UIUC) in December 2003. His research interests include theory of semiconductor devices, numerical simulation of nanoelectronic devices, semiconductor spintronics, and theory and simulation of bipolar transistor lasers. He has published eight journal papers and six conference papers. He has also been a teaching assistant for four undergraduate and graduate courses at UIUC. He is a recipient of the Gregory Stillman Semiconductor Research Award, M. E. Van Valkenburg Graduate Research Award, Mavis Fellowship Award, and Ross J. Martin Award, all from UIUC.